

Tropospheric Ozone Precursors: Global and Regional Distributions, Trends, and Variability

Yasin Elshorbany^{1*}, Jerald R. Ziemke², Sarah Strode^{2,3}, Hervé Petetin⁴, Kazuyuki Miyazaki⁵, Isabelle De Smedt⁶, Kenneth Pickering⁷, Rodrigo J. Seguel⁸, Helen Worden⁹, Tamara Emmerichs¹⁰, Domenico Taraborrelli¹⁰, Maria Cazorla¹¹, Suvarna Fadnavis¹², Rebecca R. Buchholz⁹, Benjamin Gaubert⁹, Néstor Y. Rojas¹³, Thiago Nogueira¹⁴, Thérèse Salameh¹⁵, Min Huang¹⁶

*Correspondence to: elshorbany@usf.edu

¹ School of Geosciences, College of Arts and Sciences, University of South Florida, St. Petersburg, FL, USA

² NASA Goddard Space Flight Center, Greenbelt, Maryland, USA

³ Goddard Earth Sciences Technology and Research (GESTAR II), Maryland, USA

⁴ Earth Sciences Department, Barcelona Supercomputing Center, Barcelona, Spain

⁵ Jet Propulsion Laboratory, California Institute of Technology, Pasadena CA

⁶ BIRA-IASB, Ringlaan 3 Av. Circulaire, 1180 Brussels, Belgium

⁷ Dept. of Atmospheric and Oceanic Science, University of Maryland, College Park, MD USA

⁸ Center for Climate and Resilience Research, Department of Geophysics, Faculty of Physical and Mathematical Sciences University of Chile, Chile.

⁹ Atmospheric Chemistry Observations & Modeling Laboratory (ACOM), NSF National Center for Atmospheric Research (NSF NCAR), Boulder CO, USA.

¹⁰ Institute of Climate and Energy Systems, ICE-3: Troposphere, Forschungszentrum Jülich GmbH, Jülich, Germany

¹¹ Universidad San Francisco de Quito USFQ, Instituto de Investigaciones Atmosféricas, Diego de Robles y Av Interoceánica, Quito, Ecuador.

¹² Center for Climate Change Research, Indian Institute of Tropical Meteorology, MoES, Pune, India.

¹³ Department of Chemical and Environmental Engineering, Universidad Nacional de Colombia, Bogota, Colombia.

¹⁴ University of São Paulo, São Paulo, Brazil.

¹⁵ IMT Nord Europe, Institut Mines-Télécom, Univ. Lille, Centre for Energy and Environment, 59000, Lille, France.

¹⁶ Earth System Science Interdisciplinary Center, University of Maryland, College Park, MD, USA.

36 **Abstract**

37 Tropospheric ozone results from in-situ chemical formation and stratosphere-troposphere
38 exchange (STE), with the latter being more important in the middle and upper troposphere than in
39 the lower troposphere. Ozone photochemical formation is nonlinear, and results from the oxidation
40 of methane and non-methane hydrocarbons (NMHCs) in the presence of nitrogen oxide
41 ($\text{NO}_x = \text{NO} + \text{NO}_2$). Previous studies showed that O_3 short- and long-term trends are nonlinearly
42 controlled by near-surface anthropogenic emissions of carbon monoxide (CO), volatile organic
43 compounds (VOCs), and nitrogen oxides, which maybe also impacted by the long-range transport
44 (LRT) of O_3 and its precursors. In addition, several studies have demonstrated the important role
45 of STE in enhancing ozone levels, especially in the midlatitudes. In this article, we investigate
46 tropospheric ozone spatial variability and trends from 2005 to 2019 and relate those to ozone
47 precursors on global and regional scales. We also investigate the spatiotemporal characteristics of
48 the ozone formation regime in relation to ozone chemical sources and sinks. Our analysis is based
49 on remote sensing products of the Tropospheric Column of Ozone (TrC- O_3) and its precursors,
50 nitrogen dioxide (TrC- NO_2), formaldehyde (TrC-HCHO), and total column of CO (TC-CO) as
51 well as ozonesonde data and model simulations. Our results indicate a complex relationship
52 between tropospheric ozone column levels, surface ozone levels, and ozone precursors. While the
53 increasing trends of near-surface ozone concentrations can largely be explained by variations in
54 VOC and NO_x concentration under different regimes, TrC- O_3 may also be affected by other
55 variables such as tropopause height and STE as well as LRT. Decreasing or increasing trends in
56 TrC- NO_2 have varying effects on the TrC- O_3 , which is related to the different local chemistry in
57 each region. We also shed light on the contribution of NO_x lightning and soil NO and nitrous acid
58 (HONO) emissions to trends of tropospheric ozone on regional and global scales.

59

60 1. Introduction

61 Tropospheric ozone (O₃) is an important air pollutant due to its diverse effects on air quality,
62 ecosystem (Mills et al., 2018), health (Lefohn et al., 2018; Fleming et al., 2018), and climate
63 (Boucher et al., 2013; Myhre et al., 2013; Zanis et al., 2022). O₃ is a photochemical product
64 that results from the oxidation of methane (CH₄) and non-methane hydrocarbons (NMHCs) in
65 the presence of nitrogen oxides (NO_x). Tropospheric ozone burdens can also be affected by
66 stratosphere-troposphere exchange (STE) (Stohl et al., 2003; Zeng et al., 2010; Trickl et al.,
67 2011; Li et al., 2024) and long-range transport (LRT) of ozone (e.g., Hov et al., 1978; Ravetta
68 et al., 2007; Itahashi et al., 2020). O₃ is considered a short-lived climate forcer (SLCF) and is
69 the third-most important greenhouse gas with an effective radiative forcing of (0.47^{+0.23}_{-0.23}) W
70 m⁻²; Forster et al., 2021). Since the mid-1990s, free tropospheric ozone trends based on in situ
71 measurement and satellite retrievals have increased with high confidence (HC) by 1-4 nmol
72 mol⁻¹ decade⁻¹ across the northern mid-latitudes and 1-5 nmol mol⁻¹ decade⁻¹ within the tropics
73 (Gulev et al., 2021). In the Southern Hemisphere, with more limited observation coverage
74 compared with the Northern Hemisphere, the tropospheric column ozone shows an increase
75 since the mid-1990s by less than 1 nmol mol⁻¹ decade⁻¹ with medium confidence at southern
76 mid-latitudes (Gulev et al., 2021, Cooper et al., 2020). Tropospheric O₃ short- and long-term
77 trends are nonlinearly controlled by anthropogenic emissions of carbon monoxide (CO),
78 volatile organic compounds (VOCs), and nitrogen oxides (NO_x=NO+NO₂) as well as STE,
79 especially in the midlatitudes (Li et al., 2024). Meteorological parameters such as wind speed
80 and wind direction may also enhance the LRT of O₃, affecting regional ozone burdens,
81 especially in the free troposphere (e.g., Glotfelty et al., 2014; Itahashi et al., 2020). Methane,
82 with an assessed total atmospheric lifetime of 9.1 ± 0.9 years (Szopa et al., 2021), is also a
83 crucial driver of tropospheric ozone (Fiore et al., 2002; Isaksen et al., 2014). Its accelerated
84 growth rate of 7.6 ± 2.7 nmol mol⁻¹ yr⁻¹ between 2010 and 2019 (Canadell et al., 2021) is
85 largely driven by anthropogenic activities (Szopa et al., 2021). NOAA GML observations of
86 methane (NOAA, 2024) show that methane concentrations in the atmosphere have increased
87 sharply since 2005 (an 8% increase from 2005 to 2023). Future scenarios show that emission
88 control measures can influence future changes to air pollutants. Although the global increases
89 in CH₄ abundance may offset benefits to surface O₃ from local emission reductions (Fiore et
90 al., 2002; Shindell et al., 2012; Wild et al., 2012; Szopa et al., 2021), recent reports (e.g.,
91 Itahashi et al., 2020; Zanis et al., 2022), showed the dominant role of precursor emission
92 changes in projecting surface ozone concentrations under future climate change scenarios. In
93 this study, we investigate the relation between ozone trends and the trends of its precursors,
94 with a focus on NO₂, CO, and HCHO.

95 Coupled Model Intercomparison Project Phase 6 (CMIP6) overestimates observed surface
96 O₃ concentrations in most regions, with larger variability over Northern Hemisphere (NH)
97 continental regions (e.g., Tarasick et al., 2019; Turnock et al., 2020). CMIP6 models simulate
98 large increasing trends of surface concentrations of O₃ and PM_{2.5} in East and South Asia with
99 an annual mean increase of up to 40 ppb and 12 μgm⁻³, respectively, over the historical periods
100 (1850-2014; Turnock et al., 2020). However, these studies found also that CMIP6 models
101 consistently underestimate PM_{2.5} concentrations in the NH, especially during the winter
102 months, and with larger variability near natural source regions, indicating missing sources
103 (e.g., HONO) of O₃ (e.g., Elshorbany et al., 2014).

104 Satellite observations have the advantage of large spatial and consistent temporal coverage.
105 Tropospheric columns of ozone (TrC-O₃), in Dobson unit (1 DU=2.69×10²⁰ molecules m⁻²),

106 are usually used to represent tropospheric ozone levels. The tropospheric column of a species
107 is the species' concentration integrated from the surface to the top of the troposphere, the
108 tropopause. The tropopause height is dynamically changing, and it varies over time, increasing
109 or decreasing as a function of several factors, including tropospheric and stratospheric
110 temperature (warming or cooling). Steinbrecht et al (1998) found that observed tropospheric
111 warming of 0.7 ± 0.3 K per decade leads to an increase in the tropopause high and a decrease
112 (at a rate of 16 DU/decade) in the observed column ozone levels. Similarly, after removing the
113 variations related to major natural forcings, including volcanic eruptions, ENSO (El Niño–
114 Southern Oscillation), and QBO (Quasi–Biennial Oscillation), Meng et al. (2021) concluded
115 that a continuous rise of the tropopause in the Northern Hemisphere (NH) from 1980 to 2020
116 is evident, which they related mainly to tropospheric warming caused by anthropogenic
117 emissions. Steinbrecht et al (1998) and Meng et al. (2021) calculate the same rate of tropopause
118 increase for the periods 1980-2000 and 1980-2020, respectively. We investigate the trends in
119 TrC-O₃ and ozone precursors at different column depths and determine their relationships.

120 Global models play a vital role in interpreting the observed trends in ozone precursors,
121 verifying the consistency of emission inventories with observed precursor concentrations, and
122 relating trends in ozone precursor emissions to ozone trends. Because satellite measurements
123 are often sensitive to species concentrations above the surface, models provide additional
124 information on the vertical distribution of ozone precursors needed to relate emissions or
125 surface trends to a column or free tropospheric observations. For example, chemical transport
126 models are used to relate Ozone Monitoring Instrument (OMI) NO₂ columns to surface NO₂
127 concentrations and their trends over the United States (e.g. Lamsal et al 2008, 2015; Kharol et
128 al, 2015) since they provide vertical information on the NO₂ distribution. Models are also used
129 to infer NO_x emission trends from observations (e.g. Richter et al., 2005; Stavrakou et al.,
130 2008; Miyazaki et al, 2016) or to examine whether simulations driven by state-of-the-art
131 emissions inventories can reproduce observed changes in NO_x (Itahashi et al., 2014;
132 Godowitch et al, 2010). Models also provide insight into the role of background NO₂ versus
133 local sources in relating satellite-observed NO₂ columns to NO_x emissions changes (Silvern et
134 al, 2019). Similarly, global models are vital for understanding trends in CO, since the lifetime
135 of CO allows both local emissions and long-range transport and the global background to
136 influence regional trends of CO and O₃. Duncan and Logan (2008) attributed the decreasing
137 CO in the NH from 1998-1997 to decreasing European emissions and highlighted the role of
138 Indonesian fires in driving interannual variability. Numerical models can also be used to
139 assimilate satellite CO observations to invert for CO emission fluxes, often highlighting
140 differences between bottom-up and top-down inventories (e.g., Kopacz et al., 2010; Fortems-
141 Cheiney et al., 2011; Elguindi et al., 2020; Gaubert et al., 2020). For instance, several modeling
142 studies found that the increasing emissions from China in recent years in some emission
143 inventories were inconsistent with the negative trends observed by MOPITT (Yin et al, 2015;
144 Strode et al., 2016; Zheng et al, 2019), while the decreases over the United States and Europe
145 are supported by the observed decrease in CO. Jiang et al (2017) and Zheng et al (2019) also
146 found that a decrease in biomass burning contributes to the negative CO trend in the NH. Mean
147 calculated O₃ burden using CMIP6 simulation (Griffiths et al, 2021) revealed an increase of
148 44% from 1850 to the mean of the period of 2005-2014 and by another 17% until 2100 using
149 the SSP370 experiments. Other sources of NO_x such as lightning and soil emissions play an
150 important role in controlling the O₃ budget, especially in low-NO_x regions. We investigate
151 these sources and the role they play in determining O₃ trends and variability on regional and
152 global scales, as well as their determining factors.

153 Previous literature demonstrates the importance of controlling the emissions of ozone
154 precursors to effectively reduce surface O₃ levels. Therefore, a thorough and rigorous
155 understanding of the trends and variability for O₃ precursors is of paramount importance for a
156 global abatement strategy of O₃ levels. In this study, we use ozonesonde, remote sensing, and
157 global models to evaluate tropospheric O₃ and O₃ precursor trends of CO, HCHO, and NO₂,
158 on regional and global scales.

159 **2. Methodology**

160 **2.1. Trend Analysis**

161 We analyze the historical trends of tropospheric ozone and its precursors CO, NO₂, and HCHO,
162 from 2005 to 2019. For trend analysis, we use two methods, the Quantile regression (QR)
163 method (Chang et al., 2023), and the Weighted Least Squares (WLS). For NO₂, CO, and HCHO
164 trends are calculated based on the QR method (Chang et al., 2023), as follows: (1) we first
165 compute the deseasonalized monthly time series of NO₂ and HCHO tropospheric columns
166 (hereafter referred to as TrC-NO₂, TrC-HCHO), and CO atmospheric column (TC_CO), (2) we
167 use the quantile regression method for computing the trend, focusing here on the median, and (3)
168 uncertainties at a 95% confidence level are estimated using the block bootstrapping approach,
169 through 1000 iterations with blocks size of $N^{0.25}$ with N the number of monthly values. They are
170 calculated over a 1°x1° grid and only in cells where at least 75% of the monthly values are
171 available. TC_CO column (see sec. 2.2.1) time series trends are also calculated as Weighted
172 Least Squares (WLS) of the monthly anomaly, weighted by the monthly regional standard
173 deviation (for comparison with the QR method). The tropospheric ozone column (TrC-O₃),
174 trends are calculated based on the WLS method. Tropospheric columns of satellite observations
175 are calculated based on the WMO thermal definition of the tropopause. To account for varying
176 tropospheric column definitions used in previous literature, we also evaluate the trends at varying
177 column depths.

178 **2.2. Data resources**

179 In this section, we present the different data repositories and their characteristics.

180 **2.2.1. Satellite data**

181 A list of the applied satellite data products and their resolution is shown in Table 1. For
182 Tropospheric ozone data, we use the Ozone Monitoring Instrument/Microwave Limb Sounder
183 (OMI/MLS) product (Ziemke et al., 2006). The OMI/MLS product is the residual of the OMI total
184 ozone column and the MLS stratospheric ozone column, available as gridded monthly means. The
185 OMI/MLS tropospheric column ozone product applies all necessary data quality flags to both OMI
186 total ozone and MLS profile ozone; the OMI/MLS product further includes cloud filtering by
187 omitting all scenes with OMI reflectivity greater than 0.30. The tropospheric NO₂ column
188 retrievals used were the QA4ECV project (<http://www.qa4ecv.eu/ecvs>) version 1.1 level 2 (L2)
189 product for OMI (Boersma et al., 2017a), GOME-2 (Boersma et al., 2017b), and SCIAMACHY
190 (Boersma et al., 2017c). The ground pixel sizes of the OMI, GOME-2, and SCIAMACHY
191 retrievals are 13 km×24 km, 80 km×40 km, and 60 km×30 km, with local Equator overpass times
192 of 13:45, 09:30, and 10:00 LT, respectively. We also use HCHO tropospheric columns retrieved
193 from OMI (De Smedt et al. 2018) from the QA4ECV project. Atmospheric total column CO
194 daytime observations were obtained from the MOPITT instrument aboard the Terra Satellite
195 (Barret et al., 2003; Buchholz et al., 2017). Monthly daytime L3 data were obtained at 1° gridded
196 horizontal resolution from the NASA Langley Research Center Atmospheric Science Data Center

197 (ASDC, 2024), using version 9 (V9) retrievals, and the joint near-infrared/thermal-infrared product
 198 (Deeter et al., 2022). Low-quality data were excluded by applying the provided quality flag.

199

200 Table 1 Satellite data products and their reference periods.

Parameter	Resolution (Satellite pixel size)	Instrument/Platform	Reference Period	Reference
NO ₂	1°x1° (13 km x 24 km)	OMI/Aura	2005–2020	Boersma et al., 2017a
NO ₂	1°x1° (40 km x 80 km)	GOME-2/METOP-A	2007–2018	Boersma et al., 2017b
NO ₂	1°x1° (30 km x 60 km)	SCIAMACHY/ENVISAT	2005–2011	Boersma et al., 2017c
CO	1°x1° (22 km x 22 km)	MOPITT/TERRA	2002–2020	Deeter et al., 2022
HCHO	1°x1° (13 km x 24 km)	OMI/Aura	2004–2020	De Smedt et al., 2018
Ozone	1°x1°	OMI/MLS	2004–2020	Ziemke et al., 2006

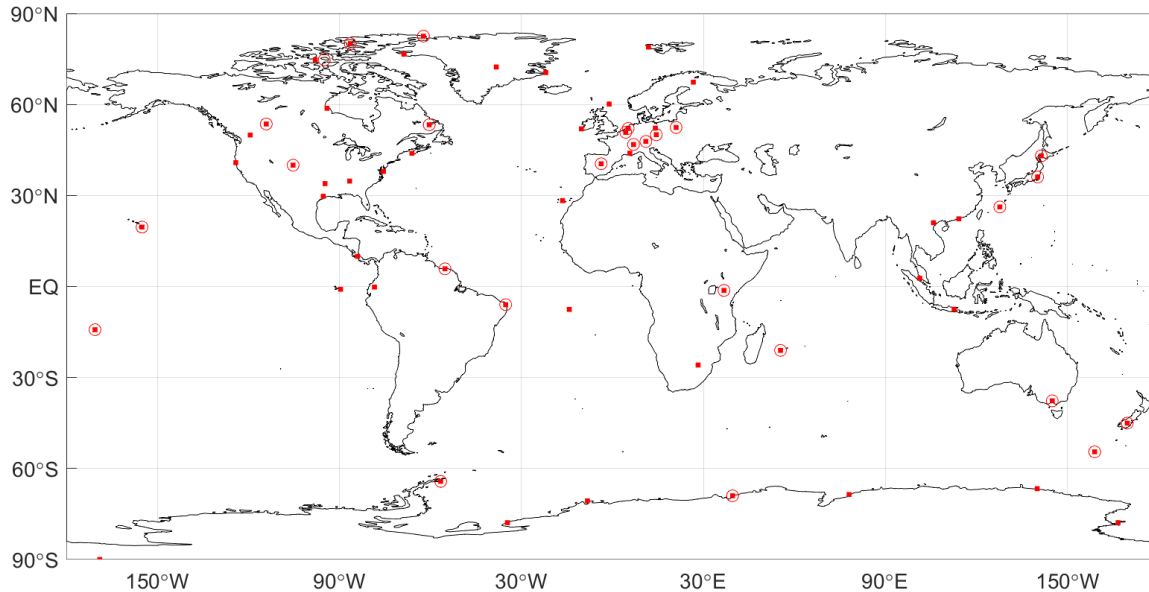
201

202 2.2.2. Ozonesonde Data

203 Direct sampling of ozone throughout the atmospheric column by ozonesondes on board of high-
 204 altitude balloons is a primary source of information of the ozone abundance and changes in the
 205 free troposphere. Ozonesonde data have been used extensively for satellite ozone product
 206 validations, trend analyses, and as a priori climatology profiles for satellite retrieval algorithms
 207 (McPeters and Labow, 2012; Labow et al., 2015; Hubert et al., 2021; Christiansen et al., 2022;
 208 Newton et al., 2016). Ozonesondes networks around the globe have been providing the ozone
 209 community with accurate in situ measurements of high vertical resolution (100-m) for the last 5
 210 decades in the Northern Hemisphere (Krizan and Lastovicka, 2005), nearing 3 decades at
 211 stations in the tropics (Thompson et al., 2017), and in the last decade, new efforts are
 212 contributing with data from undersampled regions such as the tropical Andes (Cazorla and
 213 Herrera, 2022). Other important contributions include dedicated campaigns for regional studies
 214 (e.g. Newton et al., 2016; Fadnavis et al., 2023). Figure 1 shows a map with ozonesonde stations
 215 around the globe whose data are publicly available from data providers (station names,
 216 coordinates, and links for data access in the Supplementary Material, Table S1). In this work, we

217 present a review of ozonesonde trends calculated and published in previous studies (Wang et al.,
218 2022 and Christiansen et al., 2022).

219



220

221 Figure 1: Ozone-sounding stations around the globe (red squares) whose data are publicly
222 available (Table S1). Stations that meet the criteria to calculate trends (Wang et al., 2022) are
223 circled in red.

224

225 2.2.3. Model simulations of ozone precursors and their vertical distribution

226 Model simulations provide information on the vertical distribution of trace gases that can help
227 interpret the observed columns. Here, we use a Goddard Earth Observing System (GEOS) Earth
228 System Model (Molod et al, 2015) simulation run with the GMI chemistry mechanism (Duncan
229 et al, 2007; Strahan et al, 2007; Nielsen et al, 2017) to simulate the contributions of the lower,
230 middle, and upper troposphere to the tropospheric columns of ozone and its precursors. The
231 model configuration is described in Fisher et al (2024) and summarized here. The MERRA-2
232 reanalysis (Gelaro et al., 2017) constrains the GEOS-GMI meteorology. The GEOS-GMI
233 meteorology is replayed to the MERRA-2 meteorology as described in Orbe et al (2017).
234 Anthropogenic emissions of NO₂, CO, and VOCs are based on the MACCity inventory (Granier
235 et al, 2011) through 2010 and the RCP8.5 emissions afterward, with NO₂ emissions scaled based
236 on OMI. The emissions are downscaled to higher resolution using the EDGAR 4.2 emission
237 inventory (Janssens-Maenhout et al., 2013). Biomass burning emissions for the analysis period
238 come from the Fire Energetics and Emissions Research (FEER) product (Ichoku and Ellison,
239 2014). Liu et al (2022) evaluated another GEOS simulation with GMI chemistry with satellite
240 observations of TrC-O₃, TrC-NO₂, TrC-HCHO, and TC-CO.

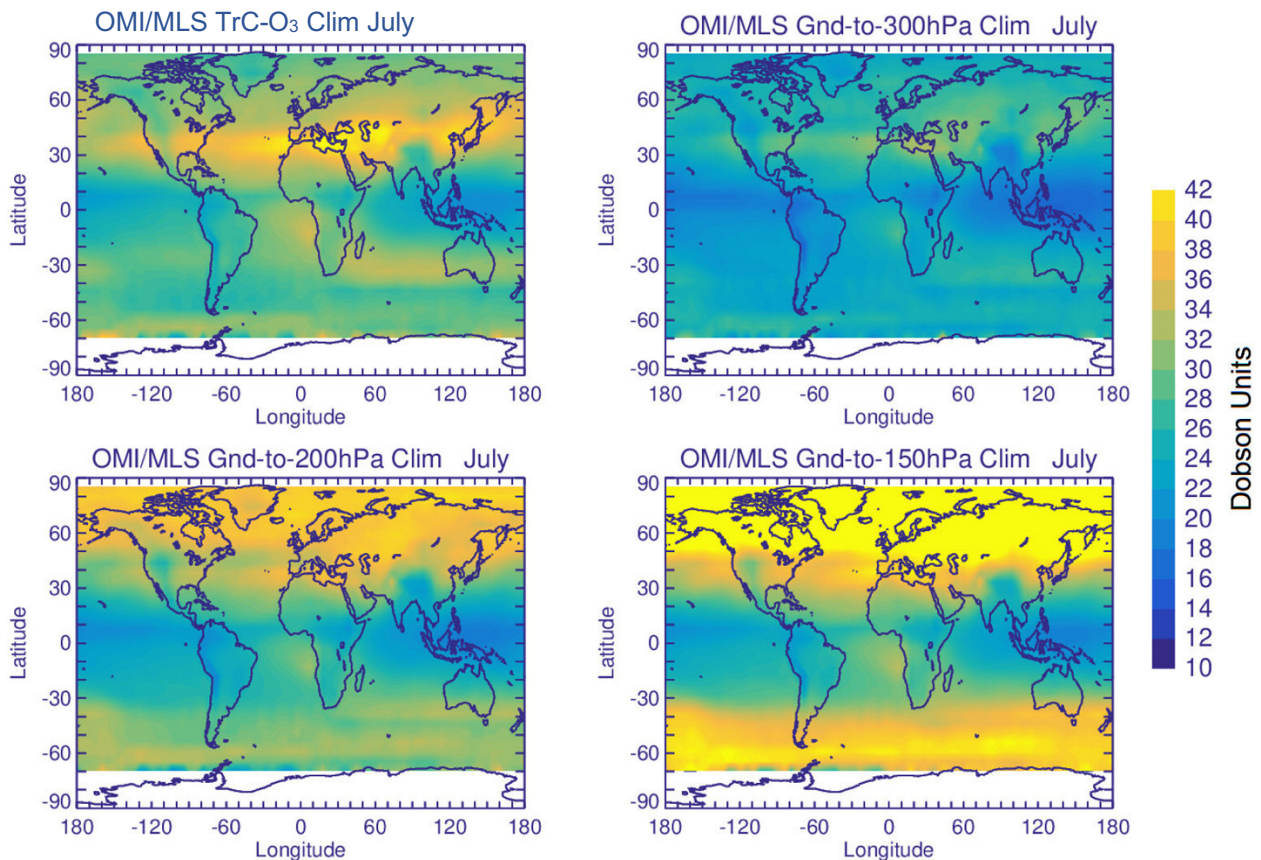
241 3. Data Analysis and Discussion

242 3.1. TrC-O₃ Sensitivity to Tropopause

243 Calculated TrC-O₃ depends on several factors such as tropospheric ozone levels, atmospheric
244 warming (e.g., due to GHG emissions) or cooling (stratospheric or tropospheric (e.g., after major
245 volcanic eruptions), and tropopause height (TH). Atmospheric warming or cooling can lead to a

246 decrease or an increase, respectively, of TrC-O₃ due to the respective change in the TH. Several
 247 methods are used to determine the TH. The WMO thermal definition for the first TH, the lowest
 248 altitude level at which the lapse rate decreases to 2° K km⁻¹ or less, provided that the average
 249 lapse rate between this level and all higher levels within 2 km does not exceed 2° K km⁻¹. A
 250 second tropopause may be also found if the lapse rate above the first tropopause exceeds 3°K
 251 km⁻¹ (WMO, 1992; Hoffmann and Spang (2022)). Other studies define the TH based on fixed
 252 pressure levels (from ground to 150, 200, 300, and 400 hPa). Mean OMI/MLS TrC-O₃ values in
 253 July (2005-2019) calculated based on the WMO thermal definition, are shown in Figure 2. TrC-
 254 O₃ values are comparable to previously reported CMIP6 and satellite measurements (Griffiths et
 255 al., 2021). Partial ozone columns (OC) calculated from the ground to different pressure levels,
 256 150, 200, and 300 hPa show increasing OC values with increasing column depth, with calculated
 257 OC at 150 and 200 hPa being the closest to the TrC-O₃ WMO values, still overestimating OC in
 258 the northern hemisphere (50-90° N), especially for the 150 hPa OC, see Figure 2.

259

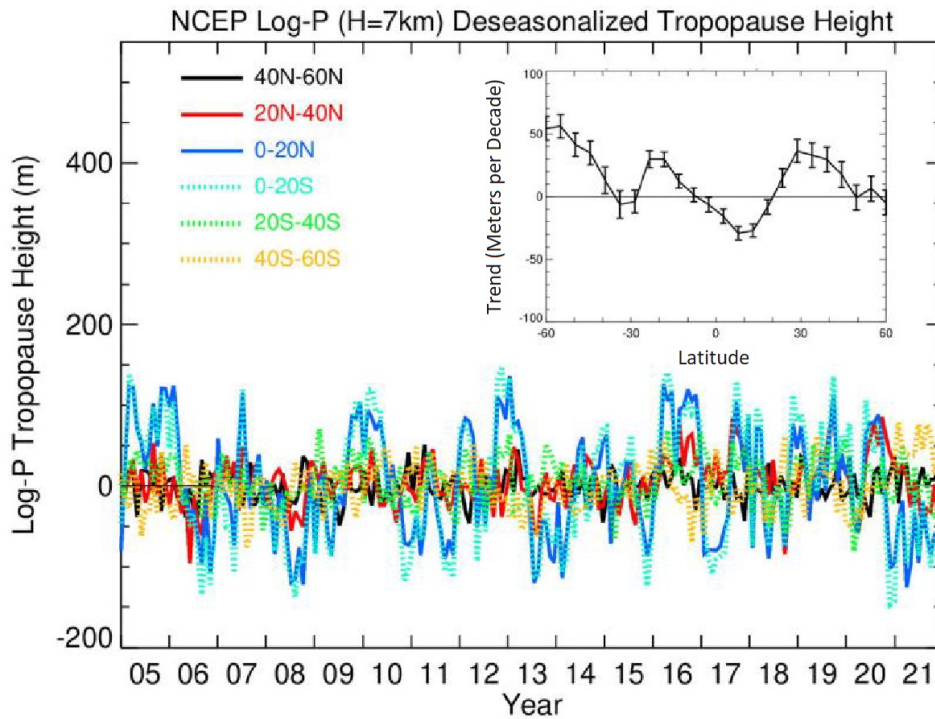


260
 261 Figure 2: Global Mean (2005-2019) Column Ozone based on the WMO definition, and for
 262 different column depths.

263
 264 Steinbrecht et al (1998) found that observed tropospheric warming of 0.7 ± 0.3 K per decade
 265 leads to an increase in the TH and a decrease in total ozone. They also calculated a decrease of
 266 16 DU per kilometer increase in TH. These results indicate the importance of TH on calculated
 267 long-term ozone trends. This could also affect comparisons between trends calculated based on
 268 different TrC-O₃ definitions and near-surface ozone levels. The time series of deseasonalized TH
 269 from 2004 to 2021 are shown in Figure 3 together with their zonal mean trends. Trends in TH are

270 positive reaching 60 meters/decade except in a narrow band in the tropics from 10°S to 20°N and
 271 at 30°S, where TH decreases at a rate up to 30 meters/decade. TH in the tropical regions is also
 272 characterized by high variability (see Figure 3). These results are also consistent with recent
 273 reports showing a positive trend of TH from 20-80°N at a rate of 50-60 m/decade (Meng et al.,
 274 2021). They related this increase primarily to tropospheric warming. These results show that
 275 using a fixed pressure level for the tropopause may not be accurate given the change in TH over
 276 time. In the following sections, tropospheric columns will be calculated based on the WMO
 277 tropopause definition.

278



279

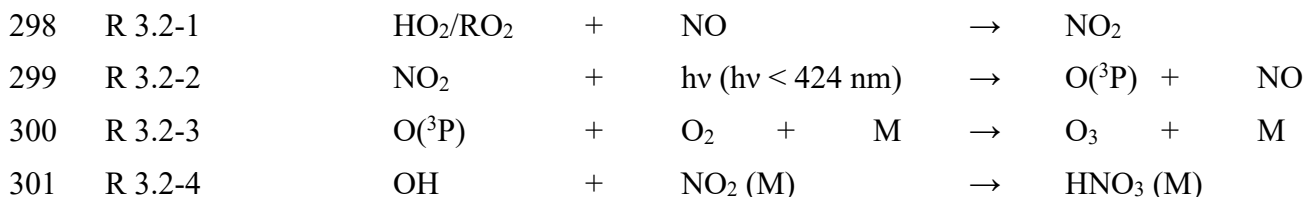
280 Figure 3: National Centers for Environmental Prediction (NCEP) WMO (2K/km) tropopause
 281 log-P height time series with trends (meters/decade) embedded.

282

283 3.2. Spatial Distribution of O₃ and its Precursors

284 Tropospheric O₃ results from in-situ photochemical formation and STE. In-situ O₃ results from
 285 the photolysis of NO₂. Therefore, the sources and fate of NO₂ in the atmosphere determine O₃
 286 burden and distribution. NO₂ is formed from the reaction of hydrogen peroxy (HO₂) and alkyl
 287 peroxy (RO₂) radicals with NO (R 3.2-1). While photolysis of NO₂ is the main source of ozone,
 288 high NO₂ levels can suppress O₃ levels as NO₂ reacts with OH radical forming HNO₃ (R 3.2-2 to
 289 R 3.2-4), thus reducing the oxidation rate of hydrocarbons and respectively HO₂ and RO₂ levels,
 290 leading to a net loss of O₃ (e.g., Finlayson-Pitts and Pitts, 2000; Elshorbany et al., 2010,
 291 Archibald et al., 2020). Ozone production efficiency is calculated as the ratio of the number of
 292 NO₂ molecules photolyzed to form O₃ to that lost due to the reaction with OH forming HNO₃.
 293 Under NO-sensitive conditions, the decrease in NO_x leads to a reduction in OH, HCHO, and O₃.
 294 However, under high NO conditions, a reduction in NO_x could lead to an increase in
 295 photochemical products, OH, HCHO, and O₃ because a reduction in NO₂ leads to a decrease in

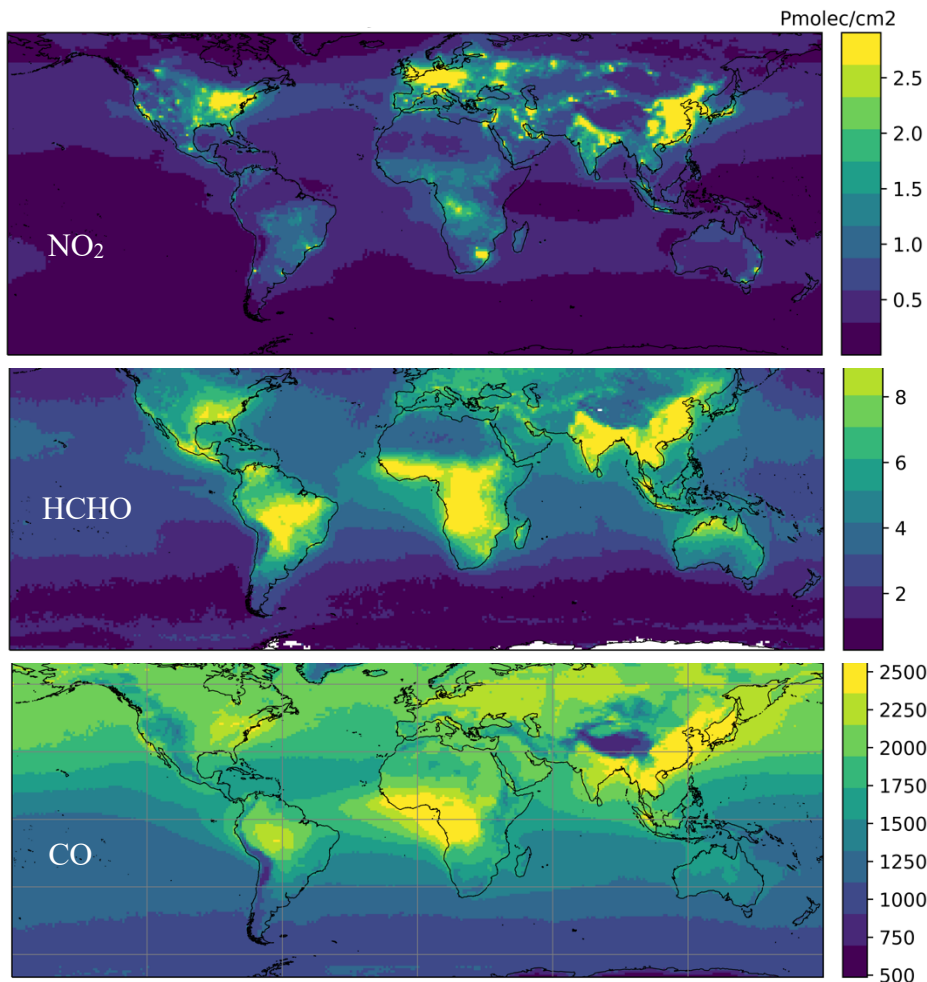
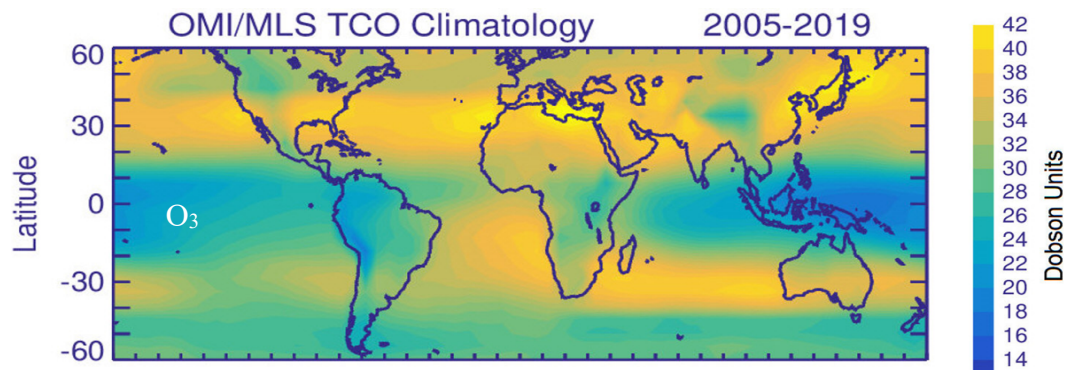
296 OH loss rate, thus higher HO₂ and RO₂ production (Elshorbany et al., 2012; Archibald et al.,
297 2020).



302

303 The observed mean tropospheric columns of O₃, NO₂, and HCHO and atmospheric column of
304 CO from 2005 to 2019 are shown in Figure 4. The unit for column number density is
305 Pmolec/cm² (×10¹⁵ molecules per square centimeter), except for TrC-O₃, which is Dobson. NO₂
306 concentration has decreased since 2005 in North America, Europe, and Australia, mainly due to
307 strict measures to reduce air pollution (Lamsal et al., 2015). Since O₃ is a photochemical product
308 that is formed based on non-linear chemistry, a reduction in NO₂ may lead to an increase or
309 decrease in tropospheric O₃ levels based on the dominant photochemical regime in the respective
310 region. In addition, tropospheric ozone levels may be affected by STE especially in the middle
311 and upper troposphere (Li et al., 2024), as well as LRT, especially in the free troposphere (e.g.,
312 Glotfelty et al, 2014; Itahashi et al., 2020). The highest values of the NO₂ tropospheric column
313 are in the northern hemisphere between 10 °N and 50°N, especially over the eastern US, northern
314 Europe, and east and south Asia, with elevated levels in the Southern Hemisphere (SH) between
315 10 and 30°S, especially in sub-Saharan Africa, and Brazil. TrC-O₃ is also highest over the band
316 of 20-50° N, especially over the eastern coast of the US, southern Europe, and east Asia. Some
317 differences exist between TrC-O₃ and TrC-NO₂ spatial patterns which is due to factors including
318 different lifetime, photochemical sensitivity (see sec. 3.4), and STE. On average, the northern
319 hemisphere has higher TC-CO than the southern hemisphere due to a larger number of sources
320 (Buchholz et al., 2021). Additionally, high amounts of CO are found in regions with large
321 anthropogenic sources (e.g., eastern China) or in regions with large and regular fire seasons (e.g.,
322 central Africa) (Buchholz et al., 2021). HCHO and CO show a similar spatial pattern over
323 western Africa due to emissions from biomass burning (Marais et al., 2012, Buchholz et al.,
324 2021). In the following sections, global and regional trends of TrC-O₃ are investigated along
325 with tropospheric ozone precursors.

326



327

328 Figure 4: Mean (2005-2019) of TrC-O₃, TrC-NO₂, TrC-HCHO, and TC-CO.

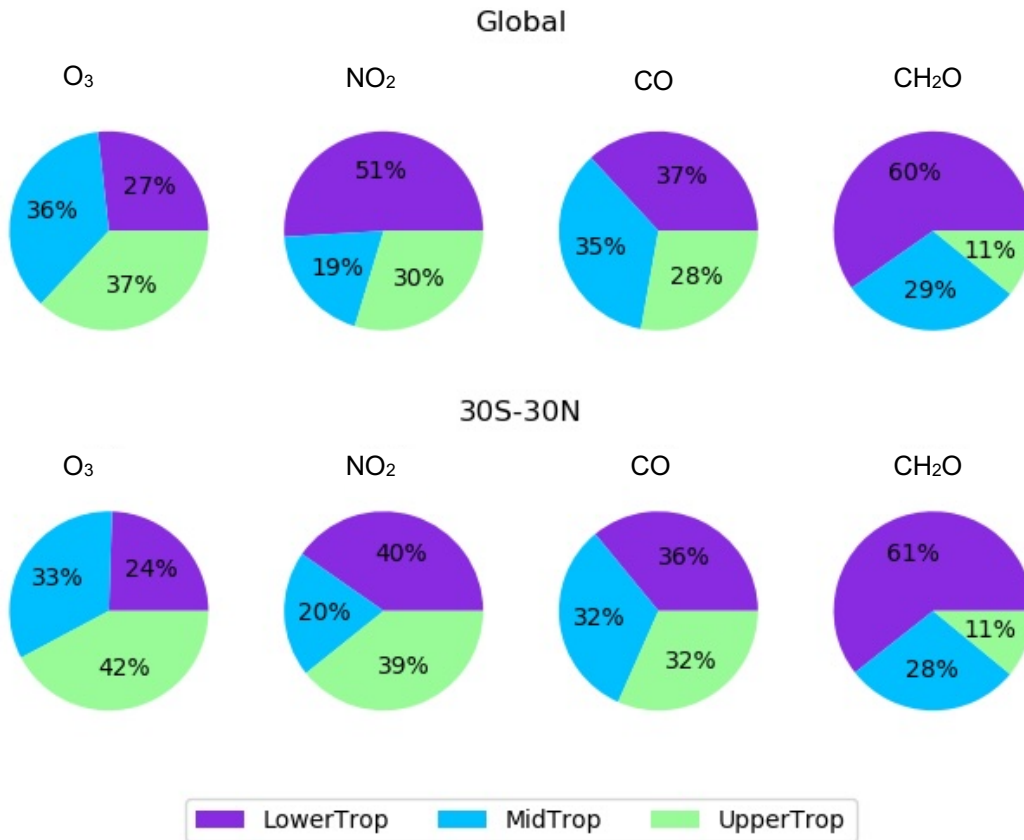
329

3.3. Simulated O₃ Precursors

330 Ozone and its precursors differ in their vertical distribution through the troposphere. In this
 331 section, we use the GEOS -simulations to show how the lower, middle, and upper troposphere
 332 contribute to the simulated columns of O₃ and its precursors to complement the column
 333 information from satellites. Figure 5 shows the simulated mean (2005-2019) contributions to
 334 tropospheric columns of O₃, NO₂, formaldehyde, and CO, partitioned into the lower (up to
 335 700hPa), middle (700-400hPa), and upper (400hPa to tropopause) portions of the troposphere for
 336 the tropical band (30°S:30°N) and the global mean. The middle and upper troposphere make

337 large contributions to the simulated TrC-O₃ and its variability (Figure 5). The lower troposphere
 338 makes the largest contribution to the TrC-HCHO since it is mainly a photochemical product
 339 (e.g., Elshorbany et al., 2009), and all three levels make substantial contributions to the CO
 340 column. Globally, the relative contributions for TrC-O₃, TrC-HCHO and CO are similar to those
 341 of the tropics. However, for TrC-NO₂ the lower troposphere makes a smaller contribution in the
 342 tropics than globally.

343



344

345 Figure 5: Simulated average (2005-2019) contributions to the tropospheric columns of O₃, NO₂,
 346 formaldehyde, and CO from the lower (surface-700hPa), middle (700-400hPa), and upper
 347 troposphere (400hPa-tropopause) using NASA GEOS-GMI. The top row is for the global mean,
 348 while the bottom row is averaged from 30°S-30°N.

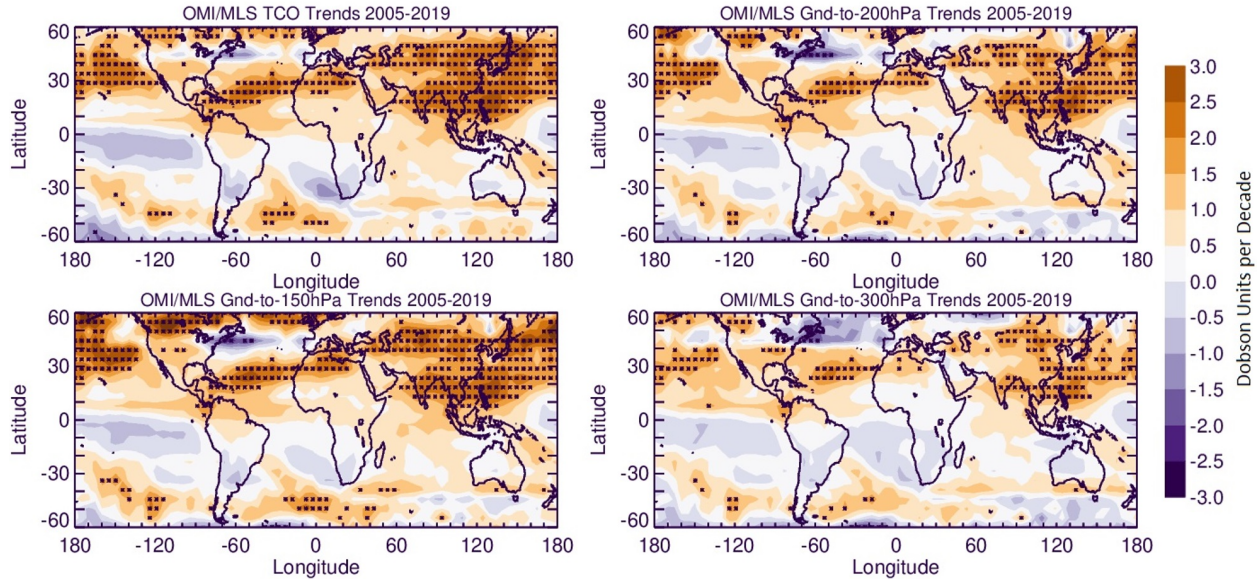
349 3.4. Tropospheric Trends

350 3.4.1. Global Tropospheric Ozone

351 Global TrC-O₃ trends calculated for different column depths are shown in Figure 6. Compared to
 352 TrC-O₃, OC trends up to 150 hPa seem to be the closest despite OC values being much higher
 353 than that of the TrC-O₃ (Figure 2). All trends with high confidence, HC (at 95% confidence) are
 354 positive indicating increasing trends of ozone columns, regardless of the tropopause height. Low
 355 confidence, LC (at 2 σ levels) decreasing TrC-O₃ trends were also found in some locations, e.g.,
 356 South Australia, South Africa, and the northeastern coast of the US. Increasing trends in the
 357 northern midlatitudes may also be partially related to STE (Willimas et al, 2019; Li et al., 2024).
 358 While the annual trends inform about overall trends, seasonal trends provide insights into local
 359 chemistry and meteorology. For example, during the boreal summer months, June, July, and

360 August (JJA), TrC-O₃ HC trends are similar to the annual trends except for HC decreasing trends
 361 over South America and South Africa and HC increasing trends over the west and central Africa
 362 and Central America (Figure S7). During the boreal winter months, HC trends are also similar to
 363 the annual trends (Figure 6) except for HC increasing trends over Europe, North America, South
 364 America, and South Africa (Figure S7).

365

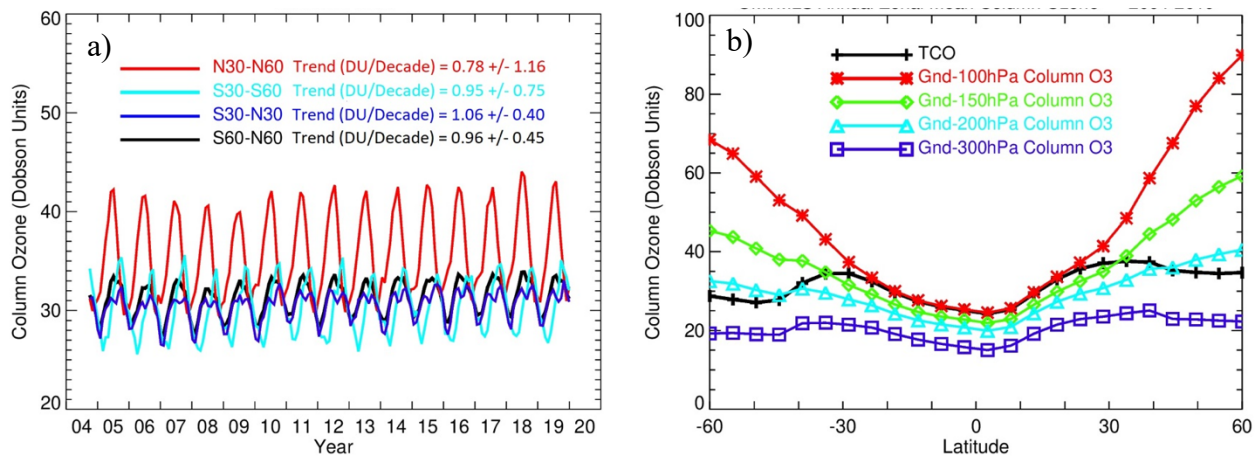


366
 367 Figure 6: Trends in tropospheric column ozone, based on the WMO thermal definition, and the
 368 trends on ozone columns (from ground to 150, 200, and 300 hPa). Trends are calculated based on
 369 deseasonalized monthly data from 2005 to 2019. Asterisks denote 95% confidence trends.

370

371 The time series of OMI/MLS TrC-O₃ averaged over several latitudinal bands and at different
 372 column depths are shown in Figure 7. Zonal mean TrC-O₃ compares well with partial ozone
 373 columns in the tropics (from 30°S to 30°N) with the OC of up to 300 hPa differing by about 10
 374 DU from the TrC-O₃ (Figure 7b). The lowest TrC-O₃ trends are located in the northern
 375 hemisphere (30 – 60°N) at 0.78 ± 1.16 DU/decade, followed by the southern hemisphere (30-60°S
 376 (0.95 ± 0.75 DU/decade) and the tropical band (30-30°N (1.06 ± 0.40 DU/decade). In addition, the
 377 continental trends over Australia, South Africa, and South America in the 30 °S -60°S band are
 378 essentially negative and the positive trends in this band are contributed mainly by oceanic
 379 regions (see Figure 6). The positive trends in the 30°N -60°N band are slightly offset by the
 380 negative trends over the northeastern US and western Europe (see Figure 6).

381

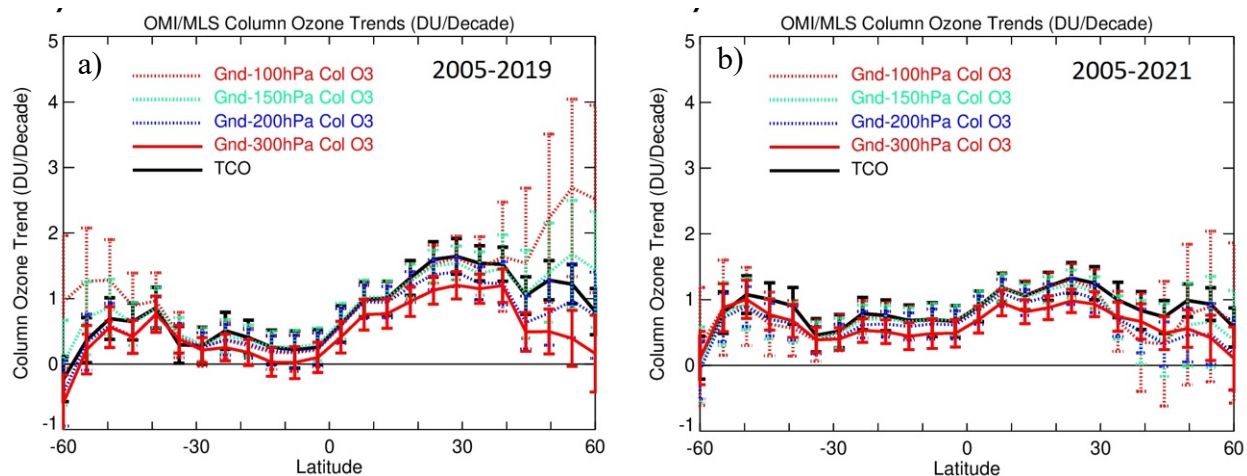


382

383 Figure 7: Time series and zonal mean trends of OMI/MLS TrC-O₃ in different latitudinal bands
 384 (left) and zonal mean of different column depths (right) from 2005-2019.

385 Observed trends for the time period before COVID-19 (2005-2019) show that OC trends
 386 were highest in the northern latitudes (0-30° N) reaching about 1.5 DU/decade, followed by the
 387 northern midlatitudes 30-60°N (Figure 8). The high trends in the 30-60°N band are dominated by
 388 transpacific impacts as well as some impacts from East Asia. The positive trends in the southern
 389 hemisphere (0-30° S) are mainly over Amazonia and Southeast Asia, being offset by small
 390 negative trends over Western Australia and South Africa. The trends during the time period
 391 (2005-2021) show a decline in O₃ column trends in the northern hemisphere but a slightly
 392 increasing trend in the southern hemisphere (Figure 8b). The decreasing trends in the northern
 393 hemisphere during the COVID-19 is consistent with previous literature showing a decrease in
 394 several pollutants including NO₂ and O₃ due to the extended lockdown periods imposed during
 395 the pandemic (e.g., Bauwens et al., 2020; Elshorbany et al., 2021; Steinbrecht et al., 2021; Putero
 396 et al., 2023). The decrease of NO₂ in some parts of Europe and the northeastern USA led to a
 397 decrease in tropospheric O₃.

398 Zonal mean trends (Figure 8) show that OC up to 150 hPa is almost identical to that of
 399 TrC-O₃ except for the high latitudes 45°-60° S and 45°-60° N. The decreasing trends above 30°N
 400 and 30°S are due to the offsetting impact of negative trends over the northeastern US and western
 401 Europe in the north, and Australia and South Africa in the south, respectively. This impact is less
 402 apparent in the 150 hPa OC due to the lower positive trends in that band compared to TrC-O₃.
 403 The 200 hPa OC comes next with a very good agreement from 60° S to 10° N. followed by the
 404 100 hPa which is only in good agreement from 30° S to 30°N, while the 300 hPa OC was the
 405 farthest from the TrC-O₃. The decrease of O₃ in the northeastern US and western Europe is
 406 consistent with decreasing NO₂ trends and NO-sensitive conditions dominating these regions.
 407 The decreasing trends of NO₂ (see below) are due to the successful measures applied since 2004
 408 to mitigate air pollution in these regions. The increase of O₃ in the western US maybe due to
 409 LRT from eastern Asia (e.g., Itahashi et al., 2020).



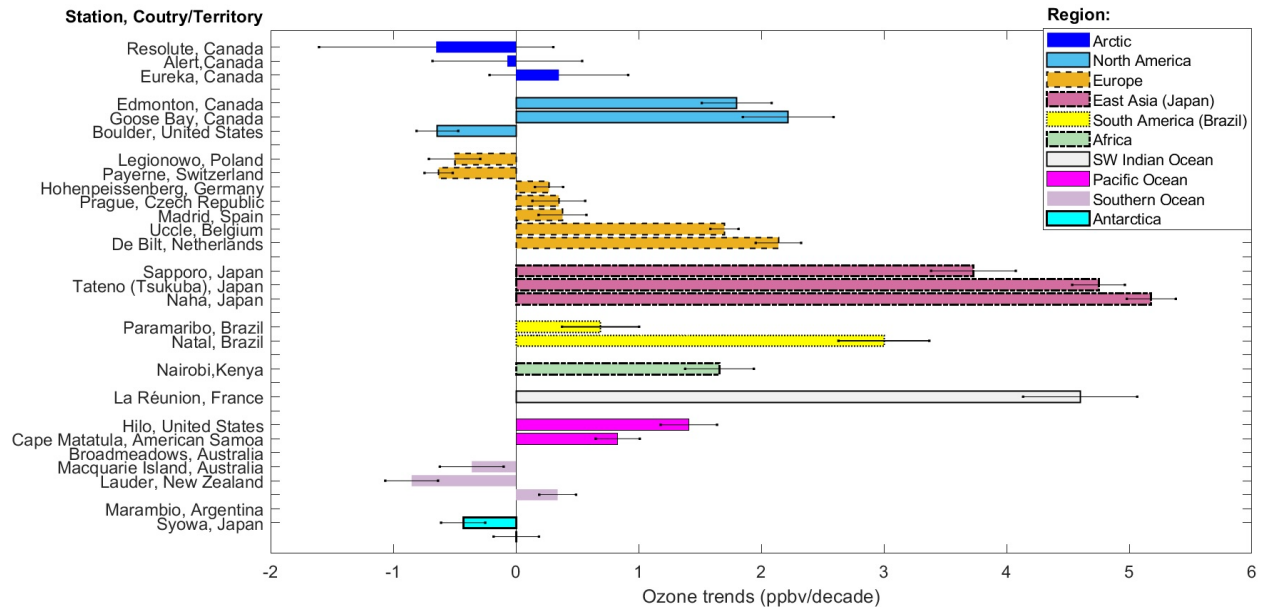
410
 411 Figure 8: Tropospheric column ozone (TrC-O₃) and trends for different column depths before the
 412 COVID-19 pandemic (2005-2019) and including the pandemic (2005-2021).

413
 414 **3.4.2. Free tropospheric trends**

415 Trends of ozone in the free troposphere presented here are based on previous work published in
 416 the literature. Despite the high stability of ozonesonde measurements across the global networks
 417 over several decades (Stauffer et al., 2022), the spatial sparsity of sounding stations and non-
 418 uniform sampling frequency among sites is a limitation in using these data to produce trends.
 419 These shortcomings have constrained the ability to include data from many stations in previously
 420 published analyses. For example, Chang et. al (2020) estimated that at least 18 profiles per
 421 month are needed at a single station to calculate accurate long-term trends, while uncertainty
 422 increases at lower sampling rates (Chang et al 2024). However, such high sampling frequency is
 423 only achieved at three European stations (Hohenpeissenberg, Germany; Payerne, Switzerland,
 424 and Uccle, Belgium), while the rest of the global stations work at lower sampling rates.
 425 Nonetheless, high-quality ozonesonde observations continue to be the gold standard against
 426 which satellite measurements are validated. Likewise, ozonesonde data continue to provide
 427 spaceborne observations with climatological feedback. Thus, recent studies have softened the
 428 sampling frequency criteria in order to take advantage of the valuable data set collected by the
 429 global ozonesonde networks. For example, the latest trend studies establish the minimum
 430 frequency requirement to calculate trends to at least three profiles per month (Wang et al., 2022;
 431 Christiansen et al., 2022) with at least eight months of sampling in a year, and at least 15 annual
 432 means for an analysis of about two decades (Wang et al., 2022). With these criteria, recent
 433 ozonesonde trend analyses indicate that ozone concentration increased globally by 1.8+/-1.3
 434 ppbv/decade in the free troposphere within 800 to 400 hPa (Christiansen et al., 2022). However,
 435 there is high regional variability, as illustrated in Figure 9 where ozone trends published by
 436 Wang et. al. (2022) (1995-2017 data between 950-250 hPa) are organized by regions and
 437 stations. For example, ozone in East Asia (Japan) has been increasing at a rate of 3.5 to 5
 438 ppbv/decade, particularly since 2010 (Christiansen et al., 2022), which may lead to transpacific
 439 LRT of O₃ to the western US (e.g., Itahashi et al., 2020). Over the Southwestern Indian Ocean
 440 (La Réunion), trends are of similar magnitude (>4.5 ppbv/decade). In tropical South America,
 441 over the Atlantic basin region (Paramaribo and Natal), sounding measurements also show ozone
 442 increases by almost 3 ppbv/decade (Natal), but other regions in South America continue to lack
 443 sufficient measurements to produce trends. At tropical stations in Africa (Nairobi) and the

444 Pacific Ocean (Hilo and American Samoa) trends are also positive, although of lower
 445 magnitudes (0.83-1.7 ppbv/decade). In contrast, polar stations both at the Arctic and Antarctica
 446 as well as the Southern Ocean show overall decreasing ozone concentrations to low-confidence
 447 trends. Exceptions are the Eureka station in Canada and Lauder station in New Zealand, which
 448 both show slight ozone increases (less than 0.5 ppbv/decade). The direction of regional trends by
 449 Wang et. al. (2022) is consistent with regional trends presented in similar independent research
 450 (Christiansen et al., 2022). As atmospheric composition continues to become modified under the
 451 current regime of climate change, building consistent and longer time series of ozonesonde
 452 measurements at other regions will continue to be an important source of firsthand information to
 453 assess tropospheric ozone changes and trends.

454



455

456 Figure 9: Ozone trends in the free troposphere from ozonesonde measurements calculated by
 457 Wang et. Al. (2022) and organized by region and station. Data covers the 1995-2017 period
 458 within 950 to 250 hPa. Error bars show 1- σ uncertainty. The coordinates of ozonesonde stations
 459 are listed in Table S1.

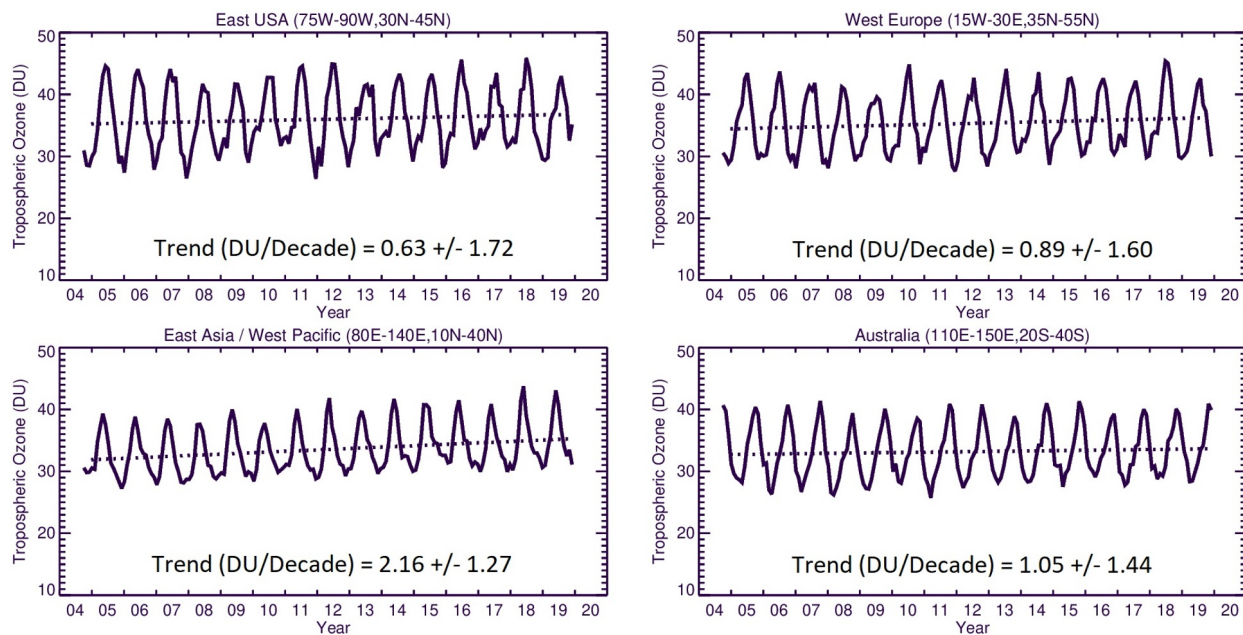
460

461 3.4.3. Regional Ozone Trends

462 As shown in Figure 10, the highest OMI/MLS regional trend is observed over East Asia
 463 (2.16 ± 1.27 DU/decade) while the lowest trend is calculated over Eastern USA (0.63 ± 1.72)
 464 followed by Western Europe (0.89 ± 1.60) and Australia (1.05 ± 1.44) DU/decade. We next
 465 calculate the monthly trends from the GEOS-GMI simulation to investigate how the simulated
 466 trends vary through the tropospheric column.

467

468



469

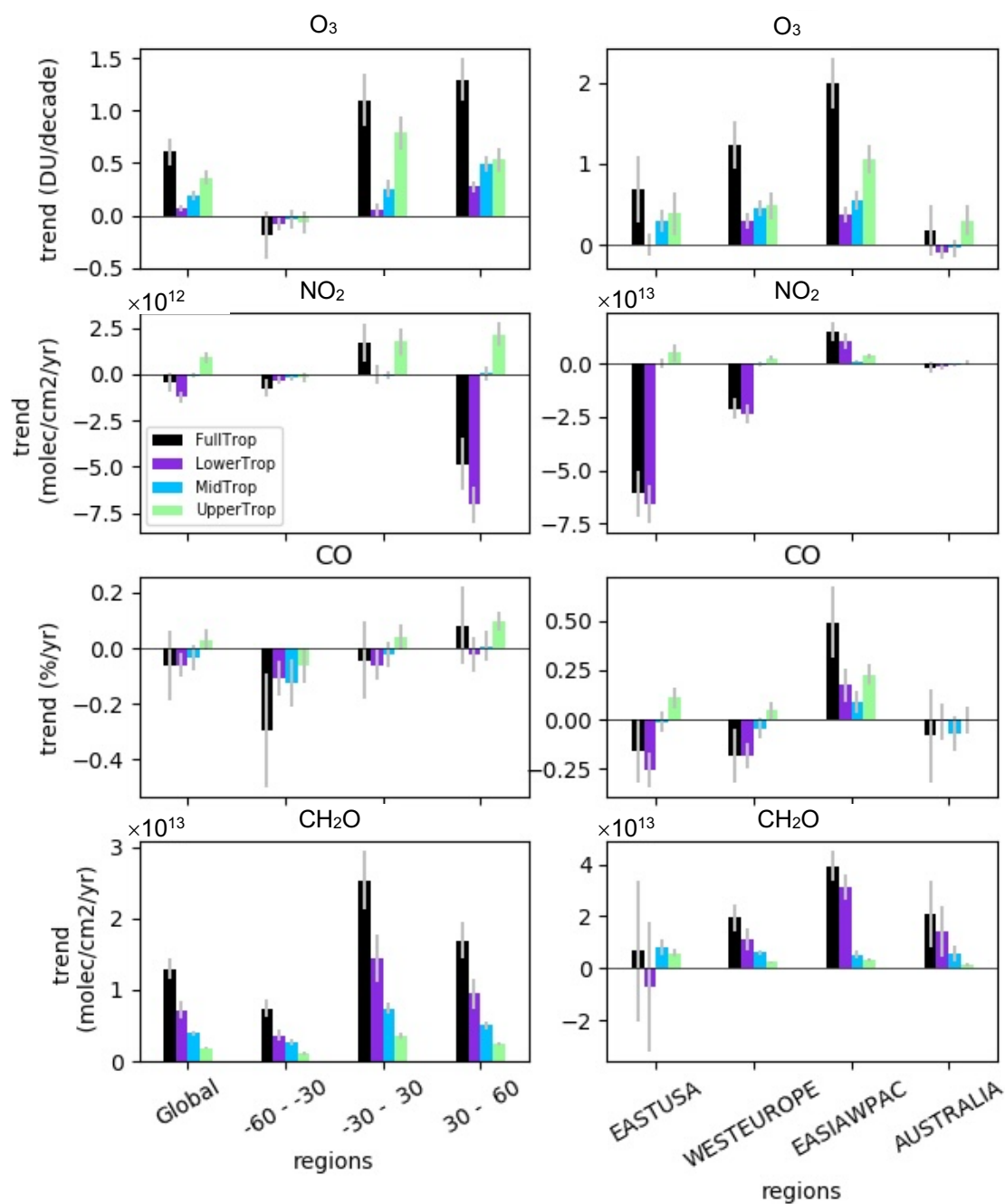
470 Figure 10: OMI/MLS observed regional mean trends of TrC-O₃.

471

472 The simulated trends in partial columns (lower, middle, and upper troposphere), as well as the
 473 TrC-O₃, TrC-NO₂, TrC-HCHO, and TC-CO from 2005 to 2019, are shown in Figure 11. The
 474 simulated tropospheric columns of TrC-O₃ and TrC-HCHO show a positive trend in most
 475 regions (Figure 11), consistent with the results of Liu et al (2022) using a different GEOSCCM
 476 simulation. Liu et al (2022) highlighted the importance of formaldehyde trends for analyzing the
 477 simulated trends in tropospheric ozone. Considering different latitude bands, the highest trends
 478 are simulated between 30° S and 60° N, consistent with calculated trends based on satellite
 479 observations (see sec. 3.4). In contrast, the simulated NO₂ and CO trends are mostly negative,
 480 although positive trends are simulated over East Asia. The largest NO₂ negative trends are in the
 481 northern hemisphere between 30°N and 60°N. The decrease in NO₂ trends is consistent with the
 482 successful measures to curb emissions of pollution criteria in the US and Europe. The increased
 483 trends in TrC-O₃ but decreased trends in TrC-NO₂, and TC-CO might indicate STE contribution
 484 (Trickl et al., 2020; Li et al., 2024) in addition to the local chemistry.

485

486



487

488 Figure 11: Global and regional trends in O₃, NO₂, CO, and HCHO calculated from the GEOS-
 489 GMI simulation for the tropospheric column (black), lower troposphere (purple), middle
 490 troposphere (blue), and upper troposphere (green) from 2005 to 2019. The lower, middle, and
 491 upper troposphere are defined as in Figure 5.

492

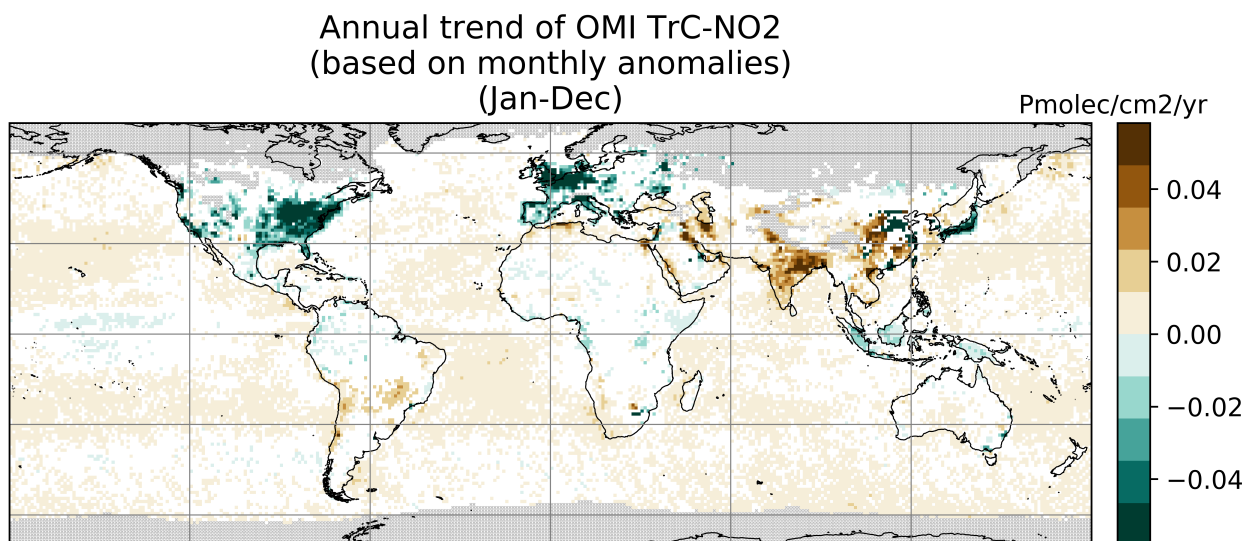
493 $\times 10^{12}$
 The GEOS-GMI simulation provides an estimate of the relative contribution from different
 494 portions of the tropospheric column to the column trends and shows that this contribution varies
 495 by region and constituent. The middle and upper troposphere make the largest contributions to
 496 the simulated TrC-O₃ trend globally, with large contributions from the upper troposphere driving
 497 the simulated TrC-O₃ trend at 30°S-30°N (Figure 11). The middle and upper troposphere

498 contribute most of the simulated positive TrC-O₃ trend over the eastern USA, while all three
499 levels contribute over western Europe and East Asia. The upper troposphere makes the primary
500 contribution to the simulated trend over Australia. Simulated TrC-O₃ trends are also quite
501 comparable to those observed by OMI/MLS within the measurement model uncertainty (see
502 Figure 10 and Figure 7). Over Australia, the OMI/MLS trend of 1.05 ± 1.44 DU/decade is higher
503 than the model trend of about 0.18 ± 0.308 DU/decade (see Figure 11). However, since OMI/MLS
504 trend has a calculated uncertainty (2σ) of 1.44 DU/decade, both the model and OMI/MLS for
505 Australia are not statistically different.

506 While the upper troposphere is a major driver of the simulated TrC-O₃ trends, the lower
507 troposphere is the largest contributor to the simulated trends in the tropospheric NO₂, CO, and
508 HCHO globally and over many regions (Figure 11). Exceptions include the simulated NO₂ in the
509 tropics (30°S-30°N), which is dominated by the upper troposphere, the simulated HCHO column
510 over the eastern USA, which is driven by the middle and upper troposphere; an important role
511 for upper tropospheric CO over East Asia; and the CO trend over Australia driven by the middle
512 tropospheric contribution. Figure 11 also shows that in some regions, such as the eastern USA
513 for all 3 precursors, the upper and lower tropospheric trends counteract each other, reducing the
514 magnitude of the column trend. In the following sections, we investigate trends and variability in
515 O₃ precursors, NO₂, CO, and HCHO.

516 3.4.4. NO₂ Trends

517 The TrC-NO₂ trends over 2005-2019 are shown in Figure 12 with a regional summary in Figure
518 13. On a global scale, there is a strong spatial variability of the TrC-NO₂ trends. About a third of
519 the oceans show HC increase of TrC-NO₂ trends (at 95% confidence level), especially at mid-
520 latitude, with trends up to $+0.01$ Pmolec/cm²/yr while only a few cells in the equatorial Pacific
521 show an HC decrease.
522



523
524 Figure 12: Global trends of OMI NO₂ tropospheric column (TrC-NO₂) over 2005-2019 (see text
525 for details on the calculation of the trends). Grey areas correspond to areas without enough data,
526 white areas correspond to regions where the trends remain at low confidence (at a 95%
527 confidence level).

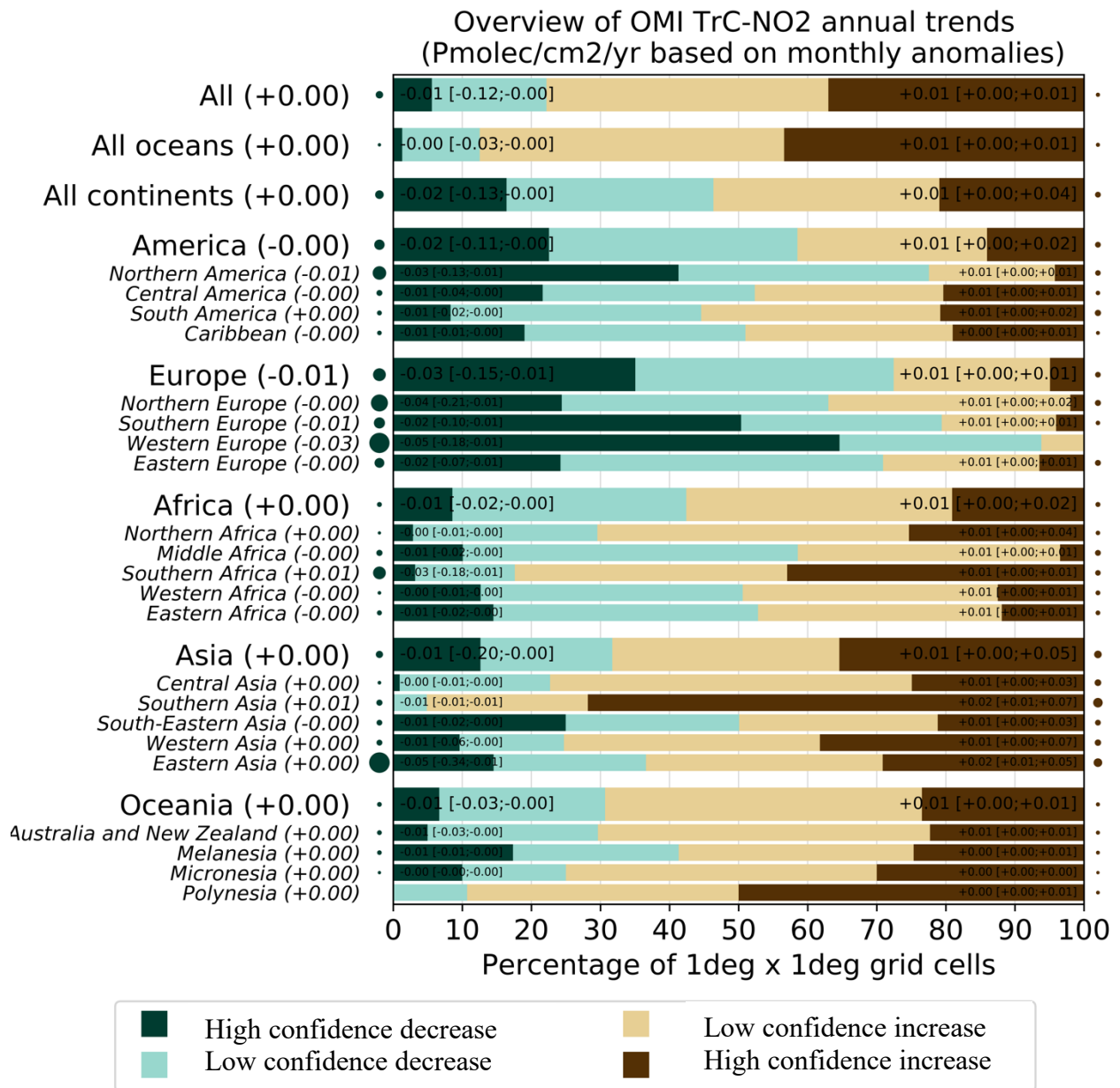
528 Regional trends are shown in Figure 13. For high-confidence trends in a given region, the
529 numbers correspond to the percentiles 5/50/95 of trends among the different cells of the region

530 where trends are considered high-confidence. Each region is tagged with a circle whose size is
531 proportional to the p50 of the high-confidence trends (red for positive and green for negative),
532 which allows us to quickly see regions where the trend is strong. For instance, for Eastern Asia
533 (this region includes 1442 1°x1° grid cells) about 15% of the grid cells (about 216 grid cells) in
534 this region show a high-confidence decrease in TrC-NO₂. Over these specific 216 cells with a
535 high-confidence decrease of TrC-NO₂, the 5th and 95th percentile of the trend is -0.34 and -0.01,
536 respectively, Pmolec/cm²/yr. About 28% of the grid cells in this region show a high-confidence
537 increase of TrC-NO₂ (which means about 403 grid cells). Over these specific 403 cells with a
538 high-confidence increase of TrC-NO₂, the 5th (resp 95th) percentile of the trend is +0.01 (resp
539 0.05) Pmolec/cm²/yr. Therefore, the Eastern Asia region shows sub-regions with high-
540 confidence decreasing TrC-NO₂, others with high-confidence increasing TrC-NO₂, and the rest
541 with low-confidence (positive and negative) trends. This figure allows us to quickly understand
542 the distribution of the trends within a given region while the overall regional trend is given by
543 the 50th percentile and the circles tagging each region. It's a regional summary of what is shown
544 in the trend global map. In Eastern Asia, the area where trends are with high-confidence positive
545 is more extended than for the high-confidence decrease (28% versus 15%), but the trend values
546 tend to be smaller (at least when comparing the 50th percentiles, -0.05 versus +0.01
547 Pmolec/cm²/yr). The map of regions is included in the supplement. Canada is included in
548 northern America but as shown in the trend map, most of Canada does not have OMI data

549 Over continental areas, high-confidence positive and negative trends are found in about
550 15-20% of the grid cells each (Figure 12). Regions with predominantly decreasing TrC-NO₂
551 include western and southern Europe (where about 50-60% of cells with a high-confidence
552 decrease), northern America (40% of cells with a high-confidence decrease, mostly located in the
553 eastern United States), Japan, and Indonesia. In absolute terms, these negative trends reach
554 values of about -0.03 Pmolec/cm²/yr. Specific eastern regions of China also show similar high-
555 confidence TrC-NO₂ decreases but overall, a larger part of the country faces increasing trends up
556 to +0.03 Pmolec/cm²/yr. Similar positive trends are observed over most of India, as well as in
557 specific parts of south-eastern Asia (mainly Vietnam) and the Middle East (mainly Iran and
558 Iraq). Conversely, TrC-NO₂ trends in Africa and South America remain mainly low-confidence ,
559 except in a few specific regions with high-confidence increases (e.g. South Africa, Morocco,
560 Chile, and parts of Brazil).

561 The trends in NO₂ have varying effects on the tropospheric ozone column, which is
562 related to the different local chemistry in each region. The concomitant decrease in TrC-O₃ and
563 TrC-NO₂ trends over some parts of the eastern US, and western Europe is consistent with the
564 strict NO_x control measures that were applied over the last two decades. STE can also contribute
565 to increased TrC-O₃ trends, especially in the mid-latitudes. A decreasing trend of TrC-NO₂ but
566 an increasing trend of TrC-O₃ is present in some other regions such as in the central US, which
567 might be due to local chemistry and STE.

568
569

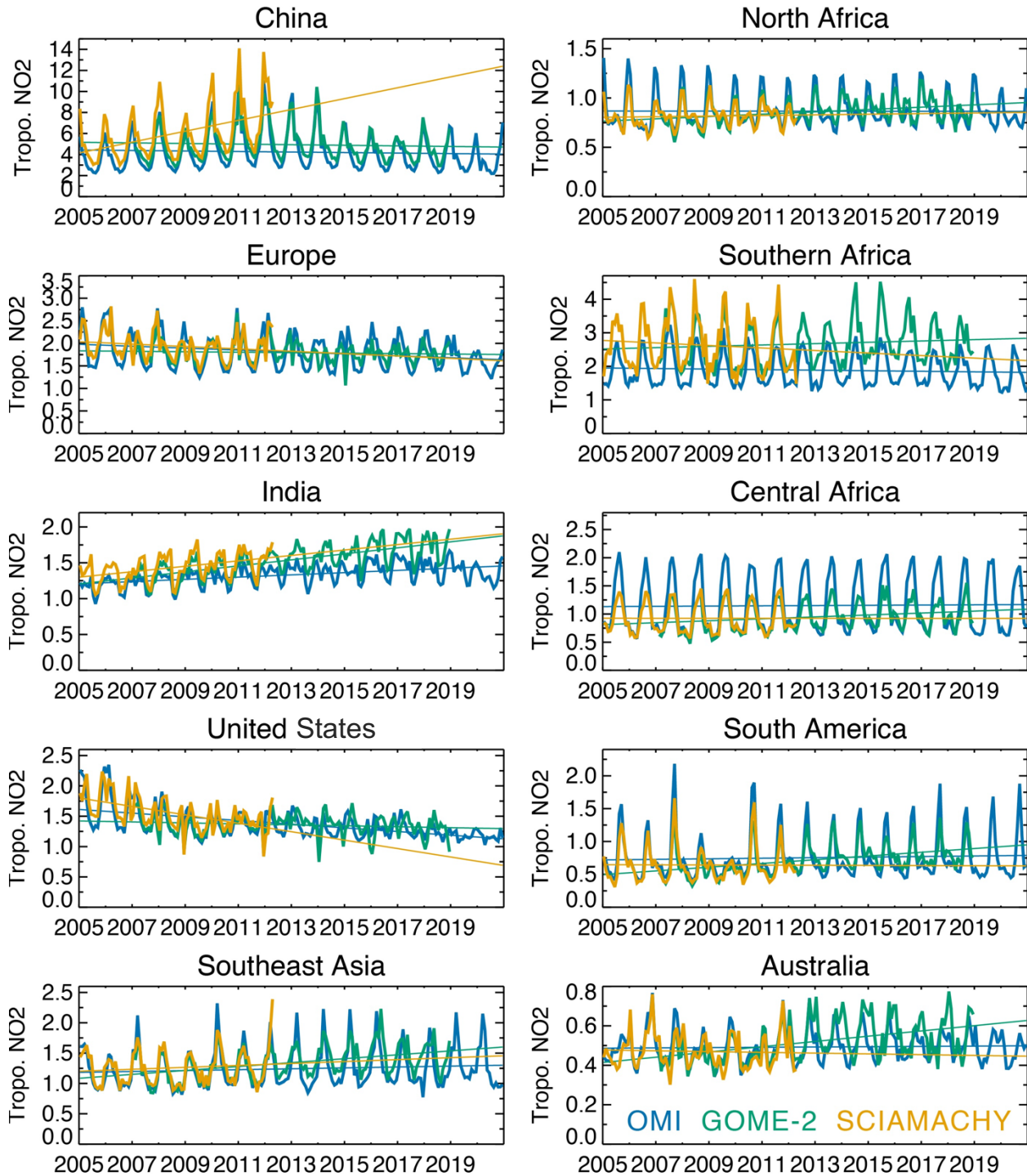


570

571 Figure 13: Summary of the high-and low-confidence regional trends of OMI NO₂ tropospheric
 572 column (TrC-NO₂) trends over 2005-2019, at a 95% confidence level (see text for details on the
 573 calculation of the trends). For each region, the trend on the bars is in the format: p50 [p5; p95],
 574 which represents the 50th[5th, and 95th] percentiles of the trends.

575 Figure 14 shows the time series of regional mean tropospheric NO₂ concentrations from three
 576 satellite instruments, OMI for 2005-2020, GOME-2 for 2007-2018, and SCIAMACHY for 2005-
 577 2012. All the instruments exhibit common large seasonal and year-to-year variations over both
 578 industrial regions and biomass-burning areas. Slight systematic differences among the instruments
 579 can mainly be attributed to the different overpass times. The satellite observations show positive
 580 trends over China by 2010, followed by a continued decrease. Over the USA and Europe, all the
 581 retrievals show a downward trend over the analysis period. Over the US, the observed TrC-NO₂
 582 levels decreased rapidly during 2005–2009 and subsequently show weaker reductions, as
 583 discussed by Jiang et al. (2018). A similar slowdown trend is found in Europe. Over India, the

584 OMI observations show positive trends over the 14 years ($+1.6\% \text{ yr}^{-1}$). The seasonal and year-to-
 585 year variations over Southeast Asia and northern and central Africa are associated with changes in
 586 biomass-burning activity (Ghude et al., 2009).
 587



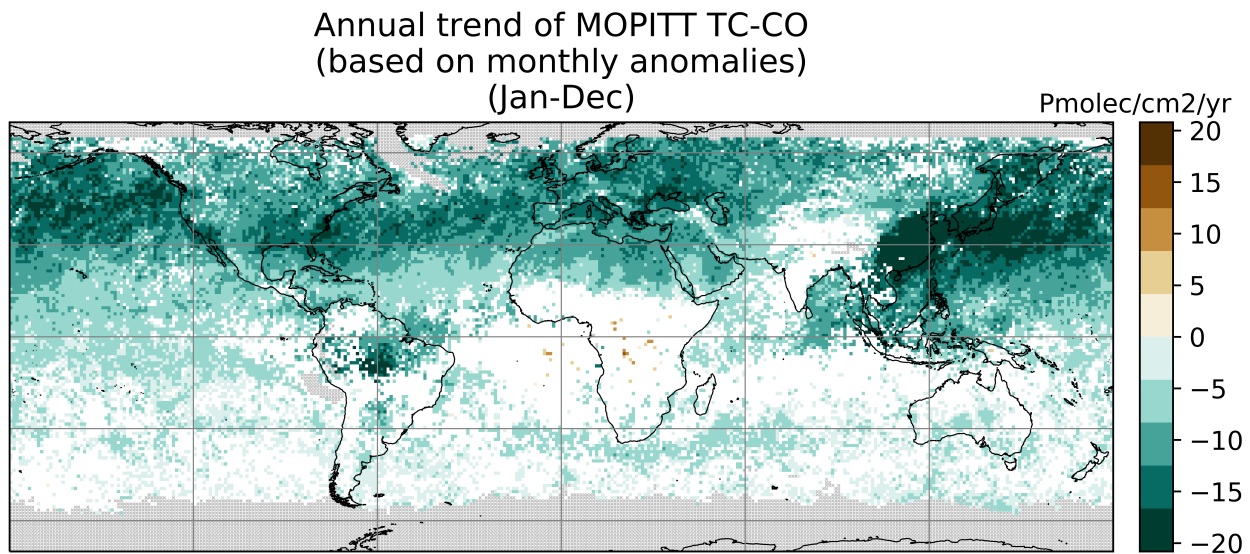
588
 589 Figure 14: Time series of regional monthly mean tropospheric NO₂ columns (in 10¹⁵ molecules
 590 cm⁻²) averaged over China (110–123° E, 30–40° N), Europe (10° W–30° E, 35–60° N), the US
 591 (70–125° W, 28–50° N), India (68–89° E, 8–33° N), South America (50–70° W, 20° S–Equator),
 592 northern Africa (20° W–40° E, Equator–20° N), central Africa (10–40° E, Equator–20° S),

593 southern Africa (25–34° E, 22–31° S), southeastern Asia (96–105° E, 10–20° N), and Australia
594 (113–155° E, 11–44° S) obtained from OMI (black), GOME-2 (blue), and SCIAMACHY (red).

595 3.4.5. CO Trends

596 CO trends are calculated based on MOPITT v9 products, see sec. 2.2.1. Observed CO trends
597 below show a slowing in the trend compared to a previous analysis (Buchholz et al. (2021)). In
598 the northern hemisphere, CO trends are largely negative over the US and Europe, which is
599 consistent with improvements in combustion efficiency and policies implemented to reduce air
600 pollution since 2004. Except for small sporadic positive trends, no HC trends can be calculated
601 over Central Asia (India and China), while there is a strong negative trend in East China due to
602 the recent strong focus on air quality improvement, and no HC trend in the SH.

603



604

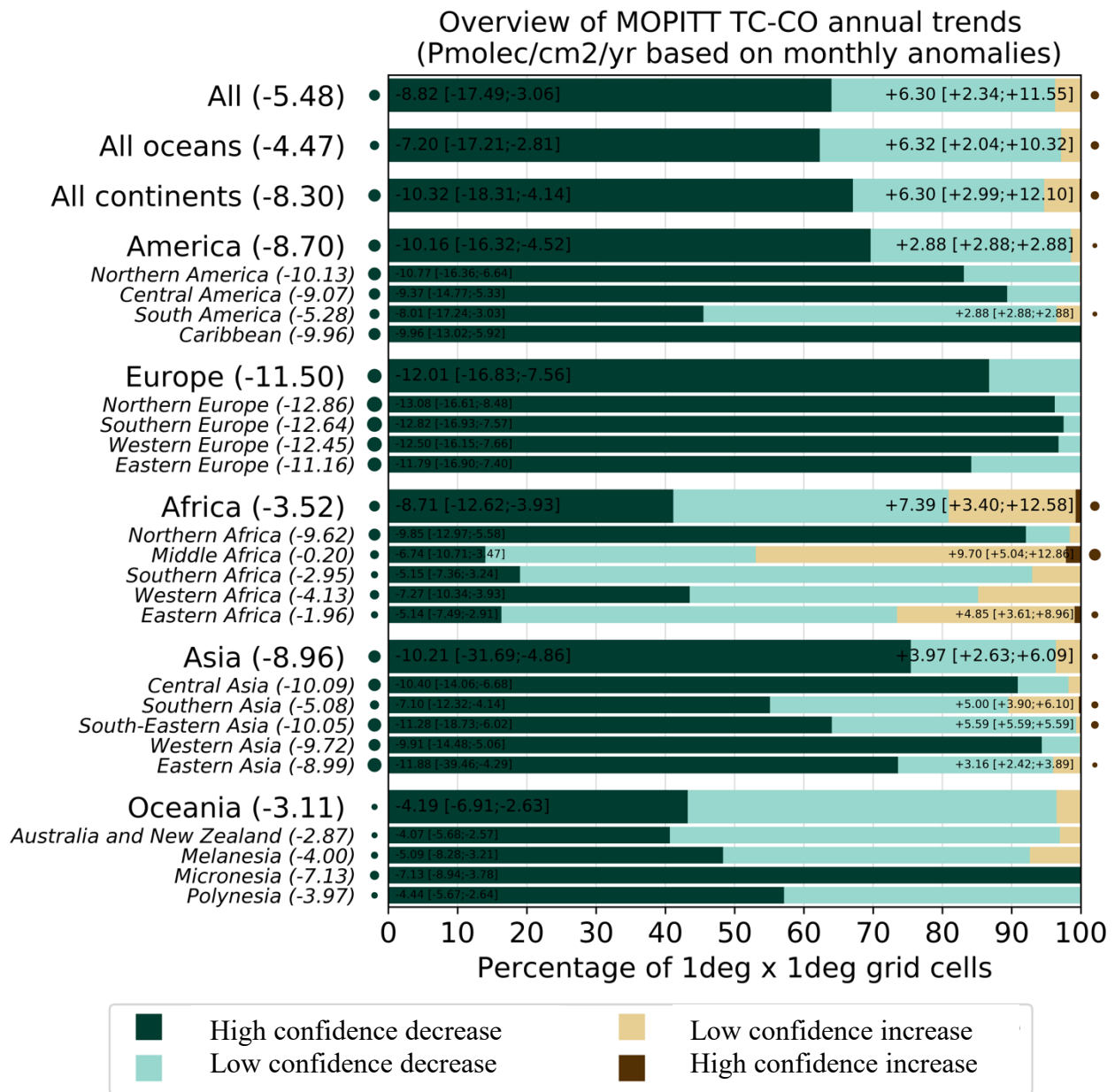
605 Figure 15: Trends in TC-CO from MOPITT V9J data, 2005-2019 (see text for details on the
606 calculation of the trends). Grey areas correspond to areas without enough data, white areas
607 correspond to regions where the trends remain statistically low-confidence at a 95% confidence
608 level.

609

610 A regional summary of the trends in the global map is shown in Figure 16. CO trends are
611 predominantly negative everywhere except for some sporadic positive trends over middle Africa.
612 Decreasing TC-CO trends are highest in Europe, followed by Asia and America with about 86%,
613 75%, and 69% of their cells being negative, respectively. The 50 percentiles of the trends in
614 these cells are -12.01, -10.21, and -10.16 Pmolec/cm²/yr, respectively. Africa shows the lowest
615 decreasing trends as the negative trends in North Africa are being offset by small increasing
616 trends in middle Africa. Overall, about 41% of the cells in Africa show decreasing trends, and
617 50% of the trends in these cells account for -8.71 Pmolec/cm²/yr. Thus, even though the NH
618 accounts for most of CO emissions, decreasing trends of TC-CO are evident in these regions.

619

620



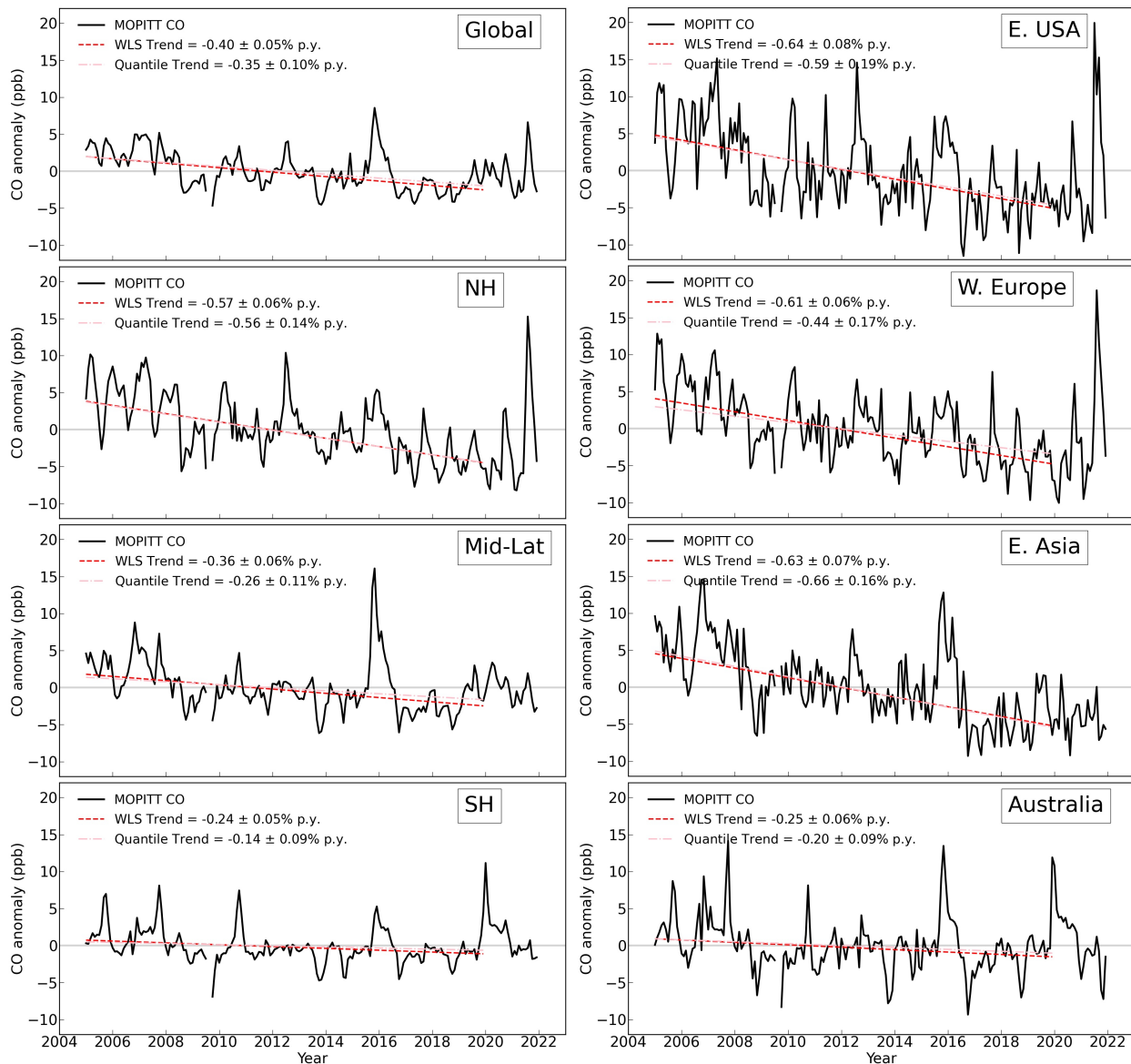
621

622 Figure 16: Summary of the statistically high- and low-confidence regional trends of MOPITT
 623 TC-CO trends over 2005-2019, at a 95% confidence level (see text for details on the calculation
 624 of the trends). For each region, the trends reported on the left (resp. right) represent the 50th[5th,
 625 and 95th] percentiles of the trends calculated over the different grid cells showing a high-
 626 confidence TC-CO increase or decrease.

627

628 Shown below are also the trends in the MOPITT column average volume mixing ratio (VMR)
 629 anomalies from 2005 to 2019 (Figure 17) using QR as well as Weighted least squares (WLS)) as
 630 Buchholz et al. (2021). The region boundaries are the same as used in Fig. 10 and 11. Results
 631 show a HC decreasing trend in the NH (-0.35 ± 0.1% annually), a smaller decreasing trend in the
 632 Mid-latitudes (-0.26 ± 0.1% annually), and LC trend in the SH (-0.14 ± 0.1% annually). The three
 633 anthropogenic regions investigated in the NH all show strong decreases in CO. The larger
 634 negative trend over Australia (-0.2 ± 0.1% annually) than the average SH, suggests sources from

635 the other two land regions (Southern Africa and South America) may be counteracting negative
 636 trends in CO for the SH.
 637



638
 639 Figure 17: MOPITT monthly average CO anomalies in column average volume mixing ratio
 640 (VMR, ppb), 2005-2021 (black). Updated dataset based on Buchholz et al. (2021). Data is Level
 641 3, monthly average daytime observations, using version 9 joint NIR/TIR retrievals (V9J).
 642 Regions are defined in Figure 10 and Figure 11. Trends are calculated on anomalies 2005-2019.
 643 The weighted Least Squares trend (red) is weighted by the monthly regional standard deviation.
 644 The quantile regression trend is also shown (pink). Grey dashed lines indicate a zero trend.

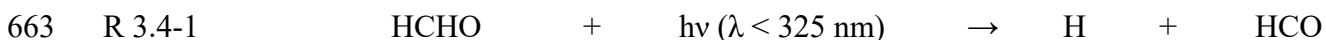
645
 646 We also compare CO trends with Community Earth System Model (CESM) simulations
 647 (Supplement Fig S1). While the magnitude of modeled CO tends to be underestimated relative to
 648 observations, the anomalies between the model and measurements are comparable, indicating the
 649 model reproduces interannual variability well. The negative trends in the NH are also reproduced

650 by CESM, although to a smaller degree than observations, suggesting that the trends in sources
 651 or loss processes (such as OH oxidation) are underestimated in the model. These processes will
 652 impact the feedback into modeled ozone and the resulting interpretation of driving factors for
 653 ozone abundance and variability. Interestingly, CESM correctly represents a negative trend in
 654 CO for the NH and East Asia while GEOS-GMI has a positive CO trend in those regions (Fig.
 655 11), likely due to the well-known misrepresentation of East Asia air quality improvements in
 656 emission inventories (Yin et al, 2015; Strode et al., 2016; Zheng et al, 2019). In the SH, CESM
 657 does not predict HC trends.

658

659 **3.4.6. HCHO Trends**

660 HCHO, mainly a photochemical product results from hydrocarbon oxidation. HCHO is itself a
 661 source of OH and ozone through its photolysis producing HO₂, which can be recycled back to
 662 OH if sufficient NO levels are present.



667 Unlike higher aldehydes, the OH reaction with HCHO leads also to the formation of a formyl
 668 radical (HCO), which ultimately forms HO₂ (R 3.4-3).

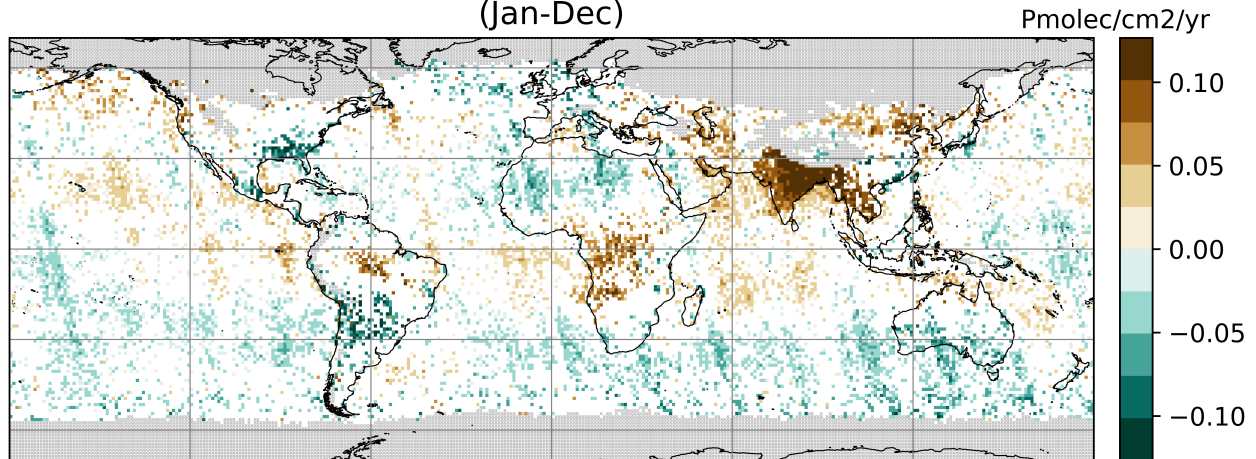


670 Due to its solubility, the variability of HCHO also depends on the presence of clouds, and wet
 671 deposition ultimately represents another important sink for HCHO (Lelievre and Crutzen, 1991).
 672 Overall, HCHO plays a key role in the O₃ budget, both in polluted and remote regions.

673 Trends of the OMI HCHO tropospheric columns (hereafter referred to as TrC-HCHO) are
 674 computed as described for OMI TrC-NO₂. TrC-HCHO trends over 2005-2019 are shown in
 675 Figure 18 with a regional summary in Figure 19. The first global feature to highlight on the
 676 global trends map is the presence of stripes along the OMI orbits. The number of rows affected
 677 by the OMI row anomaly has increased over the years (Boersma et al., 2018). The affected rows
 678 are filtered out in the HCHO data, but the change in the sampling and the related increase in the
 679 noise impact the trend analysis. Along orbit stripes in the trend analysis should be ignored but
 680 zonal trends are still valid (Figure 18).

681

Annual trend of OMI TrC-HCHO
(based on monthly anomalies)
(Jan-Dec)



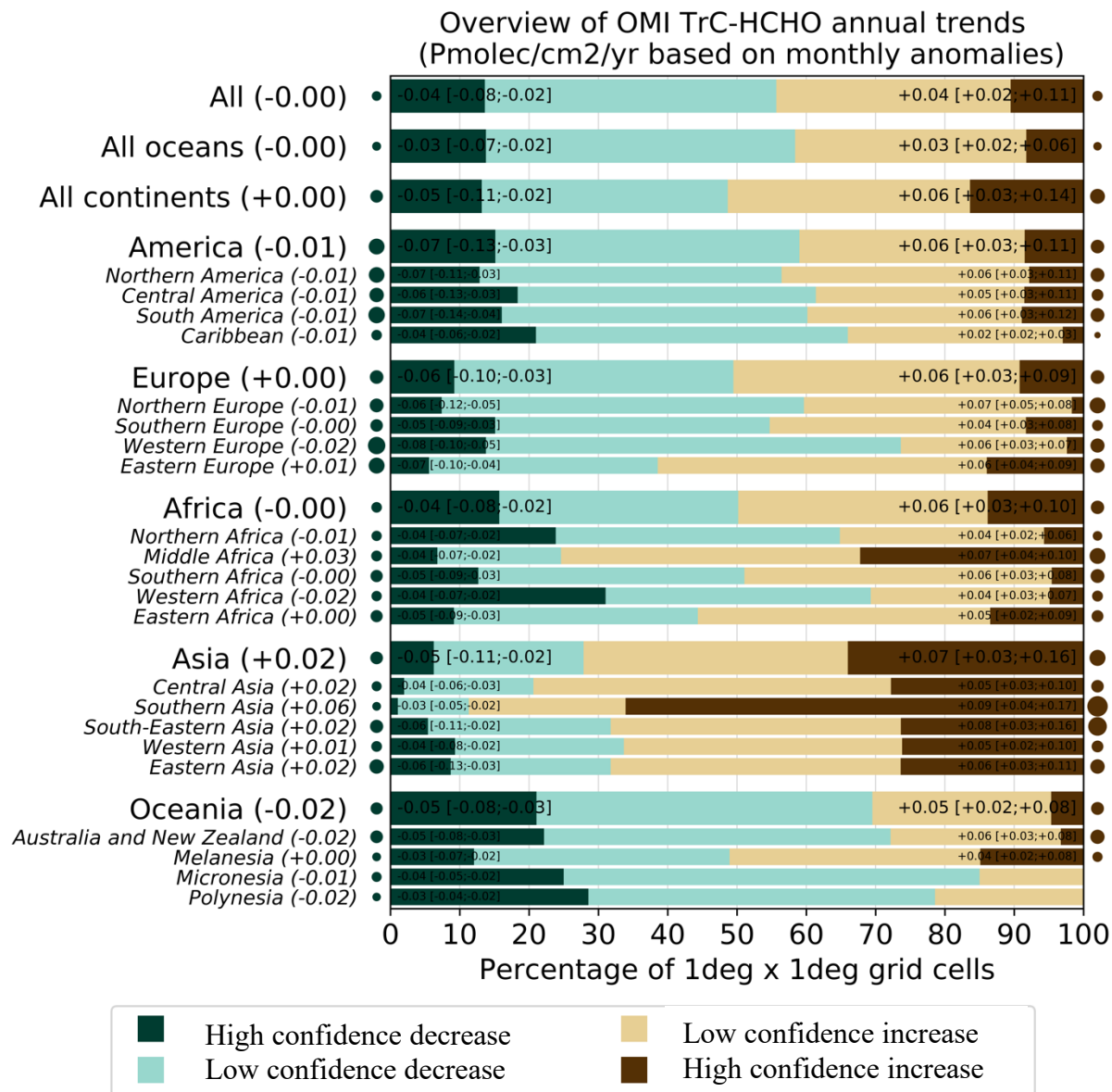
682

683 Figure 18: Global trends of OMI HCHO tropospheric column (TrC-HCHO) over 2005-2019 (see
684 text for details on the calculation of the trends). Grey areas correspond to areas without enough
685 data, white areas correspond to regions where the trends remain statistically low-confidence at a
686 95% confidence level.

687 Despite the fact that TrC-HCHO trends remain LC over a large part of the globe, specific regions
688 do highlight clear trends. The region with clearest changes is unambiguously southern Asia
689 where about 65% of the cells show increasing trends with a median of +0.09 Pmolec/cm²/yr. The
690 other regions with a large portion (25-30% of the cells) of increasing trends include the rest of
691 Asia and central Africa, with median TrC-HCHO trends ranging between +0.05 and +0.08
692 Pmolec/cm²/yr, as well as some parts of central Brazil (Amazonians). Conversely, some HC
693 decreases of TrC-HCHO are observed in the south-eastern US, the southern half of Southern
694 America, North and western Africa, and southern Australia, although part of them overlap with
695 the aforementioned stripes and might thus not be real.

696

697



698

699 Figure 19: Summary of the statistically high- and low-confidence regional trends of OMI HCHO
700 tropospheric column (TrC-HCHO) trends over 2005-2019, at a 95% confidence level (see text
701 for details on the calculation of the trends). For each region, the trends reported on the left (resp.
702 right) represent the 50th[5th, and 95th] percentiles of the trends calculated over the different grid
703 cells showing a HC TrC-HCHO increase or decrease.

704

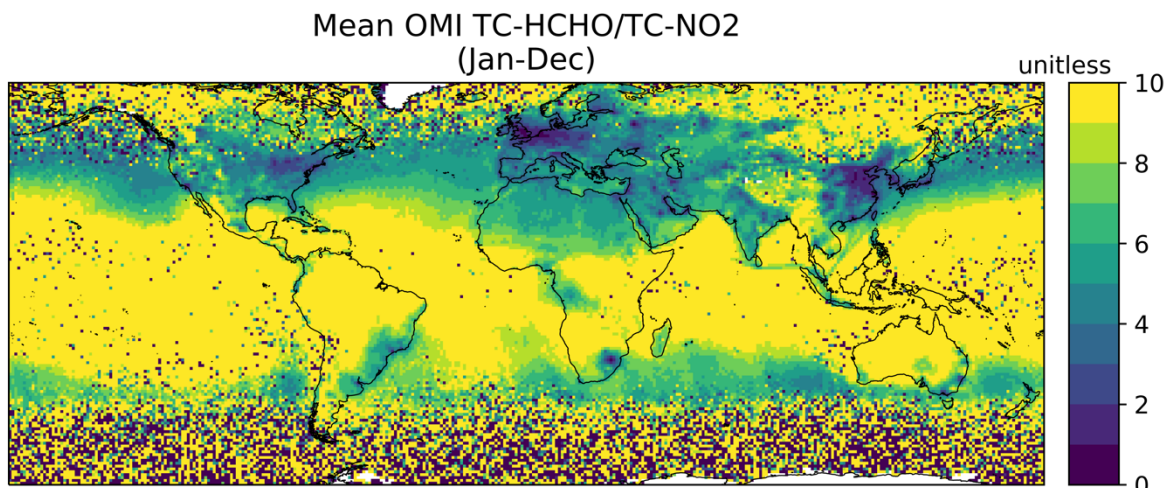
705 HCHO trends varies with that of O₃ (sec. 3.4.1) which might be due to several factors, such as
706 their different sensitivity to NO_x and hydrocarbons (Luecken et al., 2018) but also possible STE
707 contribution to tropospheric ozone levels, especially in midlatitudes (Willimas et al., 2019; Li et
708 al., 2024). For example, while TrC-O₃ is increasing in the southeastern US, TrC-NO₂, TC-CO,
709 and TrC-HCHO are decreasing, which, in addition to the local chemistry, might indicate a STE
710 signal. TrC-NO₂ trends are decreasing over the northern coast of Australia while those of TrC-O₃
711 and TrC-HCHO are increasing. While the increase of HCHO/NO₂ might indicate a trend toward
712 NO-limited conditions (see below), the increase of TrC-O₃ trends in this region might also
713 indicate increasing trends of STE contribution (Li et al., 2024). However, TrC-HCHO trends are

714 consistent with that of TrC-O₃ in other regions, e.g., over the northeastern US and Europe.
715 Similarly, while NO₂ trends are slightly increasing over central and southern Australia, trends of
716 TrC-O₃ and TrC-HCHO are decreasing, which indicates a trend toward VOC-limited conditions
717 (see below).

718

719 3.4.7. HCHO/NO₂

720 The ratio of TrC-HCHO/TrC-NO₂ observed from space (e.g., Martin et al., 2004) has been used
721 in a number of studies to give insights on the O₃ chemical regime, higher (resp. lower) TrC-
722 HCHO/TrC-NO₂ ratios indicate NO_x-limited (resp. RO_x-limited) regimes. Although imperfect
723 (e.g. Sourì et al., 2023), this indicator yet provides some qualitative information on the evolution
724 of the O₃ regime over the last years (Nussbaumer et al., 2023). We note that this analysis does not
725 consider variations in the ratios and their trends with respect to season or altitude. The mean TrC-
726 HCHO/TrC-NO₂ over 2005-2019 are shown in Figure 20, and the trend results are in Figure 21
727 with a regional summary in Figure 22. The highest ratios are observed in the tropical regions due
728 to strong TrC-HCHO from biogenic sources and fire NMVOC emissions in tropical South America
729 and Africa combined with relatively low TrC-NO₂. Conversely, lower TrC-HCHO/TrC-NO₂ ratios
730 are observed across western Europe and north-eastern Asia, and to a lesser extent, the northeastern
731 US.
732

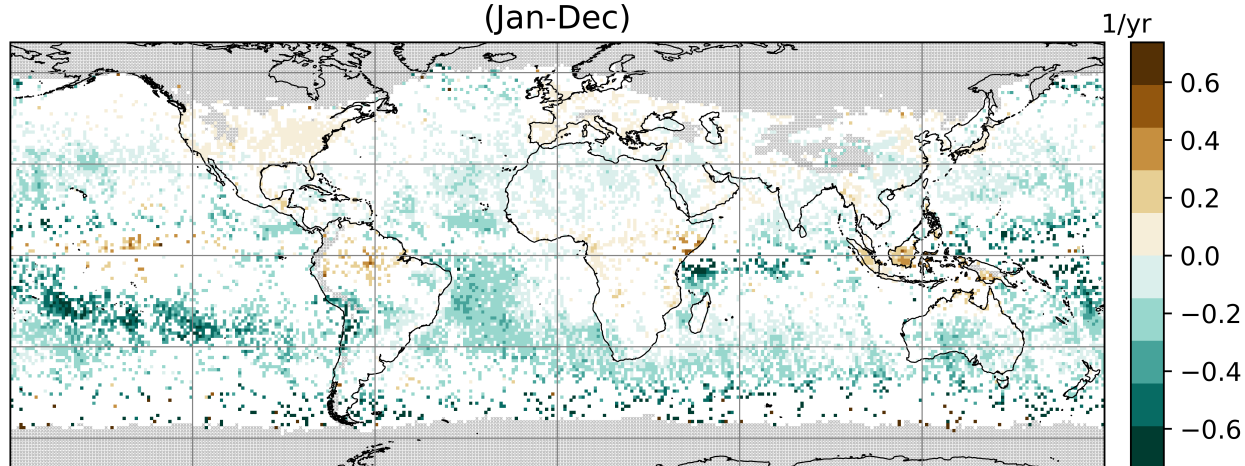


733
734 Figure 20: Global mean OMI HCHO/NO₂ tropospheric column ratio over 2005-2019.
735

736 At a global scale, the HC changes in TrC-HCHO/TrC-NO₂ trends (Figure 21-Figure 22) mostly
737 go in the direction of a reduction, with about 25% of the grid cells showing a median trend of -
738 0.52 yr⁻¹. (while only 5% of the cells show an HC increase of +0.03 yr⁻¹) as shown in Figure 22.
739 This suggests that these areas are evolving toward VOC-sensitive conditions (which does not
740 necessarily imply that they are already in this regime). This situation is observed over a large part
741 of Oceania (especially Polynesia) and specific parts of Africa, Asia, and South America. The
742 opposite HC trends, toward more NO-sensitive conditions, are mainly observed over Europe and
743 northern America, as well as South Asia. We note that the mean TrC-HCHO/TrC-NO₂ indicates
744 the mean status of the chemical regime over this period of time (2005-2019). However, the trends
745 of the TrC-HCHO/TrC-NO₂ ratio show the changing sensitivity of the chemical regime over this

746 period of time. For example, while the ratio in the Eastern US indicates VOC-sensitive conditions,
747 the trends of TrC-HCHO/TrC-NO₂ indicate a direction toward NO-sensitive conditions.
748

Annual trend of OMI TrC-HCHO/NO₂
(based on monthly anomalies)
(Jan-Dec)

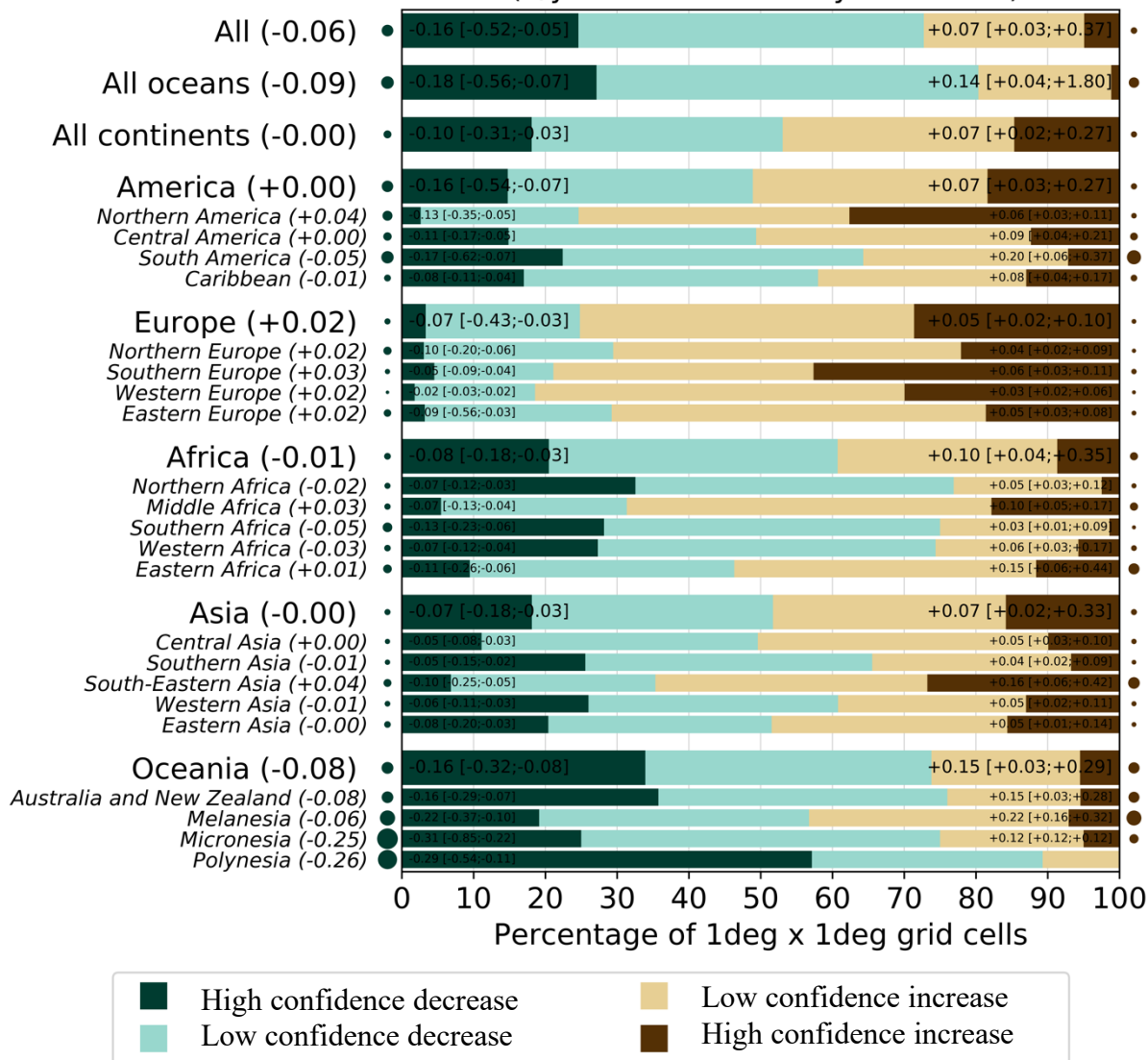


749
750 Figure 21: Global trends of OMI HCHO/NO₂ tropospheric column ratio over 2005-2019 (see
751 text for details on the calculation of the trends). Grey areas correspond to areas without enough
752 data, white areas correspond to regions where the trends remain statistically low-confidence at a
753 95% confidence level.

754
755 The trends on the TrC-HCHO/TrC-NO₂ ratio is mainly driven by specific trends on TrC-HCHO
756 and/or TrC-NO₂, depending on the region. The ratio increase in southern and western Europe and
757 southeast Asia appears primarily due to decreasing TrC-NO₂, since TrC-HCHO does not change
758 with HC. Over North America, observed TrC-HCHO values decrease but less than TrC-NO₂,
759 which thus drives the ratio toward an increase. Conversely, the increase of TrC-HCHO/TrC-NO₂
760 in equatorial Africa and Amazonians appears mainly driven by increasing TrC-HCHO. The
761 regions with HC decreasing TrC-HCHO/TrC-NO₂ ratio include Chile and Australia, due to both
762 decreasing TrC-HCHO and increasing TrC-NO₂ (Figure 22), indicating a trend towards a VOC-
763 limited regime. Note that over the US, Jin et al. (2020) demonstrated the reasonable ability of the
764 OMI-based TrC-HCHO/TrC-NO₂ trends to capture the transition from RO_x-limited to NO_x-limited
765 regimes over main US cities and found a relatively good consistency between observed changes
766 of the surface O₃ and space-based HCHO/NO₂ increasing trends.

767
768
769

Overview of OMI TrC-HCHO/NO2 annual trends (1/yr based on monthly anomalies)



770
 771 Figure 22: Summary of the statistically high- and low-confidence regional trends of OMI TrC-
 772 HCHO/TrC-NO₂ tropospheric column ratio trends over 2005-2019, at a 95% confidence level (see
 773 text for details on the calculation of the trends). For each region, the trends reported on the left
 774 (resp. right) represent the 50th[5th, and 95th] percentiles of the trends calculated over the different
 775 grid cells showing a high confidence TrC-HCHO/TrC-NO₂ increase or decrease.

776
 777

779 3.5. Lightning NO_x and Its Effects on Tropospheric NO_x and O₃

780 Nitric oxide (NO) is produced in lightning flash channels and quickly comes into equilibrium with
781 NO₂. Cloud-scale simulations of thunderstorms indicate that 55-75% of lightning NO_x (LNO_x) is
782 detrained above 8 km (Pickering et al., 1998) where it enhances upper tropospheric NO_y, OH, and
783 O₃ (Labrador et al., 2005; Allen et al., 2010; Liaskos et al., 2015) and contributes to enhanced
784 longwave radiative absorption by O₃ (Lacis et al., 1990; Finney et al., 2018). Enhanced OH leads
785 to a decrease in CH₄ lifetime and decreased longwave radiative absorption (Fiore et al., 2006;
786 Finney et al., 2018). The lifetime of NO_x in the upper troposphere is controlled by the chemical
787 cycling of NO_x with reservoir species and is 10-20 days away from deep convection (Prather and
788 Jacob, 1997) but only 2-12 hours in the vicinity of convection (Nault et al., 2016, 2017). This
789 chemical recycling provides a source of NO_x downwind of thunderstorms, which causes the ozone
790 production efficiency of emitted NO_x to be 4-20 times higher in the upper troposphere than at the
791 surface. Thus, LNO_x has a disproportionate impact on the tropospheric O₃ budget (Pickering et al.,
792 1990; Grewe et al., 2001; Sauvage et al., 2007).

793 The distribution of lightning is fairly well known over much of the Earth due to remote
794 sensing observations and an increase in the number and capability of ground-based lightning
795 networks. However, the LNO_x production efficiency (PE, mol fl⁻¹) is a continued source of
796 uncertainty. Schumann and Huntrieser (2007) reviewed the literature on LNO_x production, finding
797 a best estimate of 250 moles per flash, with uncertainty factors ranging from 0.13 to 2.7. The PE
798 can be estimated from theoretical and laboratory considerations (Price et al., 1997; Koshak et al.,
799 2014), using thunderstorm anvil observations by aircraft (Ridley et al., 2004; Huntrieser et al.,
800 2008, 2011; Pollack et al., 2016; Nault et al., 2017; Allen et al., 2021a), based on satellite data
801 (Bucsela et al., 2010; Beirle et al., 2010; Pickering et al., 2016; Bucsela et al., 2019; Lapierre et
802 al., 2020; Zhang et al., 2020; Allen et al., 2019, 2021b), or using cloud-resolved (e.g., DeCaria et
803 al., 2000; 2005; Fehr et al., 2004; Ott et al., 2007, 2010; Cummings et al., 2013; Pickering et al.,
804 2023) or global model simulations with chemistry (e.g. Martin, et al., 2007; Murray et al., 2012;
805 Miyazaki et al., 2014; Marais et al., 2018). These various techniques have yielded PE estimates
806 ranging from <50 to >1000 mol fl⁻¹, with most estimates in the 100-400 mol fl⁻¹ range. Miyazaki
807 et al. (2014) assimilated OMI NO₂, MLS and TES O₃, and MOPITT CO into a chemical transport
808 model to provide comprehensive constraints on the global LNO_x source, resulting in an estimate
809 of mean PE of 310 moles per flash. Marais et al. (2018) used cloud-sliced upper tropospheric NO₂
810 from OMI together with the GEOS-Chem model to estimate a mean LNO_x PE of 280 moles per
811 flash. Lightning is the dominant source of NO_x in the tropical upper troposphere year-round and
812 in the northern mid-latitudes in summer. Lightning is responsible for 10-15% of NO_x emissions
813 globally. Assuming 100-400 mol fl⁻¹, the global LNO_x production is likely 2 – 8 Tg N a⁻¹
814 (Schumann and Huntrieser, 2007; Verma et al., 2021). LNO_x impacts air quality and deposition
815 (Kaynak et al., 2008; Allen et al., 2012). On average LNO_x adds 1-2 ppbv to surface O₃ (Kang et
816 al., 2019b), although contributions as large as 18 ppbv have been seen for individual events
817 (Murray et al., 2016). Allen et al. found that the addition of LNO_x to the Community Multiscale
818 Air Quality (CMAQ) model increased wet deposition of oxidized nitrogen at National
819 Atmospheric Deposition Program (NADP) sites by 43%, reducing low biases from 33% to near-
820 zero. Kang et al. (2019b) found similar improvements for wet deposition and also found that
821 including LNO_x resulted in smaller biases with respect to ozonesondes and aircraft profiles taken
822 during the NASA DISCOVER-AQ field campaign (Flynn et al., 2016). Thus, to accurately assess
823 its impacts on air quality, it is critical that LNO_x-producing deep convection is accurately
824 simulated.

825 Only in recent years with the advent of satellite observations of lightning flashes and improved
826 coverage by ground-based lightning networks has there been sufficient data to make estimates of
827 trends in the occurrence of lightning. However, it is unknown whether trends in LNO_x production
828 are similar to those of lightning itself. Lightning characteristics such as the ratio of intracloud (IC)
829 flashes to cloud-to-ground (CG) flashes, the multiplicity (i.e., the number of strokes per flash), and
830 the peak current or energy associated with flashes may vary over time. All of these lightning
831 characteristics may have effects on the magnitude of LNO_x production. We have insufficient data
832 to take into account these possible effects on LNO_x production over large spatial domains or over
833 sufficiently long periods of time.

834 **3.5.1. Global Historical Trends of Lightning**

835 The first attempts at an examination of trends in thunderstorm activity were conducted in terms of
836 thunder-days (in Japan by Kitagawa et al., 1989; in Brazil by Pinto et al., 2013). A more recent
837 global analysis was conducted by Lavigne et al. (2019), who analyzed trends in thunder-days
838 (number of days with audible thunder at weather observation stations) over 43 years and in flashes
839 recorded by the Lightning Imaging Sensor (LIS) on the Tropical Rainfall Measuring Mission
840 (TRMM) for 16 years. Thunder-days increased since the 1970s in the Amazon Basin, the Maritime
841 Continent, India, Congo, Central America, and Argentina. Decreases in thunder-days were found
842 in China, Australia, and the Sahel region of Africa. Lavigne et al. (2019) do not provide a global
843 trend in thunder days, but an average trend computed over the nine primary lightning regions that
844 they considered, weighted by the mean annual thunder days in each region, yields a near global
845 estimate of +3.8% per decade. How well do thunder-days represent lightning flash rate? Lavigne
846 et al. found a positive correlation between thunder-days and LIS flash rates in China, the Maritime
847 Continent, South Africa and Argentina, but disagreement on the trend in India and West Africa.

848 Large-scale ($\pm 38^\circ$ latitude) trends in lightning flashes have been examined in the data collected by
849 the LIS on the TRMM satellite (January 1998 – December 2014) and on the International Space
850 Station (February 2017 – December 2021). Füllekrug et al. (2022; see Figure SB2.1b) demonstrate
851 that the annual mean deviations from the 1998 – 2021 mean are no more than ~5% except for ~-
852 10% in 2020 and ~-8% in 2021. However, no long-term trend is evident from the LIS data. The
853 possibility that these larger negative deviations in 2020 and 2021 are due to Covid-19 lockdowns
854 and general declines in economic activity has been speculated. The link may be provided by
855 changes in Aerosol Optical Depth (AOD) as suggested by Liu et al. (2021) who demonstrated 10-
856 20% flash reductions in March – May 2020 relative to the 2018 – 2021 mean for those months
857 from the GLD360 and WWLLN ground-based lightning networks. Regional lightning reductions
858 were consistent with AOD reductions noted by Sanap (2021). Larger reductions in lightning were
859 noted over Africa/Europe and Asia/Maritime Continent and lesser reductions over the Americas.

860 **3.5.2. Regional Historical Trends of Lightning**

861 Widely varying trends in lightning over China have been reported in the literature. To some extent,
862 whether the trend in lightning is upward or downward depends on the particular region studied and
863 on the period of time considered. Yang and Li (2014) were the first to report on lightning trends
864 in China. They used lightning data from the TRMM/LIS sensor and human-observed thunderstorm
865 day occurrence over the period 1990 to 2012 in southeastern China. Thunderstorms and lightning
866 occurrence increased over the period as well as LIS precipitation radar echo tops heights. These
867 increases were accompanied by decreases in visibility, indicating increases in pollution aerosol.
868 Detailed work on lightning trends in China has been performed in relation to aerosols. Shi et al.
869 (2020) correlated flashes from the TRMM/LIS Low-Resolution Monthly Time Series (2.5 deg.
870 resolution) with AOD from MODIS-Terra V6.1 Level 3 over the period 2001 to 2014. For AOD

871 < 1.0, $r = 0.64$, indicating a likely microphysical effect on lightning flash rate. For $AOD > 1.0$, $r =$
872 -0.06 , which could indicate that with higher aerosol concentration there is a radiation effect
873 stabilizing the atmosphere and/or a decrease in the number of graupel particles in the mixed-phase
874 region of the storms that is important for charging. Flashes were also correlated with surface
875 relative humidity and Convective Available Potential Energy (CAPE). As AOD generally
876 increased over much of the early portion of this time period and then decreased, lightning flash
877 rates followed similar trends. Wang et al. (2021) examined a 9-year record (2010- 2018) of CG
878 lightning from the China Lightning Detection Network in three polluted urban areas of China
879 (Chengdu, Wuhan, and Jinan). They found decreasing trends (see Wang et al., 2021) in CG
880 lightning and total AOD (from the MERRA-2 reanalysis). Annual mean lightning density in these
881 three regions decreased by 50 – 75% as annual mean AOD fell from 0.70 – 0.75 to 0.53 to 0.62.

882 Qie et al. (2022) analyzed the OTD/LIS record from 1996 through 2013, and found that lightning
883 increased over the eastern Tibetan Plateau by $0.072 \pm .069$ fl $\text{km}^2 \text{yr}^{-1}$. Over the 18 years, this
884 increase amounted to a total of 1.3 fl $\text{km}^2 \text{yr}^{-1}$, compared with a climatological value of 7.7 fl km^2
885 yr^{-1} , thereby indicating a HC increase. The ground-based World Wide Lightning Location Network
886 (WWLLN) also showed increased strokes in this region. The increase in lightning frequency in
887 this region was found to be due to an increase in thunderstorm frequency, not increased storm
888 intensity.

889 Koshak et al. (2015) analyzed National Lightning Detection Network (NLDN) CG flashes over
890 the contiguous United States (CONUS) from 2003 to 2012. The five-year mean flashes over 2008
891 to 2012 decreased by 12.8% from the five-year mean for 2003 to 2007 (Table 1). The CONUS
892 average wet bulb temperature also trended downward during this period, which may have led to
893 lesser or weaker storms. However, US Environmental Protection Agency air quality trends show
894 an 18% decrease in PM_{2.5} concentrations over CONUS between the two subperiods, which also
895 could have had an influence on the flash rates. A recent effort to update the Koshak et al. (2015)
896 analysis is underway. NLDN flashes have been reprocessed (Kenneth Cummins, personal
897 communication) from 2015 through 2021 to ensure that the classification of IC and CG flashes is
898 done consistently with data prior to 2015. Trend analysis of NLDN CG flashes from 2003 (a major
899 upgrade of the NLDN network hardware) through 2022 (William Koshak, personal
900 communication) shows a HC reduction in CG flashes over CONUS, comparing the mean CG
901 flashes over 2003-2004 with the mean over 2021 -2022. Within this period a major decrease
902 (~25%) in CONUS CG flashes occurred from 2011 to 2012. Flashes in 2013 remained low, but
903 recovered by 2014-2015. A major decrease (~27%) occurred from 2019 to 2020, with a small
904 increase in 2021. These results have been obtained from ongoing efforts by Dr. William Koshak
905 of the NASA Marshall Space Flight Center, and are presently part of a draft manuscript by lead
906 author Koshak that extends and refines the earlier work in Koshak et al. (2015). Details concerning
907 these trends will be contained in that manuscript.

908 A possible contributing factor to the CONUS decline in CG flashes over 2003 to 2021 is the
909 substantial decrease in aerosol. Surface annual average PM_{2.5} concentrations averaged over
910 CONUS decreased by 37% from 2000 to 2021 according to the EPA National Air Quality Trends
911 Report (<https://www.epa.gov/air-trends/air-quality-national-summary>). However, no decrease in
912 CONUS annual average PM_{2.5} was seen from 2019 to 2020. As mentioned previously, AOD may
913 be a better indicator of the aerosol amount that may become incorporated into thunderstorm clouds.
914 Sanap (2021) showed negative anomalies of AOD of ~0.1 in portions of CONUS in March and
915 April 2020 and 0.1 to 0.2 in May 2020. The major decrease in CONUS CG flashes from 2011 to
916 2012 has been related to drought conditions during Summer 2012 over the South Central and
917 Southeastern US (Koshak et al., 2015). The reason for the number of CONUS flashes remaining

918 lower in 2013 is uncertain. Koehler (2020) analyzed 26 years (1993 – 2018) of NLDN CG
919 lightning data to construct a thunder-day climatology for CONUS. Positive anomalies from the
920 26-year mean were found from Texas to Colorado during 2003 to 2007, and negative anomalies
921 in this region during 2008 to 2012. These anomalies were consistent with precipitation anomalies
922 associated with ENSO.

923
924 Holzworth et al. (2021) analyzed primarily CG lightning data from WWLLN for June, July, and
925 August for the years 2010 through 2020. The ratio of lightning strokes north of 65° N latitude to
926 the total global strokes increased by a factor of three over this period. This increase occurred as
927 the surface temperature anomaly in this region increased by 0.3°C (see Holzworth et al., 2021).
928 These results suggest a substantial increase in upper tropospheric NO_x and subsequent ozone
929 production at high northern latitudes.

930

931 **3.5.3. Future Lightning Trends**

932 Parameterizations in global chemistry and climate models have been developed for
933 lightning flash rate. These schemes typically use kinematic, thermodynamic or microphysical
934 variables from the model as predictors. In some studies such predictors have simply been applied
935 to output from multiple climate models. This is the case with the Romps et al. (2014) work, which
936 showed that when a lightning parameterization scheme using CAPE x Precipitation Rate is applied
937 to 11 climate models an increase in CG lightning by 12 +/- 5% per degree Celsius of climate
938 warming was computed. This work simply used the 12-hour resolution time series of spatial means
939 of these variables over CONUS as input. Changes in IC lightning flashes were not considered. IC
940 flashes typically outnumber CG flashes by a factor of 3 averaged over CONUS. Therefore, the
941 result of this work is unknown with respect to the amount of change in LNO_x emission. Romps et
942 al. (2018) updated their analysis using CAPE from 3-hourly North American Regional Reanalysis
943 (NARR) data and hourly precipitation from NOAA River Forecast Centers, finding that CAPE x
944 Precipitation Rate captures the spatial, seasonal, and diurnal variations of NLDN CG flash rate
945 over land, but does not predict the pronounced land-ocean contrast in flash rates. Therefore, these
946 analyses are of limited value in estimating trends of LNO_x over broader-scale regions. Romps et
947 al (2019) tested four lightning proxies in a cloud-resolved 4-km resolution simulation over
948 CONUS with the Weather Research and Forecasting (WRF) model, and over the tropical oceans
949 with a Radiative Convective Equilibrium model. The proxies were CAPE x Precipitation Rate,
950 precipitation with vertical velocity > 10 m/s, vertical ice flux at the 260K isotherm, and vertical
951 integral of cloud ice and graupel product. The fractional change in proxy values per 1 degree
952 Celsius of warming over CONUS was +8 to +16%. Over the tropical oceans the changes in proxy
953 values per degree ranged from +12% for CAPE x Precipitation Rate to -1% for ice flux and -3%
954 for the cloud ice and graupel product. Therefore, over broad regions of the Earth, there is great
955 uncertainty on future trends in lightning.

956 Finney et al. (2016; 2018) compared lightning projections for 2100 using vertical ice flux
957 (Finney et al., 2014) and cloud-top height parameterizations for flash rate in the UK Chemistry
958 and Aerosols Model. They obtained -15% global change in total flash rate with ice flux under a
959 strong global warming scenario (see Finney et al., 2018), which was composed of a greater
960 decrease in the tropics and small increases in mid-latitudes. In terms of LNO_x emissions this work
961 using the ice flux scheme produced -0.15 TgN K⁻¹ change over the years from 2000 to 2100,
962 implying less O₃ production. With the cloud-top height scheme they obtained +0.44 TgN K⁻¹ LNO_x
963 change, implying increased O₃ production. However, the ice flux scheme provided a more realistic

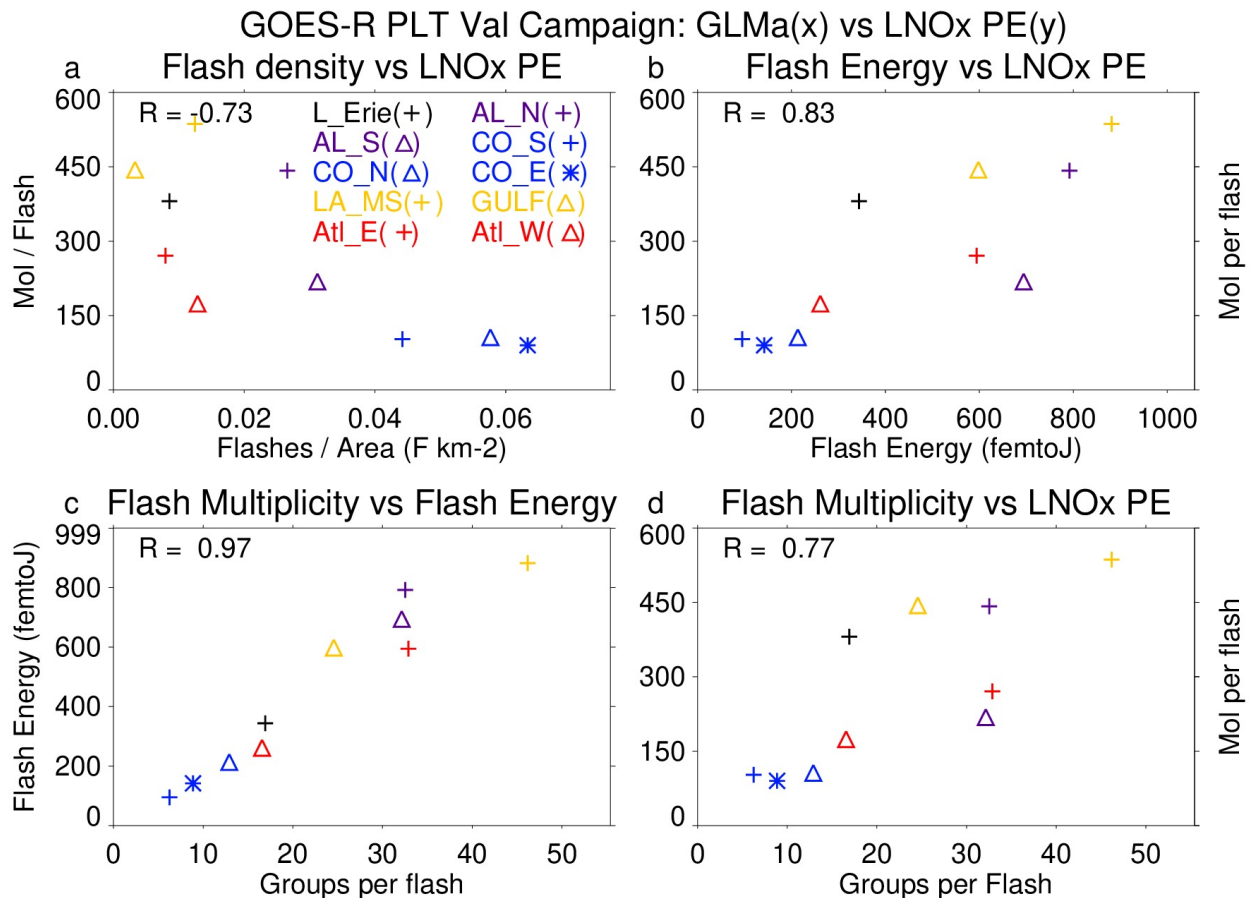
964 representation of global lightning for present day. Therefore, the negative LNO_x emissions change
 965 from this scheme may be more realistic. If indeed the ice flux scheme better represents the current
 966 distribution of lightning, both the Romps and Finney results suggest LC increase in LNO_x
 967 emission in future climate, and possibly a small global decrease. Murray (2018) points out that the
 968 ice flux scheme is a closer representation of the underlying charging mechanism, but this scheme
 969 needs to be tested in multiple global chemistry and climate models.

970

971 3.5.4. Recent findings concerning LNO_x PE

972 Recent satellite-based estimates of LNO_x production (Figure 23) have suggested a possible flash
 973 rate dependence of LNO_x production per flash (Bucsela et al., 2019; Allen et al., 2019; 2021).
 974 Smaller values of LNO_x PE in these studies were found to be associated with high flash rates,
 975 likely due to smaller flashes in these conditions (Bruning and Thomas, 2015). Allen et al. (2021a)
 976 noted positive correlations (Figure 23) of LNO_x PE with flash energy and with flash multiplicity
 977 (number of strokes per flash). Laboratory studies by Wang et al. (1998) found a positive correlation
 978 between peak current and LNO_x production. Koshak et al. (2015) found an 8% increase in peak
 979 current from the 2003-2007 period to the 2008-2012 period that accompanied the 12.8% decrease
 980 in CG flashes. These findings make it difficult to project future LNO_x production given only a
 981 prediction of future lightning flashes.

982



983

984 Figure 23. Scatterplots showing the GLMa-derived relationship between (a) LNO_x PE (mol per
 985 flash) and flash density (flashes km⁻²), (b) LNO_x PE and flash energy (fJ), (c) flash energy and

986 flash multiplicity, and (d) LNO_x PE and flash multiplicity. Colors are used to separate flight days
987 while symbols are used to separate system within each flight day. Correlations are shown in the
988 upper right. LNO_x PE derived from airborne remote sensor, the Geo-CAPE Airborne Simulator
989 (GCAS) during the GOES-R Post-launch Test field campaign. GLMa indicates Geostationary
990 Lightning Mapper data adjusted for missing data. From Allen et al. (2021a).

991

992 **3.5.5. Impacts of LNO_x on upper tropospheric O₃**

993 The literature concerning the effects of lightning NO_x production on upper tropospheric ozone
994 focuses on photochemical ozone production in storm outflow The STERAO-A storm simulation
995 by DeCaria et al. (2005) indicated that additional ozone production attributable to lightning NO
996 within the storm cloud during the lifetime of the storm was very small (~2 ppbv). However,
997 simulation of the photochemistry over the 24 hours following the storm showed that an additional
998 10 ppbv of ozone production in the upper troposphere can be attributed to lightning NO production.
999 Convective transport of HO_x precursors led to the generation of a HO_x plume, which substantially
1000 aided the downstream ozone production. Ott et al. (2007) simulated the July 21, 1998 EULINOX
1001 thunderstorm. During the storm, the inclusion of lightning NO_x in the model combined with
1002 convectively-transported boundary layer NO_x from the Munich, Germany region resulted in
1003 sufficiently large NO_x mixing ratios to cause a small titration loss of ozone (on average less than
1004 4 ppbv) at all model levels. Simulations of the chemical environment in the 24 hours following the
1005 storm show on average a small increase in the net production of ozone at most levels resulting
1006 from lightning NO_x, maximizing at approximately 5 ppbv per day at 5.5 km. Between 8 and 10.5
1007 km, lightning NO_x caused decreased net ozone production. Ren et al. (2008) found that net
1008 tropospheric ozone production proceeded at a median rate of ~11 ppbv per day above 9 km in the
1009 Intercontinental Transport Experiment (INTEX-A) in which the effects of frequent deep
1010 convection over the United States dominated the upper troposphere. Apel et al. (2012) noted that
1011 a box model calculation indicated a net ozone increase of ~10 ppbv over a few hours following
1012 observed convection with lightning over Canada in the Arctic Research of the Composition of the
1013 Troposphere from Aircraft and Satellite (ARCTAS) experiment. Apel et al. (2015) performed box
1014 modeling of the chemistry downwind of two DC3 storms in northeast Colorado on June 22, 2012
1015 finding greater ozone production over 2 days (14 ppbv) in the southern storm with more LNO_x
1016 than in the northern storm (11 ppbv). Brune et al. (2018) studied ozone production in the outflow
1017 of the June 21, 2012 DC3 mesoscale convective system. Their Box model calculations yielded a
1018 13 ppbv increase in ozone over 5 hours, similar to the observed 14 ppbv increase. This rate of
1019 increase is larger than others in the literature, perhaps because for a portion of the 5 hours the
1020 outflow was in cirrus cloud, in which photolysis rates may have been larger than clear-sky values
1021 due to multiple scattering. Using a regional chemistry model, Pickering et al. (2023) estimated that
1022 net ozone production in the upper tropospheric outflow of a severe high flash rate storm observed
1023 over Oklahoma proceeded at a rate of 10-11 ppbv day⁻¹ during the first 24 hours of downwind
1024 transport. Downwind photochemical production of ozone due to LNO_x accounted for much of the
1025 recovery of upper tropospheric ozone following large reductions due to convective transport of
1026 lower ozone boundary layer air.

1027 **3.5.6. Summary of LNO_x**

1028 LNO_x is responsible for the largest fraction of upper tropospheric ozone in the tropics year-round
1029 and in the mid-latitudes in summer. Effects on longwave radiation due to ozone are most sensitive
1030 due to the ozone near the tropopause. Therefore, it is of great importance to have knowledge of
1031 the trends in ozone in this region that are due to changes in frequency and characteristics of

1032 lightning flashes. Considerable uncertainty remains concerning trends in global thunder days. No
1033 long-term trend in global flash rates has been found. However, regionally important trends have
1034 been noted in CONUS and in China, which tend to be correlated to the decreasing atmospheric
1035 aerosol content. An increasing trend at Arctic latitudes has been noted, as that region rapidly
1036 warms. Future trends in flash rate also are uncertain, with conflicting predictions coming from
1037 models with differing flash rate parameterizations. Flash characteristics (e.g., flash rate, flash
1038 extent, flash energy or peak current, intracloud fraction) have been found to have important
1039 implications for LNO_x production per flash. Insufficient knowledge of these characteristics on a
1040 global scale makes it highly uncertain to estimate changes in LNO_x production, even with
1041 knowledge of flash rate trends.

1042

1043 **3.6. Soil NO and HONO emissions and their impacts on O₃**

1044 Nitrous acid (HONO) is produced from microbial activity in soils with a similar mechanism and
1045 strength as NO (Oswald et al., 2013). This emission source may partially account for the current
1046 mismatch between observed and simulated HONO levels in the lower troposphere (Su et al.,
1047 2011; Yang et al., 2020). Zhang et al. (2016) estimate a 29 % contribution of soil-HONO to the
1048 HONO sources in China. This may also contribute substantially to OH production with important
1049 implications for the HO_x and O₃ budget. To account for this emission source and assess the
1050 global potential for atmospheric pollution soil-HONO emissions have been parameterized based
1051 on the HONO/NO emission ratio measured at multiple field samples (taken from different
1052 regions of the world) and up-scale it to the 4 major land cover types applied to the whole globe.
1053 The study estimates a global emission source of 7 TgN/yr from soil-HONO in 2009 (Emmerichs
1054 et al., 2023). This is at the lower end of the estimated range of 7.4-12 TgN/yr presented by Wu et
1055 al. (2022) for 2017 who employ an empirical and statistical model in combination with
1056 observations. Due to the importance of NO and HONO soil emissions for the O₃ budget their
1057 variability and historical and future trends are described here and linked to O₃. Additionally, we
1058 discuss a modification of the soil NO emission scheme.

1059 **3.6.1. Global modeling of reactive nitrogen emissions from soil**

1060 In this section, we present a short overview of the soil-NO emission algorithms and estimates for
1061 regional and global emissions. The emission of nitrogen oxides (NO) from the soil is the major
1062 source of NO_x in unpolluted regions accounting for 15-25 % of global emissions (Weng et al.,
1063 2020, Vinken et al., 2014). Thereby, NO is produced from the nitrification in soil (microbial
1064 activity) and depends non-linearly on soil properties like pH, carbon and nutrient content,
1065 temperature, and soil moisture (Gödde and Conrad 2000, Oswald et al. 2013). Model algorithms
1066 estimate soil-NO emissions with a function dependent on biological and meteorological drivers.
1067 The common empirical approach by Yienger and Levy (1995), which is used in the current
1068 CMIP6 simulations (Szopa et al. 2022), is based on a biome-specific emission factor, soil
1069 temperature, precipitation, and the canopy uptake reduction factor. The resulting global estimate
1070 is in the range of 3.3-7.7 TgN/yr which is, however, only at the lower end of the more recent
1071 model and observation-based estimates. The Yienger and Levy (1995) approach generally
1072 underestimates soil NO for all landcover types except in the tundra and rainforest due to the
1073 pulsing parameterization, which describes a large NO_x release at the wetting of very dry soil and
1074 the subsequent rapid decay (Steinkamp et al., 2009). This is accounted for in the more
1075 mechanistic approach by Hudman et al. (2012) representing pulsing of the emissions following
1076 dry spells and N-inputs from chemical fertilizer and atmospheric N-deposition. This approach
1077 calculates spatial and temporal patterns of soil moisture, temperature, pulsing, fertilizer, manure

1078 and atmospheric N deposition and biome overall replacing the emission factors by Yienger and
 1079 Levy (1995) which yields in comparison 34 % more annual global soil emissions of nitrogen
 1080 oxide (10.7 TgN/yr). Satellite top-down estimates range from 7.9 TgN/yr (Miyazaki et al., 2017:
 1081 2005-2014, assimilation of satellite data sets) to 16.7 TgN/yr (Vinken et al., 2014; GEOS-Chem
 1082 and OMI). The emission of soil-NO varies regionally with small sources in Australia (~0.5
 1083 TgN/yr), Europe, Russia and Southern Hemisphere (SH) Africa (0.7 TgN/yr, 0.8 TgN/yr),
 1084 America (0.9-1 TgN/yr) and high values in S.E. Asia and Northern Hemisphere (NH) Africa (2-
 1085 2.1 TgN/yr). The emission estimates (here for 0.25° lat. \times 0.3125° lon.) increase with resolution
 1086 in some regions like Europe by 38 % (Weng et al., 2020).

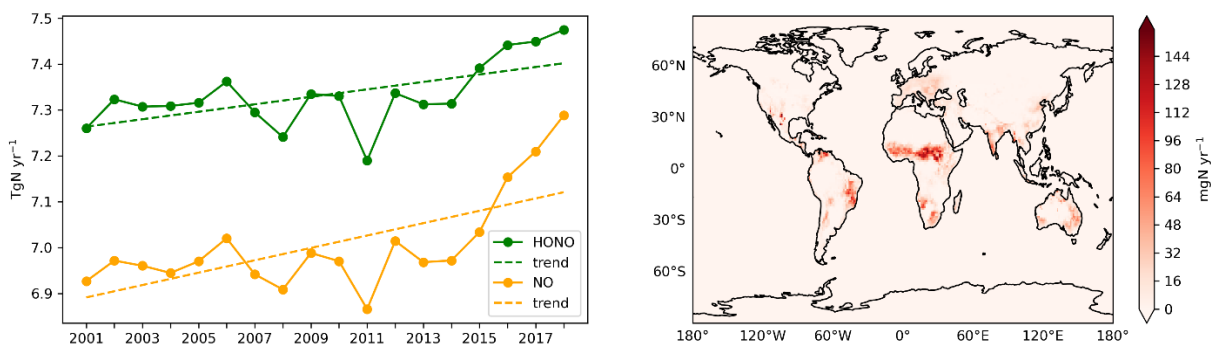
1087 Nitrous acid (HONO), a major OH source, is also produced from microbial activity in soils with
 1088 a similar mechanism and strength as NO (Oswald et al., 2013). This additional emission source
 1089 may account for the current mismatch between models and measurements representing HONO
 1090 levels in the lower troposphere (Su et al., 2011; Yang et al., 2020). Soil emissions of HONO play
 1091 a major role in the daytime-HONO concentrations in rural areas (in the lowest layers) where
 1092 traffic emissions and NO₂ heterogeneous reactions occur less than in urban areas (Wu et al.
 1093 2022). HONO photolysis is a main OH source and impacts the oxidation capacity of the
 1094 atmosphere (Zhang 2016, 2019). Therefore, this may also contribute significantly to OH
 1095 production with important implications for the HO_x and O₃ budget.

1096 3.6.2. Variability and trends of soil emissions of NO and HONO in the last 15 years

1097 The magnitude of soil emissions varies strongly with season where the emissions rise from
 1098 January and July by a factor of 2.5 (Weng et al., 2020). This follows the meteorological
 1099 variability as for instance, heavy rainfall over dry grasslands/forests causes a pulse of soil NO
 1100 emissions coupled with the usage of fertilizer (Hudman et al., 2012). According to the CCM1
 1101 simulations by Jöckel et al. (2016) (following the future ('medium high') climate scenario
 1102 RCP6.0 the soil NO emissions show a positive trend since pre-industrial times with a steeper
 1103 increase of up to 0.3 TgN/decade from the year 2000. As soil emissions of HONO rely on the
 1104 same biogeochemical process with similar dependencies on temperature and water content as NO
 1105 also increased from 2000 to 2019.

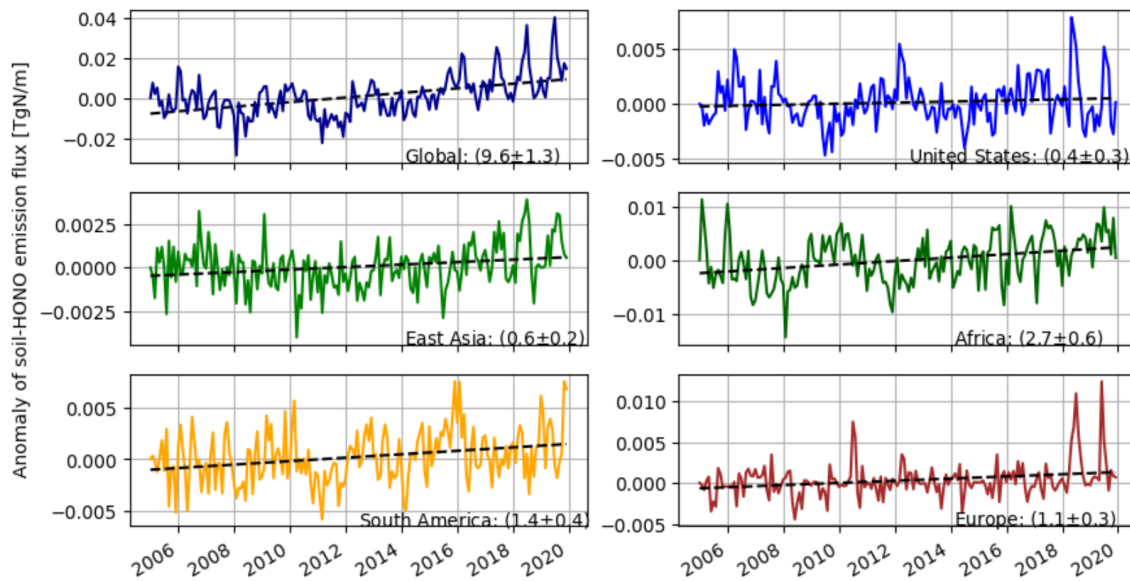
1106 For soil-HONO, however, the trend over 2005-2019 is much smaller, most pronounced in
 1107 Central Africa (Figure 25). Thereby, the highest positive monthly anomalies occur mainly in the
 1108 5 most recent years which is likely due to the more frequent heat wave occurrence, e.g. in Europe
 1109 and North America. Overall, Africa relates the most (~30%) to the global anomaly (Figure 24 -
 1110 Figure 25).

1111



1112

1113 Figure 24: Time series of soil-HONO and soil-NO emissions and their trends (left) and the mean
 1114 global distribution of the soil-HONO emission trend for 2005-2019 based on monthly anomalies
 1115 (right).
 1116

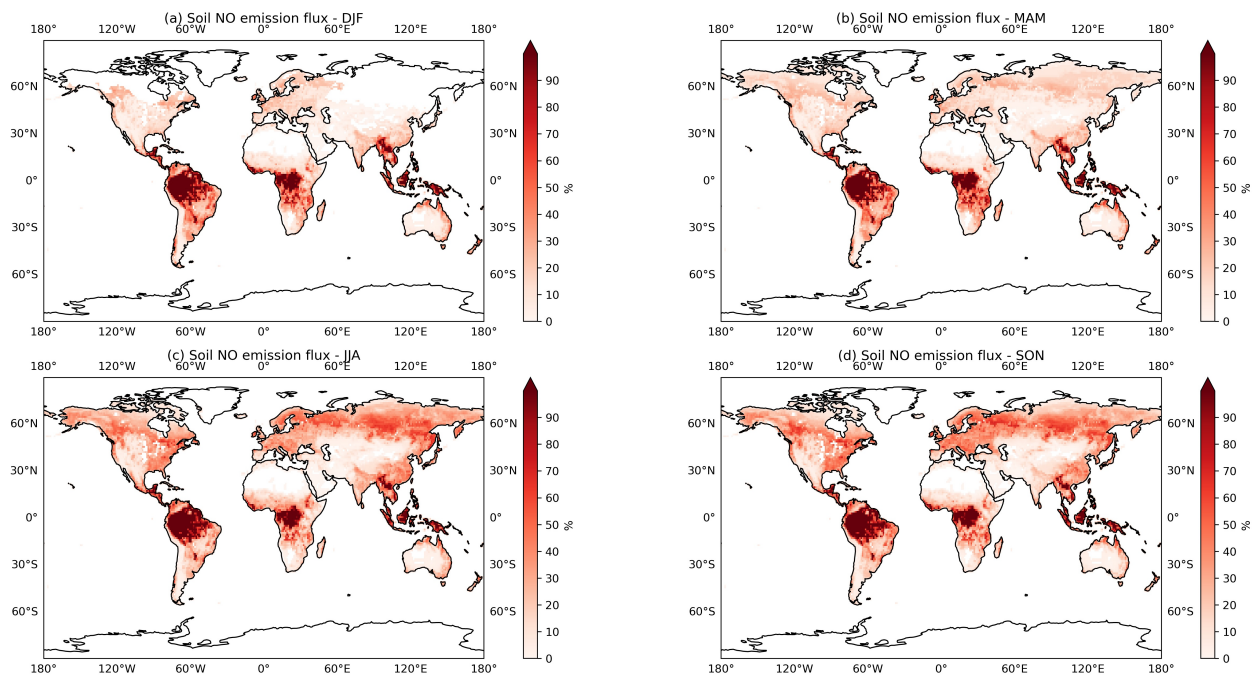


1117
 1118 Figure 25: Monthly anomalies of HONO emissions from soil (de-seasonalized). The trend is
 1119 given in 10^{-5} , including the uncertainty estimate ($2 \times$ standard deviation).

1120 3.6.3. Canopy Reduction Factor

1121 Most NO soil emission models (Yienger and Levy, 1995; Hudman et al., 2012) rely on an
 1122 empirical canopy reduction scheme which represents loss processes in plants as the diffusion of
 1123 NO_2 through the stomata and direct deposition to the cuticle. In particular, a large fraction of
 1124 NO_x (and peroxyacyl nitrate) loss during the night may be only explainable by non-stomatal
 1125 processes (Delaria et al., 2020b). Mechanistically, the canopy reduction can be described by an
 1126 efficient NO_x deposition to plants. Thus, Delaria et al. (2020a) points out that models already
 1127 represent the uptake by vegetation and do not need to use a canopy reduction scheme. The
 1128 potential change of NO soil emissions is shown by employing the global model
 1129 ECHAM/MESy ($1^\circ \times 1^\circ$) with an explicit trace gas uptake at stomata and cuticle (Emmerichs et
 1130 al., 2021) for two different seasons in 2005 and 2006. Removing the canopy reduction factor in
 1131 the model leads to a HC increase of soil NO emissions highest over tropical forests (Figure 26).
 1132 The temporal variation follows the vegetational growth as in the Northern Hemisphere summer
 1133 50% higher emissions occur. These findings are reasonable as Hudman et al. (2012) estimated
 1134 that the canopy reduction scheme overall lowers the NO emissions by 10-15% in grasslands and
 1135 up to 85% over forests (GEOS-Chem at $2^\circ \times 2.5^\circ$ in 2006). Consequently, improper accounting
 1136 for the canopy reduction factor may imply a strong underestimation of the soil-N in densely
 1137 forested regions and globally by about 31% (2005-2006).

1138



1139

1140 Figure 26: Relative difference Canopy Reduction soil HONO

1141

1142 3.6.4. Projections of soil NO and variability in different climates

1143 The future land use is predicted to change as a consequence of the growing demand for
 1144 nutrition and biofuels which implies an increasing use of fertilizer. Consequently, NO soil
 1145 emissions are estimated to rise by ~28% during the century to 11.5 TgN/yr at the end of 2100
 1146 (Fowler et al., 2015). Similarly, Liu et al. (2021) estimate an increasing soil NO emission of 8.9
 1147 TgN/yr by the year 2050 due to intensive nitrification processes.

1148 An increase of LAI by 10 %, in contrast, would lead to 1% lower emissions. In addition, several
 1149 responses are expected from the changing climate. In fact, the 1°C higher temperature would
 1150 cause ~5% increase in emissions (Weng et al., 2020). Following the future (‘medium high’)
 1151 climate scenario RCP6.0 (Representative Concentration Pathway, 6 W/m² radiative forcing until
 1152 2500, stabilization after 2150) used for the CMIP5 (Climate Model Intercomparison Project)
 1153 simulations. Jöckel et al. (2016) suggest an increase of ~15 % in soil NO emissions due to
 1154 increasing soil temperature (an increase of soil microbes) from present-day (2010) until 2100.
 1155 However, the most significant implications for large-scale denitrification activity are changing
 1156 rainfall and the regional hydrological cycles (Fowler et al., 2015). In general, soil NO_x will play
 1157 a more important role in the global budget in the troposphere due to the decreasing
 1158 anthropogenic emissions in the future. Therefore, increasing NO_x-soil emissions may slow down
 1159 the decrease of O₃ in response to declining anthropogenic emissions (Wu et al. 2022).

1160

1161 3.6.5. Next steps with biogeochemical models implemented in ESMs

1162 Uncertainties of modeling soil nitrogen emissions are associated with the model input and
 1163 parameters (Wang and Chen 2012). Process-based biogeochemical models which also consider
 1164 the complexity of soil emission processes as DNDC (Denitrification–Decomposition) are needed
 1165 (Li et al., 2011). The capability to represent interactive biogeochemical cycles allows for

1166 instance for the online calculation of crop nutrition from soil. Also, a model like CLM5
1167 distinguishes between natural and agricultural soils which more accurately predicts the fertilizer
1168 usage (Fung et al., 2022). Resolving the soil and litter biogeochemical dynamics vertically, in
1169 addition, lead to a more efficient retainment and recycling of N by the ecosystem (Koven et al.,
1170 2013). However, these models should be calibrated to multiple sites (Wang et al., 2019) which is
1171 limited by the availability of measurement data, especially when it comes to global modeling.

1172

1173 **4. Conclusion**

1174 In this article, we investigate temporal and spatial trends and variability of tropospheric ozone in
1175 relation to its precursors using satellite products, ozonesonde measurements, and model
1176 simulations. Our results show that ozone has positive trends at all latitudes and column depths
1177 regardless of the tropopause height within ± 100 hPa. The positive trends in the 30-60°N band are
1178 due to increasing trends over Canada and Alaska and are slightly offset by the small negative
1179 trends over the northeastern US and Europe. The lower trends in the bands 30-60°N and 30-60°S
1180 are due to the offsetting impact of negative trends over Eastern US and Europe in the north, and
1181 Australia and South Africa in the south, respectively. The decreasing trends of TrC-O₃ over parts
1182 of the northeastern US and Europe are likely due to the decreasing trend of TrC-NO₂, which is
1183 due to the effective measures applied over the last two decades to mitigate air pollution in these
1184 regions. TrC-HCHO trends are decreasing in the Eastern US, some parts of northern and western
1185 Africa, and western and northern Europe, and increasing in South Asia, central Africa, northern
1186 Australia, and Brazil. TrC-HCHO trends are consistent with that of TrC-O₃ over northeastern US
1187 and Europe. Simulated O₃ and its precursors are in good agreement with satellite measurements.
1188 Considering different latitude bands, the TrC-O₃ highest trends are simulated between 30° S and
1189 60° N, consistent with calculated trends based on satellite observations. The middle and upper
1190 troposphere make the largest contributions to the simulated TrC-O₃ trend globally, with large
1191 contributions from the upper troposphere driving the simulated TrC-O₃ trend at 30°S-30°N and
1192 counteracting the negative TrC-O₃ trend in the southern midlatitudes.

1193 We have also shed light on NO_x lightning and its relation to ozone trends. LNO_x is responsible
1194 for the largest fraction of upper tropospheric ozone in the tropics year-round and in the mid-
1195 latitudes in summer. Ozone Radiative forcing is due to the ozone near the tropopause. An
1196 increasing trend of LNO_x at Arctic latitudes has been noted, as that region rapidly warms.
1197 However, future trends in flash rate are uncertain, with conflicting predictions coming from
1198 models with differing flash rate parameterizations. Soil HONO emissions had their highest
1199 positive monthly anomalies mainly in the 5 most recent years which is likely due to the more
1200 frequent heat wave occurrence, e.g. in Europe and North America. Soil HONO trends are highest
1201 in Africa accounting for ~30% of the global anomaly. Soil NO_x emissions could play an
1202 important role in the tropospheric NO_x global budget due to the decreasing anthropogenic
1203 emissions in the future. Therefore, the expected increase in NO_x-soil emissions may slow down
1204 the decrease of O₃ in response to declining anthropogenic emissions. Overall, this study
1205 presented a comprehensive overview of tropospheric ozone trends in relation to its precursors in
1206 different spatial and temporal scales.

1207 Competing interests: At least one of the (co-)authors is a member of the editorial board of
1208 Atmospheric Chemistry and Physics

1209 Author contribution: YE led the conceptualization, writing, and review of the article, JZ led the
1210 OMI ozone satellite product and data analysis, SS led the GEOS 5 GMI data analysis, HP led the

1211 sections on HCHO, NO₂, HCHO/NO₂ data analysis and contributed to the CO analyses, KM led
1212 the comparison of different satellite products, KP lead the lightning NO_x section, HW and RB
1213 contributed to the CO analysis, DT and TE led the section on HONO soil emission, all authors
1214 contribute to the writing and review of the article.

1215

1216 **Acknowledgment**

1217 This study was partially funded by the NSF AGS, grant number 1900795, USF Creative
1218 Scholarship Grant 2022. A part of the research was conducted at the Jet Propulsion Laboratory,
1219 California Institute of Technology, under a contract with NASA. HP has received funding from
1220 the Ministerio de Ciencia e Innovación through the MITIGATE project (grant no. PID2020-
1221 113840RA-I00 funded by MCIN/AEI/10.13039/501100011033) and the Ramon y Cajal grant
1222 (RYC2021-034511-I, MCIN / AEI / 10.13039/501100011033 and European Union
1223 NextGenerationEU/PRTR). The GEOS-GMI simulation was supported by the NASA's Making
1224 Earth System Data Records for Use in Research Environments (MEaSUREs) program and the
1225 high-performance computing resources for GEOS-GMI were provided by the NASA Center for
1226 Climate Simulation (NCCS). A part of the research was supported by the NSF National Center
1227 for Atmospheric Research, which is a major facility sponsored by the U.S. National Science
1228 Foundation under Cooperative Agreement No. 1852977. We acknowledge the support of the
1229 National Aeronautics and Space Administration (NASA) Atmospheric Composition: Aura
1230 Science Team Program (19-AURAST19-0044), Atmospheric Composition Modeling and
1231 Analysis Program (22-ACMAP22-0013), NASA Earth Science U.S. Participating Investigator
1232 program (22-EUSPI22-0005).

1233 **5. References**

- 1234 Allen, D., Pickering, K., Duncan, B., and Damon, M.: Impact of lightning NO emissions on
1235 North American photochemistry as determined using the Global Modeling Initiative
1236 (GMI) model, *J. Geophys. Res.*, 115, D22301, doi:10.1029/2010JD014062, 2010.
- 1237 Allen, D. J., Pickering, K. E., Pinder, R. W., Henderson, B. H., Appel, K. W., and Prados, A.:
1238 Impact of lightning-NO on eastern United States photochemistry during the summer
1239 of 2006 as determined using the CMAQ model, *Atmos. Chem. Phys.*, 12, 1737-1758,
1240 doi:10.5194/acp-12-1737-2012, 2012.
- 1241 Allen, D. J., Pickering, K. E., Lamsal, L., Mach, D., Quick, M. G., Lapierre, J., Janz, S.,
1242 Koshak, W., Kowalewski, M. & Blakeslee, R.: Observations of Lightning NO_x
1243 production from GOES-R Post Launch Test Field Campaign Flights, *J. Geophys.*
1244 *Res.*, 126 (8), <https://doi.org/10.1029/2020JD033769>, 2021a.
- 1245 Allen, D. J., Pickering, K. E., Bucsela, E., van Geffen, J., Lapierre, J., Koshak, W., & Eskes,
1246 H.: Observations of Lightning NO_x production from Tropospheric Ozone Monitoring
1247 Instrument Case Studies over the United States, *J. Geophys. Res.*, 126 (10),
1248 <https://doi.org/10.1029/2020JD034174>, 2021b.
- 1249 Allen, D., J., Pickering, K. E., Bucsela, E., Krotkov, N., and Holzworth, R.: Lightning NO_x
1250 Production in the Tropics as Determined Using OMI NO₂ Retrievals and WLLN
1251 Stroke Data, *J. Geophys. Res.*, <https://doi.org/10.1029/2018JD029824>, 2019.
- 1252 Apel, E. C., J. R. Olson, J. H. Crawford, R. S. Hornbrook, A. J. Hills, C. A. Cantrell, L. K.
1253 Emmons, D. J. Knapp, S. Hall, R. L. Mauldin III, A. J. Weinheimer, A. Fried, D. R.
1254 Blake, J. D. Crouse, J. M. St. Clair, P. O. Wennberg, G. S. Diskin, H. E. Fuelberg,

- 1255 A. Wisthaler, T. Mikoviny, W. Brune, and Riemer, D.: Impact of the deep convection
 1256 of isoprene and other reactive trace species on radicals and ozone in the upper
 1257 troposphere, *Atmos. Chem. Phys.*, 12, 1135–1150, [www.atmos-chem-](http://www.atmos-chem-phys.net/12/1135/2012/doi:10.5194/acp-12-1135-2012)
 1258 [phys.net/12/1135/2012/doi:10.5194/acp-12-1135-2012](http://www.atmos-chem-phys.net/12/1135/2012/doi:10.5194/acp-12-1135-2012), 2012.
- 1259 Apel, E. C., et al.: Upper tropospheric ozone production from lightning NO_x-impacted
 1260 convection: Smoke ingestion case study from the DC3 campaign, *J. Geophys. Res.*
 1261 *Atmos.*, 120, doi:10.1002/2014JD022121, 2015.
- 1262 Archibald, A.T., et al.: Tropospheric Ozone Assessment Report: A critical review of changes
 1263 in the tropospheric ozone burden and budget from 1850 to 2100. *Elem Sci Anth*, 8: 1.
 1264 DOI: <https://doi.org/10.1525/elementa.2020.034>, 2020.
- 1265 ASDC, MOPITT CO gridded monthly means (Near and Thermal Infrared Radiances) V009
 1266 [Data set]. NASA Langley Atmospheric Science Data Center DAAC. Retrieved from
 1267 <https://doi.org/10.5067/TERRA/MOPITT/MOP03JM.009>, 2024.
- 1268 Barret, B., De Mazière, M., and Mahieu, E.: Ground-based FTIR measurements of CO from
 1269 the Jungfraujoch: characterisation and comparison with in situ surface and MOPITT
 1270 data, *Atmos. Chem. Phys.*, 3, 2217–2223, <https://doi.org/10.5194/acp-3-2217-2003>,
 1271 2003.
- 1272 Bauwens, M.; Compornolle, S.; Stavrakou, T.; Müller, J.; Gent, J.; Eskes, H.; Levelt, P.F.;
 1273 van der A, R.; Veefkind, J.P.; Vlietinck, J.; et al. Impact of Coronavirus Outbreak on
 1274 NO₂ Pollution Assessed Using TROPOMI and OMI Observations. *Geophys. Res.*
 1275 *Let.*, 47, 2020.
- 1276 Beirle, S., Huntrieser, H., and Wagner, T.: Direct satellite observation of lightning-produced
 1277 NO_x, *Atmos. Chem. Phys.*, 10, 10965–10986, [https://doi.org/10.5194/acp-10-10965-](https://doi.org/10.5194/acp-10-10965-2010)
 1278 2010, 2010.
- 1279 Boersma, K., Eskes, H., Richter, A., De Smedt, I., Lorente, A., Beirle, S., Van Geffen, J.,
 1280 Peters, E., Van Roozendaal, M., and Wagner, T.: QA4ECV NO₂ tropospheric and
 1281 stratospheric vertical column data from OMI (Version 1.1) (data set), Royal
 1282 Netherlands Meteorological Institute (KNMI), [https://doi.org/10.21944/qa4ecv-no2-](https://doi.org/10.21944/qa4ecv-no2-omi-v1.1)
 1283 [omi-v1.1](https://doi.org/10.21944/qa4ecv-no2-omi-v1.1), 2017a.
- 1284 Boersma, K., Eskes, H., Richter, A., De Smedt, I., Lorente, A., Beirle, S., Van Geffen, J.,
 1285 Peters, E., Van Roozendaal, M., and Wagner, T.: QA4ECV NO₂ tropospheric and
 1286 stratospheric vertical column data from GOME-2 (Version 1.1) (data set), Royal
 1287 Netherlands Meteorological Institute (KNMI), [https://doi.org/10.21944/qa4ecv-no2-](https://doi.org/10.21944/qa4ecv-no2-gome2a-v1.1)
 1288 [gome2a-v1.1](https://doi.org/10.21944/qa4ecv-no2-gome2a-v1.1), 2017b.
- 1289 Boersma, K., Eskes, H., Richter, A., De Smedt, I., Lorente, A., Beirle, S., Van Geffen, J.,
 1290 Peters, E., Van Roozendaal, M., and Wagner, T.: QA4ECV NO₂ tropospheric and
 1291 stratospheric vertical column data from SCIAMACHY (Version 1.1) (data set), Royal
 1292 Netherlands Meteorological Institute (KNMI), [https://doi.org/10.21944/qa4ecv-no2-](https://doi.org/10.21944/qa4ecv-no2-sciav1.1)
 1293 [sciav1.1](https://doi.org/10.21944/qa4ecv-no2-sciav1.1), 2017c.
- 1294 Boersma, K. F., Eskes, H. J., Richter, A., De Smedt, I., Lorente, A., Beirle, S., van Geffen, J.
 1295 H. G. M., Zara, M., Peters, E., Van Roozendaal, M., Wagner, T., Maasackers, J. D.,
 1296 van der A, R. J., Nightingale, J., De Rudder, A., Irie, H., Pinardi, G., Lambert, J.-C.,
 1297 and Compornolle, S. C.: Improving algorithms and uncertainty estimates for satellite
 1298 NO₂ retrievals: results from the quality assurance for the essential climate variables

- 1299 (QA4ECV) project, *Atmos. Meas. Tech.*, 11, 6651–6678, [https://doi.org/10.5194/amt-](https://doi.org/10.5194/amt-11-6651-2018)
1300 11-6651-2018, 2018.
- 1301 Brune, W. H., et al.: Atmospheric oxidation in the presence of clouds during the Deep
1302 Convective Clouds and Chemistry (DC3) study, *Atmos. Chem. Phys.*, 18, 14493–14510,
1303 2018, <https://doi.org/10.5194/acp-18-14493-2018>, 2018.
- 1304 Bruning, E. C. & Thomas, R. J.: Lightning channel length and flash energy determined from
1305 moments of the flash area distribution, *J. Geophys. Res. Atmos.*, 120, 8925–8940,
1306 doi:[10.1002/2015JD023766](https://doi.org/10.1002/2015JD023766), 2015.
- 1307 Buchholz, R.R.; Deeter, M.N.; Worden, H.M.; Gille, J.; Edwards, D.P.; Hannigan, J.W.;
1308 Jones, N.B.; Paton-Walsh, C.; Griffith, D.W.T.; Smale, D.; et al.: Validation of
1309 MOPIIT carbon monoxide using ground-based Fourier transform infrared
1310 spectrometer data from NDACC. *Atmos. Meas. Tech.* 10, 1927–1956, 2017.
- 1311 Buchholz, R. R., Worden, H. M., Park, M., Francis, G., Deeter, M. N., Edwards, D. P.,
1312 Emmons, L. K., Gaubert, B., Gille, J., Martinez-Alonso, S., Tang, W., Kumar, R.,
1313 Drummond, J. R., Clerbaux, C., George, M., Coheur, P.-F., Hurtmans, D., Bowman,
1314 K. W., Luo, M., Payne, V. H., Worden, J. R., Chin, M., Levy, R. C., Warner, J., Wei,
1315 Z., and Kulawik, S. S.: Air pollution trends measured from Terra: CO and AOD over
1316 industrial, fire-prone, and background regions, *Remote Sens. Environ.*, 256, 112275,
1317 <https://doi.org/10.1016/j.rse.2020.112275>, 2021.
- 1318 Bucsel, E. J., K. E. Pickering, T. L. Huntemann, R. C. Cohen, A. Perring, J. F. Gleason, R.
1319 J. Blakeslee, R. I. Albrecht, R. Holzworth, J. P. Cipriani, D. Vargas-Navarro, I. Mora-
1320 Segura, A. Pacheco-Hernández, Laporte-Molina, S.: Lightning-generated NO_x seen
1321 by OMI during NASA’s TC⁴ experiment, *J. Geophys. Res.*, 115, D00J10,
1322 doi:10.1029/2009JD013118, 2010.
- 1323 Bucsel, E., Pickering, K. E., Allen, D., Holzworth, R., and Krotkov, N.: Midlatitude
1324 lightning NO_x Production Efficiency Inferred from OMI and WLLN Data, *J.*
1325 *Geophys. Res.*, <https://doi.org/10.1029/2019JD030561>, 2019.
- 1326 Canadell, J.G., P.M.S. Monteiro, M.H. Costa, L. Cotrim da Cunha, P.M. Cox, A.V. Eliseev,
1327 S. Henson, M. Ishii, S. Jaccard, C. Koven, A. Lohila, P.K. Patra, S. Piao, J. Rogelj, S.
1328 Syampungani, S. Zaehle, and K. Zickfeld: Global Carbon and other Biogeochemical
1329 Cycles and Feedbacks. In *Climate Change 2021: The Physical Science Basis.*
1330 *Contribution of Working Group I to the Sixth Assessment Report of the*
1331 *Intergovernmental Panel on Climate Change* [Masson-Delmotte, V., P. Zhai, A.
1332 Pirani, S.L. Connors, C. Péan, S. Berger, N. Caud, Y. Chen, L. Goldfarb, M.I. Gomis,
1333 M. Huang, K. Leitzell, E. Lonnoy, J.B.R. Matthews, T.K. Maycock, T. Waterfield, O.
1334 Yelekçi, R. Yu, and B. Zhou (eds.)]. Cambridge University Press, Cambridge, United
1335 Kingdom and New York, NY, USA, pp. 673–816, doi: [10.1017/9781009157896.007](https://doi.org/10.1017/9781009157896.007),
1336 2021.
- 1337 Cazorla, M. and Herrera, E.: An ozonesonde evaluation of spaceborne observations in the
1338 Andean tropics, *Sci Rep*, 12, <https://doi.org/10.1038/s41598-022-20303-7>, 2022.
- 1339 Chang K-L, Petropavlovskikh I, Cooper OR, Schultz MG, Wang T. Regional trend analysis
1340 of surface ozone observations from monitoring networks in eastern North America,
1341 Europe and East Asia. *Elem Sci Anth.*, 5:50. DOI: 10.1525/elementa.243, 2017.

- 1342 Chang, K.-L., Cooper, O. R., Gaudel, A., Petropavlovskikh, I., and Thouret, V.: Statistical
1343 regularization for trend detection: an integrated approach for detecting long-term
1344 trends from sparse tropospheric ozone profiles, *Atmos. Chem. Phys.*, 20, 9915–9938,
1345 <https://doi.org/10.5194/acp-20-9915-2020>, 2020.
- 1346 Chang, K.-L., Cooper, O. R., Gaudel, A., Allaart, M., Ancellet, G., Clark, H., et al.: Impact
1347 of the COVID-19 economic downturn on tropospheric ozone trends: An uncertainty
1348 weighted data synthesis for quantifying regional anomalies above western North
1349 America and Europe. *AGU Advances*, 3,
1350 e2021AV000542. <https://doi.org/10.1029/2021AV000542>, 2022.
- 1351 Chang K-L, Martin G. Schultz, Gerbrand Koren, Selke, N.: Guidance note on best statistical
1352 practices for TOAR analyses, <https://doi.org/10.48550/arXiv.2304.14236>, 2023.
- 1353 Chang, K.-L., Cooper, O. R., Gaudel, A., Petropavlovskikh, I., Effertz, P., Morris, G., and
1354 McDonald, B. C.: Technical note: Challenges of detecting free tropospheric ozone
1355 trends in a sparsely sampled environment, *EGUsphere* [preprint],
1356 <https://doi.org/10.5194/egusphere-2023-2739>, 2024.
- 1357 Chen, Z., Jane Liu, Xiushu Qie, Xugeng Cheng, Mengmiao Yang, Lei Shu, Zang, Z.:
1358 Stratospheric influence on surface ozone pollution in China, *Nature Communications*,
1359 10.1038/s41467-024-48406-x, **15**, 1, 2024.
- 1360 Christiansen, A., Mickley, L. J., Liu, J., Oman, L. D., and Hu, L.: Multidecadal increases in
1361 global tropospheric ozone derived from ozonesonde and surface site observations: can
1362 models reproduce ozone trends?, *Atmos Chem Phys*, 22, 14751–14782,
1363 <https://doi.org/10.5194/acp-22-14751-2022>, 2022.
- 1364 Cooper, O. R., Schultz, M. G., Schröder, S., Chang, K. L., Gaudel, A., Benítez, G. C.,
1365 Cuevas, E., Fröhlich, M., Galbally, I. E., Molloy, S., Kubistin, D., Lu, X., McClure-
1366 Begley, A., Nédélec, P., O’Brien, J., Oltmans, S. J., Petropavlovskikh, I., Ries, L.,
1367 Senik, I., Sjöberg, K., Solberg, S., Spain, G. T., Spangl, W., Steinbacher, M.,
1368 Tarasick, D., Thouret, V., and Xu, X.: Multi-decadal surface ozone trends at globally
1369 distributed remote locations, *Elementa*, 8, <https://doi.org/10.1525/elementa.420>, 2020.
- 1370 Cummings, K. A., T. L. Huntemann, and E. Pickering, K.: Cloud-resolving chemistry
1371 simulation of a Hector thunderstorm, *Atmos. Chem. Phys.*, 13(5), 2757-2777,
1372 doi:10.5194/acp-13-2757, 2013.
- 1373 DeCaria, A., K. Pickering, G. Stenchikov, J. Scala, J. Stith, J. Dye, B. Ridley, and Laroche,
1374 P.: A cloud-scale model study of lightning-generated NO_x in an individual
1375 thunderstorm during STERAO-A, *J. Geophys. Res.*, 105, 11,601-11,616, 2000.
- 1376 DeCaria, A. J., K. E. Pickering, G. L. Stenchikov, and E. Ott, L.: Lightning-generated NO_x
1377 and its impact on tropospheric ozone production: A three-dimensional modeling study
1378 of a STERAO-A thunderstorm, *J. Geophys. Res.*, 110, D14303,
1379 doi:10.1029/2004JD005556, 2005.
- 1380 Deeter, M., Francis, G., Gille, J., Mao, D., Martínez-Alonso, S., Worden, H., Ziskin, D.,
1381 Drummond, J., Commane, R., Diskin, G., and McKain, K.: The MOPITT Version 9
1382 CO product: sampling enhancements and validation, *Atmos. Meas. Tech.*, 15, 2325–
1383 2344, <https://doi.org/10.5194/amt-15-2325-2022>, 2022.

- 1384 De Smedt, I., Theys, N., Yu, H., Danckaert, T., Lerot, C., Compernelle, S., Van Roozendael,
1385 M., Richter, A., Hilboll, A., Peters, E., Pedergnana, M., Loyola, D., Beirle, S.,
1386 Wagner, T., Eskes, H., van Geffen, J., Boersma, K. F., and Veeffkind, P.: Algorithm
1387 theoretical baseline for formaldehyde retrievals from S5P TROPOMI and from the
1388 QA4ECV project, *Atmos. Meas. Tech.*, 11, 2395–2426, [https://doi.org/10.5194/amt-](https://doi.org/10.5194/amt-11-2395-2018)
1389 11-2395-2018, 2018
- 1390 Duncan, B. N., Strahan, S. E., Yoshida, Y., Steenrod, S. D., and Livesey, N.: Model study of
1391 the cross-tropopause transport of biomass burning pollution, *Atmos. Chem. Phys.*, 7,
1392 3713–3736, <https://doi.org/10.5194/acp-7-3713-2007>, 2007.
- 1393 Elguindi, N., Granier, C., Stavrou, T., Darras, S., Bauwens, M., Cao, H., Chen, C., Denier
1394 van der Gon, H. A. C., Dubovik, O., Fu, T. M., Henze, D. K., Jiang, Z., Keita, S.,
1395 Kuenen, J. J. P., Kurokawa, J., Liousse, C., Miyazaki, K., Müller, J. F., Qu, Z.,
1396 Solmon, F., and Zheng, B.: Intercomparison of Magnitudes and Trends in
1397 Anthropogenic Surface Emissions From Bottom-Up Inventories, Top-Down
1398 Estimates, and Emission Scenarios, *Earths Future*, 8, e2020EF001520,
1399 <https://doi.org/10.1029/2020EF001520>, 2020.
- 1400 Elshorbany, Y. F., Kurtenbach, R., Wiesen, P. Lissi, E., Rubio, M., Villena, G., Gramsch, E.,
1401 Rickard, A. R., Pilling, M. J., Kleffmann, J.: Oxidation capacity of the city air of
1402 Santiago, Chile, *Atmospheric Chemistry and Physics*, 9, 2257-2273, 2009.
- 1403 Elshorbany, Y. F., Barnes, I., Becker, K. H., Kleffmann, J., and Wiesen, P.: Sources and
1404 Cycling of Tropospheric Hydroxyl Radicals-An Overview, *Zeitschrift für*
1405 *Physikalische Chemie*, 224, 967-987, DOI:10.1524/zpch.2010.6136, 2010.
- 1406 Elshorbany, Y. F., Kleffmann, J., Hofzumahaus, A., Kurtenbach, R., Wiesen, P., Dorn, H.-P.,
1407 Schlosser, E., Brauers, T., Fuchs, H., Rohrer, F., Wahner, A., Kanaya, Y., Yoshino,
1408 A., Nishida, S., Kajii, Y., Martinez, M., Rudolf, M., Harder, H., Lelieveld, J., Elste,
1409 T., Plass-Dülmer, C., Stange, G., and Berresheim, H.: HO_x Budgets during
1410 HO_xComp: a Case Study of HO_x Chemistry under NO_x limited Conditions, *J.*
1411 *Geophys. Res.*, 117, D03307, doi: 10.1029/2011JD017008, 2012.
- 1412 Elshorbany, Y. F., Crutzen, P. J., Steil, B., Pozzer, A., Tost, H., and Lelieveld, J.: Global and
1413 regional impacts of HONO on the chemical composition of clouds and aerosols,
1414 *Atmos. Chem. Phys.*, 14, 1167–1184, <https://doi.org/10.5194/acp-14-1167-2014>,
1415 2014.
- 1416 Elshorbany, Y. F.: Hannah C. Kapper; Jerald R. Ziemke; A. Parr, S.: The Status of Air
1417 Quality in the United States During the COVID-19 Pandemic: A Remote Sensing
1418 Perspective . *Remote Sensing*, doi:10.3390/rs13030369, 2021.
- 1419 Fadnavis, S., Sagalgile, A., Sonbawne, S., Vogel, B., Peter, T., Wienhold, F. G., Dirksen, R.,
1420 Oelsner, P., Naja, M., and Müller, R.: Comparison of ozonesonde measurements in
1421 the upper troposphere and lower Stratosphere in Northern India with reanalysis and
1422 chemistry-climate-model data, *Sci Rep*, 13, 7133, [https://doi.org/10.1038/s41598-](https://doi.org/10.1038/s41598-023-34330-5)
1423 023-34330-5, 2023.
- 1424 Fehr, T., H. Höller, and Huntrieser, H.: Model study on production and transport of
1425 lightning-produced NO_x in a EULINOX supercell storm, *J. Geophys. Res.*, 109,
1426 D09102, doi:10.1029/2003JD003935, 2004.

- 1427 Finney, D. L., R. M. Doherty, O. Wild, H. Huntrieser, H. C. Pumphrey, and M. Blyth, A.:
 1428 Using cloud ice flux to parameterize large-scale lightning, *Atmos. Chem. Phys.*, 14,
 1429 12665–12682, www.atmos-chem-phys.net/14/12665/2014/ doi:10.5194/acp-14-
 1430 12665-2014, 2014.
- 1431 Finney, D. L., R. M. Doherty, O. Wild, P. J. Young, and Butler, A.: Response of lightning
 1432 NO_x emissions and ozone production to climate change: Insights from the
 1433 Atmospheric Chemistry and Climate Model Intercomparison Project, *Geophys. Res.*
 1434 *Lett.*, 43, 5492–5500, doi:[10.1002/2016GL068825](https://doi.org/10.1002/2016GL068825), 2016.
- 1435 Finney, D. L., R. M. Doherty, O. Wild, D. S. Stevenson, I. A. MacKenzie, and M. Blyth, A.:
 1436 A projected decrease in lightning under climate change, *Nature Climate Change*, 8,
 1437 210-213, 2018.
- 1438 Fiore, A. M., Jacob, D. J., Field, B. D., Streets, D. G., Fernandes, S. D., and Jang, C.: Linking
 1439 air pollution and climate change: The case for controlling methane, *Geophys. Res.*
 1440 *Lett.*, 29, 1919, doi:10.1029/2002GL015601, 2002.
- 1441 Fiore, A. M., L. W. Horowitz, E. J. Dlugokencky, and J. West, J.: Impact of meteorology and
 1442 emissions on methane trends, 1990–2004, *Geophys. Res. Lett.*, 33, L12809,
 1443 doi:10.1029/2006GL026199, 2006.
- 1444 Fisher, B. L., Lamsal, L. N., Fasnacht, Z., Oman, L. D., Joiner, J., Krotkov, N. A., ... &
 1445 Yang, E. S.: Revised estimates of NO₂ reductions during the COVID-19 lockdowns
 1446 using updated TROPOMI NO₂ retrievals and model simulations. *Atmospheric*
 1447 *Environment*, 326, 120459, 2024.
- 1448 Fleming, Z.L., Doherty, R.M., von Schneidmesser, E., Malley, C.S., Cooper, O.R., Pinto,
 1449 J.P., Colette, A., Xu, X., Simpson, D., Schultz, M.G., Lefohn, A.S., Hamad, S.,
 1450 Moolla, R., Solberg, S. and Feng, Z.: Tropospheric Ozone Assessment Report:
 1451 Present-day ozone distribution and trends relevant to human health, *Elem Sci Anth*,
 1452 6(1), p.12. DOI: 10.1525/elementa.73, 2018.
- 1453 Flynn, C. M., K. E. Pickering, J. H. Crawford, A. Weinheimer, K. L. Thornhill, C. Loughner,
 1454 Lee, P.: Variability of O₃ and NO₂ profile shapes during DISCOVER-AQ:
 1455 Implications for satellite observations and comparisons to model-simulated profiles,
 1456 *Atmos. Environ.*, 147, 133-156, 2016.
- 1457 Fortems-Cheiney, A., Chevallier, F., Pison, I., Bousquet, P., Szopa, S., Deeter, M. N., and
 1458 Clerbaux, C.: Ten years of CO emissions as seen from Measurements of Pollution in
 1459 the Troposphere (MOPITT), *J. Geophys. Res.*, 116, D05304,
 1460 <https://doi.org/10.1029/2010JD014416>, 2011.
- 1461 Fortems-Cheiney, A., Chevallier, F., Pison, I., Bousquet, P., Saunois, M., Szopa, S., Cressot,
 1462 C., Kurosu, T. P., Chance, K., and Fried, A.: The formaldehyde budget as seen by a
 1463 global-scale multi-constraint and multi-species inversion system, *Atmos. Chem.*
 1464 *Phys.*, 12, 6699–6721, <https://doi.org/10.5194/acp-12-6699-2012>, 2012.
- 1465 Forster, P., T. Storelvmo, K. Armour, W. Collins, J.-L. Dufresne, D. Frame, D.J. Lunt, T.
 1466 Mauritsen, M.D. Palmer, M. Watanabe, M. Wild, and H. Zhang, 2021: The Earth's
 1467 Energy Budget, Climate Feedbacks, and Climate Sensitivity. In *Climate Change*
 1468 *2021: The Physical Science Basis. Contribution of Working Group I to the Sixth*
 1469 *Assessment Report of the Intergovernmental Panel on Climate Change [Masson-*
 1470 *Delmotte, V., P. Zhai, A. Pirani, S.L. Connors, C. Péan, S. Berger, N. Caud, Y. Chen,*

- 1471 L. Goldfarb, M.I. Gomis, M. Huang, K. Leitzell, E. Lonnoy, J.B.R. Matthews, T.K.
 1472 Maycock, T. Waterfield, O. Yelekçi, R. Yu, and B. Zhou (eds.)]. Cambridge
 1473 University Press, 923 Cambridge, United Kingdom and New York, NY, USA, pp.
 1474 923–1054, doi:10.1017/9781009157896.009, 2021.
- 1475 Fullekrug, M. E. Williams, C. Price, S. Goodman, R. Holzworth, K. Virts, and Buechler
 1476 Sidebar, D.: Lightning, in State of the Climate: 2021, Bull. Amer. Meteor. Soc., 108,
 1477 S79-S81, doi:10.1175/BAMS-D-22-0092.1, 2022
- 1478 Fung, K. M., Val Martin, M., and Tai, A. P. K.: Modeling the interinfluence of fertilizer-
 1479 induced NH₃ emission, nitrogen deposition, and aerosol radiative effects using
 1480 modified CESM2, Biogeosciences, 19, 1635–1655, [https://doi.org/10.5194/bg-19-](https://doi.org/10.5194/bg-19-1635-2022)
 1481 1635-2022, 2022.
- 1482 Gaubert, B., Emmons, L. K., Raeder, K., Tilmes, S., Miyazaki, K., Arellano Jr., A. F., Elguindi,
 1483 N., Granier, C., Tang, W., Barré, J., Worden, H. M., Buchholz, R. R., Edwards, D. P.,
 1484 Franke, P., Anderson, J. L., Saunio, M., Schroeder, J., Woo, J.-H., Simpson, I. J.,
 1485 Blake, D. R., Meinardi, S., Wennberg, P. O., Crouse, J., Teng, A., Kim, M.,
 1486 Dickerson, R. R., He, H., Ren, X., Pusede, S. E., and Diskin, G. S.: Correcting model
 1487 biases of CO in East Asia: impact on oxidant distributions during KORUS-AQ, Atmos.
 1488 Chem. Phys., 20, 14617–14647, <https://doi.org/10.5194/acp-20-14617-2020>, 2020.
- 1489 Gaudel, A., Cooper, O.R., Ancellet, G., Barret, B., Boynard, A., Burrows, J.P., Clerbaux, C.,
 1490 Coheur, P.-F., Cuesta, J., Cuevas, E., Doniki, S., Dufour, G., Ebojie, F., Foret, G.,
 1491 Garcia, O., Granados Muños, M.J., Hannigan, J.W., Hase, F., Huang, G., Hassler, B.,
 1492 Hurtmans, D., Jaffe, D., Jones, N., Kalabokas, P., Kerridge, B., Kulawik, S.S., Latter,
 1493 B., Leblanc, T., Le Flochmoën, E., Lin, W., Liu, J., Liu, X., Mahieu, E., McClure-
 1494 Begley, A., Neu, J.L., Osman, M., Palm, M., Petetin, H., Petropavlovskikh, I., Querel,
 1495 R., Rappoe, N., Rozanov, A., Schultz, M.G., Schwab, J., Siddans, R., Smale, D.,
 1496 Steinbacher, M., Tanimoto, H., Tarasick, D.W., Thouret, V., Thompson, A.M.,
 1497 Trickl, T., Weatherhead, E., Wespes, C., Worden, H.M., Vigouroux, C., Xu, X.,
 1498 Zeng, G. and Ziemke, J., Tropospheric Ozone Assessment Report: Present-day
 1499 distribution and trends of tropospheric ozone relevant to climate and global
 1500 atmospheric chemistry model evaluation, Elem Sci Anth, 6(1), p.39. DOI:
 1501 10.1525/elementa.291, 2018.
- 1502 Gelaro, Ronald, et al.: The modern-era retrospective analysis for research and applications,
 1503 version 2 (MERRA-2), Journal of climate 30.14, 5419-5454, 2017.
- 1504 Ghude, S.D., Van der A, R.J., Beig, G., Fadnavis, S., Polade, S.D.: Satellite derived trends in
 1505 NO₂ over the major global hotspot regions during the past decade and their inter-
 1506 comparison. Environ. Pollut. 157, 1873–1878. [https://doi.org/10.1016/j.](https://doi.org/10.1016/j.envpol.2009.01.013)
 1507 envpol.2009.01.013, 2009.
- 1508 Glotfelty, T., Zhang, Y., Karamchandani, P., and Streets, D. G.: Will the role of
 1509 intercontinental transport change in a changing climate?, Atmos. Chem. Phys., 14,
 1510 9379–9402, <https://doi.org/10.5194/acp-14-9379-2014>, 2014.
- 1511 Gödde, M., Conrad, R. Influence of soil properties on the turnover of nitric oxide and nitrous
 1512 oxide by nitrification and denitrification at constant temperature and moisture. Biol
 1513 Fertil Soils 32, 120–128, <https://doi.org/10.1007/s003740000247>, 2000.

- 1514 Granier, C., Bessagnet, B., Bond, T., D'Angiola, A., Denier van der Gon, H., Frost, G. J., ...
 1515 & van Vuuren, D. P.: Evolution of anthropogenic and biomass burning emissions of
 1516 air pollutants at global and regional scales during the 1980–2010 period. *Climatic*
 1517 *change*, 109, 163–190, 2011.
- 1518 Grewe, V., Brunner, D., Dameris, M., Grenfell, J. L., Hein, R., Shindell, D., & Staehelin, J.:
 1519 Origin and variability of upper tropospheric nitrogen oxides and ozone at northern
 1520 mid-latitudes, *Atmos. Env.*, 35, 3421–3433, 2001.
- 1521 Griffiths, P. T., Murray, L. T., Zeng, G., Shin, Y. M., Abraham, N. L., Archibald, A. T.,
 1522 Deushi, M., Emmons, L. K., Galbally, I. E., Hassler, B., Horowitz, L. W., Keeble, J.,
 1523 Liu, J., Moeini, O., Naik, V., O'Connor, F. M., Oshima, N., Tarasick, D., Tilmes, S.,
 1524 Turnock, S. T., Wild, O., Young, P. J., and Zanis, P.: Tropospheric ozone in CMIP6
 1525 simulations, *Atmos. Chem. Phys.*, 21, 4187–4218, [https://doi.org/10.5194/acp-21-](https://doi.org/10.5194/acp-21-4187-2021)
 1526 [4187-2021](https://doi.org/10.5194/acp-21-4187-2021), 2021.
- 1527 Gulev, S.K., P.W. Thorne, J. Ahn, F.J. Dentener, C.M. Domingues, S. Gerland, D. Gong,
 1528 D.S. Kaufman, H.C. Nnamchi, J. Quaas, J.A. Rivera, S. Sathyendranath, S.L. Smith,
 1529 B. Trewin, K. von Schuckmann, and R.S. Vose: Changing State of the Climate
 1530 System. In *Climate Change 2021: The Physical Science Basis. Contribution of*
 1531 *Working Group I to the Sixth Assessment Report of the Intergovernmental Panel on*
 1532 *Climate Change* [Masson-Delmotte, V., P. Zhai, A. Pirani, S.L. Connors, C. Péan, S.
 1533 Berger, N. Caud, Y. Chen, L. Goldfarb, M.I. Gomis, M. Huang, K. Leitzell, E.
 1534 Lonnoy, J.B.R. Matthews, T.K. Maycock, T. Waterfield, O. Yelekçi, R. Yu, and B.
 1535 Zhou (eds.)]. Cambridge University Press, Cambridge, United Kingdom and New
 1536 York, NY, USA, pp. 287–422, doi: [10.1017/9781009157896.004](https://doi.org/10.1017/9781009157896.004), 2021.
- 1537 Hoor, P., Borken-Kleefeld, J., Caro, D., Dessens, O., Endresen, O., Gauss, M., Grewe, V.,
 1538 Hauglustaine, D., Isaksen, I. S. A., Jöckel, P., Lelieveld, J., Myhre, G., Meijer, E.,
 1539 Olivier, D., Prather, M., Schnadt Poberaj, C., Shine, K. P., Staehelin, J., Tang, Q., van
 1540 Aardenne, J., van Velthoven, P., and Sausen, R.: The impact of traffic emissions on
 1541 atmospheric ozone and OH: results from QUANTIFY, *Atmos. Chem. Phys.*, 9, 3113–
 1542 3136, <https://doi.org/10.5194/acp-9-3113-2009>, 2009.
- 1543 Holzworth, R. H., Brundell, J. B., McCarthy, M. P., Jacobson, A. R., Rodger, C. J., &
 1544 Anderson, T. S.: Lightning in the Arctic. *Geophysical Research Letters*, 48,
 1545 e2020GL091366, <https://doi.org/10.1029/2020GL091366>, 2021.
- 1546 Hov, Ö., Hesstvedt, E. & Isaksen, I. Long-range transport of tropospheric ozone. *Nature* **273**,
 1547 341–344. <https://doi.org/10.1038/273341a0>, 1978.
- 1548 Hubert, D., Heue, K.-P., Lambert, J.-C., Verhoelst, T., Allaart, M., Compernelle, S., Cullis,
 1549 P. D., Dehn, A., Félix, C., Johnson, B. J., Keppens, A., Kollonige, D. E., Lerot, C.,
 1550 Loyola, D., Maata, M., Mitro, S., Mohamad, M., Piters, A., Romahn, F., Selkirk, H.
 1551 B., da Silva, F. R., Stauffer, R. M., Thompson, A. M., Veeffkind, J. P., Vömel, H.,
 1552 Witte, J. C., and Zehner, C.: TROPOMI tropospheric ozone column data: geophysical
 1553 assessment and comparison to ozonesondes, GOME-2B and OMI, *Atmos Meas Tech*,
 1554 14, 7405–7433, <https://doi.org/10.5194/amt-14-7405-2021>, 2021.
- 1555 Hudman, R. C., Moore, N. E., Mebust, A. K., Martin, R. V., Russell, A. R., Valin, L. C., and
 1556 Cohen, R. C.: Steps towards a mechanistic model of global soil nitric oxide

1557 emissions: implementation and space based-constraints, *Atmos. Chem. Phys.*, 12,
1558 7779–7795, <https://doi.org/10.5194/acp-12-7779-2012>, 2012.

1559 Huntrieser, H., U. Schumann, H. Schlager, H. Höller, A. Giez, H.-D. Betz, D. Brunner, C.
1560 Forster, O. Pinto Jr., and Calheiros, R.: Lightning activity in Brazilian thunderstorms
1561 during TROCCINOX: Implications for NO_x production, *Atmos. Chem. Phys.*, 8, 21–
1562 953, 2008.

1563 Huntrieser, H., H. Schlager, M. Lichtenstern, P. Stock, T. Hamburger, H. Hoeller, K.
1564 Schmidt, H.-D. Betz, A. Ulanovsky, and Ravegnani, F.: Mesoscale convective
1565 systems observed during AMMA and their impact on the NO_x and O₃ budget over
1566 West Africa, *Atmos. Chem. Phys.*, 11, 2503–2536, [www.atmos-chem-](http://www.atmos-chem-phys.net/11/2503/2011)
1567 [phys.net/11/2503/2011](http://www.atmos-chem-phys.net/11/2503/2011), doi:10.5194/acp-11-2503-2011, 2011.

1568 Ichoku, C., & Ellison, L.: Global top-down smoke-aerosol emissions estimation using
1569 satellite fire radiative power measurements. *Atmospheric Chemistry and Physics*,
1570 14(13), 6643-6667, 2014.

1571 IPCC, AR5, chrome-
1572 extension://efaidnbmnnnibpcajpcgclefindmkaj/[https://www.ipcc.ch/site/assets/upload](https://www.ipcc.ch/site/assets/uploads/2018/03/TAR-06.pdf)
1573 [s/2018/03/TAR-06.pdf](https://www.ipcc.ch/site/assets/uploads/2018/03/TAR-06.pdf), 2018.

1574 Isaksen, I.S.A.; Berntsen, T.K.; Dalsøren, S.B.; Eleftheratos, K.; Orsolini, Y.; Rognerud, B.;
1575 Stordal, F.; Søvde, O.A.; Zerefos, C.; Holmes, C. D.: Atmospheric Ozone and
1576 Methane in a Changing Climate. *Atmosphere*, 5, 518-535.
1577 <https://doi.org/10.3390/atmos5030518>, 2014.

1578 Itahashi, S., Mathur, R., Hogrefe, C., Napelenok, S. L., and Zhang, Y.: Modeling
1579 stratospheric intrusion and trans-Pacific transport on tropospheric ozone using
1580 hemispheric CMAQ during April 2010 – Part 2: Examination of emission impacts
1581 based on the higher-order decoupled direct method, *Atmos. Chem. Phys.*, 20, 3397–
1582 3413, <https://doi.org/10.5194/acp-20-3397-2020>, 2020.

1583 Janssens-Maenhout, G., Pagliari, V., Guizzardi, D., & Muntean, M.: Global emission
1584 inventories in the emission database for global atmospheric research (EDGAR)–
1585 Manual (I). Gridding: EDGAR emissions distribution on global gridmaps,
1586 Publications Office of the European Union, Luxembourg, 775, 2013.

1587 Jin, X., Fiore, A., Boersma, K. F., Smedt, I. D., and Valin, L.: Inferring Changes in
1588 Summertime Surface Ozone–NO_x–VOC Chemistry over U.S. Urban Areas from
1589 Two Decades of Satellite and Ground-Based Observations, *Environmental Science*
1590 *Technology*, 54, 6518–6529, <https://doi.org/10.1021/acs.est.9b07785>, 2020.

1591 J. Jung, Y. Choi, S. Mousavinezhad, D. Kang, J. Park, A. Pouyaei, et al.: Changes in the
1592 ozone chemical regime over the contiguous United States inferred by the inversion of
1593 NO_x and VOC emissions using satellite observation, *Atmos. Res.*, 270, 106076,
1594 <https://doi.org/10.1016/j.atmosres.2022.106076>, 2022.

1595 Kang, D., K. Foley, R. Mathur, S. Roselle, K. Pickering, and D. Allen, Lightning NO_x
1596 Production in CMAQ Part II – Performance Evaluations, *Geosci. Model Devel.*, 12,
1597 4409–4424, <https://doi.org/10.5194/gmd-12-4409-2019>, 2019.

1598 Kaynak, B., Hu, Y., Martin, R. V., Russell, A. G., Choi, Y., & Wang, Y.: The effect of
1599 lightning NO_x production on surface ozone in the continental United States,
1600 Atmospheric Chemistry and Physics, 8, 5151–5159, 2008.

1601 Koven, C. D., Riley, W. J., Subin, Z. M., Tang, J. Y., Torn, M. S., Collins, W. D., Bonan, G.
1602 B., Lawrence, D. M., and Swenson, S. C.: The effect of vertically resolved soil
1603 biogeochemistry and alternate soil C and N models on C dynamics of CLM4,
1604 Biogeosciences, 10, 7109–7131, <https://doi.org/10.5194/bg-10-7109-2013>, 2013.

1605 Kitagawa, N.: Long-term variations in thunder-day frequencies in Japan, J. Geophys. Res.,
1606 94, 13 183–13 189, <https://doi.org/10.1029/JD094iD11p13183>, 1989.

1607 Koehler, T. L.: Cloud-to-Ground Lightning Flash Density and Thunderstorm Day
1608 Distributions over the Contiguous United States Derived from NLDN Measurements:
1609 1993–2018, Mon. Weather Rev., DOI: 10.1175/MWR-D-19-0211.1, 2020

1610 Kopacz, M., Jacob, D. J., Fisher, J. A., Logan, J. A., Zhang, L., Megretskaia, I. A., Yantosca,
1611 R. M., Singh, K., Henze, D. K., Burrows, J. P., Buchwitz, M., Khlystova, I., McMillan,
1612 W. W., Gille, J. C., Edwards, D. P., Eldering, A., Thouret, V., and Nedelec, P.: Global
1613 estimates of CO sources with high resolution by adjoint inversion of multiple satellite
1614 datasets (MOPITT, AIRS, SCIAMACHY, TES), Atmos. Chem. Phys., 10, 855–876,
1615 <https://doi.org/10.5194/acp-10-855-2010>, 2010.

1616 Koshak, W., Peterson, H., Biazar, A., Khan, M., & Wang, L.: The NASA Lightning Nitrogen
1617 Oxides Model (LNOM): application to air quality modeling. Atmospheric Research,
1618 135, 363-369, 2014.

1619 Koshak, W.J., Cummins, K.L., Buechler, D.E., Vant-Hull, B., Blakeslee, R.J., Williams,
1620 E.R. and Peterson, H.S.: Variability of CONUS lightning in 2003–12 and associated
1621 impacts. Journal of Applied Meteorology and Climatology, **54**, 15–41,
1622 <https://doi.org/10.1175/JAMC-D-14-0072.1>, 2015.

1623 Krizan, P. and Lastovicka, J.: Trends in positive and negative ozone laminae in the Northern
1624 Hemisphere, Journal of Geophysical Research: Atmospheres, 110,
1625 <https://doi.org/https://doi.org/10.1029/2004JD005477>, 2005.

1626 Labow, G. J., Ziemke, J. R., McPeters, R. D., Haffner, D. P., and Bhartia, P. K.: A total
1627 ozone-dependent ozone profile climatology based on ozonesondes and Aura MLS
1628 data, Journal of Geophysical Research: Atmospheres, 120, 2537–2545,
1629 <https://doi.org/10.1002/2014JD022634>, 2015.

1630 Labrador, L. J., Kuhlmann, R. V., and Lawrence, M. G.: The effects of lightning-produced
1631 NO_x and its vertical distribution on atmospheric chemistry: sensitivity simulations
1632 with MATCH-MPIC, Atmos. Chem. Phys., 5, 1815-1834, 2005.

1633 Lacis, A. A., Wuebbles, D. J., and Logan, J. A.: Radiative forcing of climate by changes in
1634 the vertical distribution of ozone, J. Geophys. Res., 95, 9971-9982, 1990.

1635 Lamsal, L. N, Duncan, B. N., Yoshida, Y., Krotkov, N. A., Pickering, K. E., Streets, D. G.,
1636 Zifeng Lu, Z.: U.S. NO₂ trends (2005–2013): EPA Air Quality System (AQS) data
1637 versus improved observations from the Ozone Monitoring Instrument (OMI),
1638 Atmospheric Environment, <https://doi.org/10.1016/j.atmosenv.2015.03.055>, 2015.

- 1639 Lapierre, J. L., Laughner, J. L., Geddes, J. A., Koshak, W. J., Cohen, R. C., Pusede, S. E.:
 1640 Observing U.S. regional variability in lightning NO₂ production rates, *J. Geophys.*
 1641 *Res.*, 125 (5), <https://doi.org/10.1029/2019JD031362>, 2020.
- 1642 Lavigne, T., C. Liu, and Liu, N.: How does the trend in thunder days relate to the variation of
 1643 lightning flash density? *J. Geophys. Res. Atmos.*, 124, 4955–4974,
 1644 <https://doi.org/10.1029/2018JD029920>, 2019.
- 1645 Lefohn, AS, Malley, CS, Smith, L, Wells, B, Hazucha, M, Simon, H, Naik, V, Mills, G,
 1646 Schultz, MG, Paoletti, E, De Marco, A, Xu, X, Zhang, L, Wang, T, Neufeld, HS,
 1647 Musselman, RC, Tarasick, D, Brauer, M, Feng, Z, Tang, H, Kobayashi, K, Sicard, P,
 1648 Solberg, S and Gerosa, G.: Tropospheric ozone assessment report: Global ozone
 1649 metrics for climate change, human health, and crop/ecosystem research. *Elem Sci*
 1650 *Anth*, 6: 28. DOI: 10.1525/elementa.279, 2018.
- 1651 Lelieveld, J.; Crutzen, P J.: The role of clouds in tropospheric photochemistry, 12(3), 229–
 1652 267. doi:10.1007/bf00048075, 1991.
- 1653 Liaskos, C. E., Allen, D. J., & Pickering, K. E.: Sensitivity of tropical tropospheric
 1654 composition to lightning NO_x production as determined by replay simulations with
 1655 GEOS-5, *J. Geophys. Res. Atmos.*, 120, 8512–8534, doi:[10.1002/2014JD022987](https://doi.org/10.1002/2014JD022987),
 1656 [2015](https://doi.org/10.1002/2014JD022987).
- 1657 Liu, J., Jose M. Rodriguez, Luke D. Oman, Anne R. Douglass, Mark A. Olsen, Lu
 1658 Hu, Stratospheric impact on the Northern Hemisphere winter and spring ozone
 1659 interannual variability in the troposphere, *Atmospheric Chemistry and Physics*,
 1660 10.5194/acp-20-6417-2020, **20**, 11, 6417-6433, 2020.
- 1661 Liu, X., Tai, A. P. K., and Fung, K. M.: Responses of surface ozone to future agricultural
 1662 ammonia emissions and subsequent nitrogen deposition through terrestrial ecosystem
 1663 changes, *Atmos. Chem. Phys.*, 21, 17743–17758, [https://doi.org/10.5194/acp-21-](https://doi.org/10.5194/acp-21-17743-2021)
 1664 [17743-2021](https://doi.org/10.5194/acp-21-17743-2021), 2021.
- 1665 Liu, J., Strode, S. A., Liang, Q., Oman, L.D., Colarco, P. R., Fleming, E. L., et al. (2022).
 1666 Change in tropospheric ozone in the recent decades and its contribution to global total
 1667 ozone. *Journal of Geophysical Research: Atmospheres*, 127, e2022JD037170.
 1668 <https://doi.org/10.1029/2022JD037170>, 2022.
- 1669 Li et al. Jianjun Qiu, Ligang Wang, Yang, L.: Advance in a terrestrial biogeochemical
 1670 model—DNDC model, *Acta Ecologica Sinica*, 31, 2,
 1671 <https://doi.org/10.1016/j.chnaes.2010.11.006>, 2011.
- 1672 Luecken, D. J.; Napelenok, S. L.; Strum, M.; Scheffe, R.; Phillips, S.: Sensitivity of ambient
 1673 atmospheric formaldehyde and ozone to precursor species and source types across the
 1674 united states, *Environ. Sci. Technol.*, 52, 4668– 4675, DOI: 10.1021/acs.est.7b05509,
 1675 2018
- 1676 Marais, E. A., Jacob, D. J., Kurosu, T. P., Chance, K., Murphy, J. G., Reeves, C., Mills, G.,
 1677 Casadio, S., Millet, D. B., Barkley, M. P., Paulot, F., and Mao, J.: Isoprene emissions
 1678 in Africa inferred from OMI observations of formaldehyde columns, *Atmos. Chem.*
 1679 *Phys.*, 12, 6219–6235, <https://doi.org/10.5194/acp-12-6219-2012>, 2012.
- 1680 Marais, E. A., Jacob, D. J., Choi, S., Joiner, J., Belmonte-Rivas, M., Cohen, R. C., et al.:
 1681 Nitrogen oxides in the global upper troposphere: interpreting cloud-sliced NO₂

1682 observations from the OMI satellite instrument, Atmospheric Chemistry and Physics,
1683 <https://doi.org/10.5194/acp-18-17017-2018>, 2018

1684 Martin, R. V., Sauvage, B., Folkins, I., Sioris, C. E., Boone, Bernath, C. P., & Ziemke, J.:
1685 Space-based constraints on the production of nitric oxide by lightning, J. Geophys.
1686 Res., 112, D09309, doi:10.1029/2006JD007831, 2007.

1687 Matandirotya, N.R., Burger, R. An assessment of NO₂ atmospheric air pollution over three
1688 cities in South Africa during 2020 COVID-19 pandemic. Air Qual Atmos Health **16**,
1689 263–276, <https://doi.org/10.1007/s11869-022-01271-3>, 2023.

1690 McDuffie, E. E., Smith, S. J., O'Rourke, P., Tibrewal, K., Venkataraman, C., Marais, E. A.,
1691 Zheng, B., Crippa, M., Brauer, M., and Martin, R. V.: A global anthropogenic emission
1692 inventory of atmospheric pollutants from sector- and fuel-specific sources (1970–
1693 2017): an application of the Community Emissions Data System (CEDS), Earth Syst.
1694 Sci. Data, 12, 3413–3442, <https://doi.org/10.5194/essd-12-3413-2020>, 2020.

1695 Meng, L., Liu, J., Tarasick, D. W., Randel, W. J., Steiner, A. K., Wilhelmssen, H., Wang, L.,
1696 and Haimberger, L.: Continuous rise of the tropopause in the Northern Hemisphere
1697 over 1980–2020. Science Advances, <https://doi.org/10.1126/sciadv.abi8065>, 2021.

1698 Mills G, Pleijel H, Malley CS, Sinha B, Cooper OR, Schultz MG, Neufeld HS, Simpson D,
1699 Sharps K, Feng Z, Gerosa G, Harmens H, Kobayashi K, Saxena P, Paoletti E, Sinha
1700 V, Xu X., [Tropospheric Ozone Assessment Report: Present-day tropospheric ozone
1701 distribution and trends relevant to vegetation](#). Elem Sci Anth.,6(1):47. DOI:
1702 10.1525/elementa.302, 2018.

1703 Miyazaki, K., H. J. Eskes, K. Sudo, and Zhang, C.: Global lightning NO_x production
1704 estimated by an assimilation of multiple satellite data sets, Atmos. Chem Phys., 14,
1705 3277–3305, doi:10.5194/acp-14-3277-2014, 2014.

1706 Miyazaki, K., Bowman, K., Sekiya, T., Eskes, H., Boersma, F., Worden, H., Livesey, N.,
1707 Payne, V. H., Sudo, K., Kanaya, Y., Takigawa, M., and Ogochi, K.: Updated
1708 tropospheric chemistry reanalysis and emission estimates, TCR-2, for 2005–2018,
1709 Earth Syst. Sci. Data, 12, 2223–2259, <https://doi.org/10.5194/essd-12-2223-2020>,
1710 2020.

1711 McPeters, R. D. and Labow, G. J.: Climatology 2011: An MLS and sonde derived ozone
1712 climatology for satellite retrieval algorithms, Journal of Geophysical Research:
1713 Atmospheres, 117, n/a-n/a, <https://doi.org/10.1029/2011JD017006>, 2012.

1714 Molod, A., Takacs, L., Suarez, M., and Bacmeister, J.: Development of the GEOS-5
1715 atmospheric general circulation model: evolution from MERRA to MERRA2,
1716 Geosci. Model Dev., 8, 1339–1356, <https://doi.org/10.5194/gmd-8-1339-2015>, 2015.

1717 Murray, L.T.: An uncertain future for lightning. Nature Clim Change **8**, 191–192,
1718 <https://doi.org/10.1038/s41558-018-0094-0>, 2018.

1719 Murray, L. T.: Lightning NO_x and Impacts on Air Quality, Curr Pollution Rep (2016) 2:115–
1720 133, DOI 10.1007/s40726-016-0031-7, 2016

1721 Murray, L. T., D. J. Jacob, J. A. Logan, R. C. Hudman, and J. Koshak, W.: Optimized
1722 regional and interannual variability of lightning in a global chemical transport model
1723 constrained by LIS/OTD satellite data, J. Geophys. Res., 117, D20307,
1724 doi:[10.1029/2012JD017934](https://doi.org/10.1029/2012JD017934), 2012.

- 1725 Nault, B. A., Garland, C., Wooldridge, J. L., Brune, W. H., Campuzano-Jost, P., Crouse, J.
1726 D., et al.: Observational Constraints on the Oxidation of NO_x in the Upper
1727 Troposphere, *The Journal of Physical Chemistry A*, 120 (9), 1468-1478, doi:
1728 10.1021/acs.jpca.5b07824, 2016.
- 1729 Nault, B. A., Laughner, J. L., Wooldridge, P. J., Crouse, J. D., Dibb, J., Diskin, et al.:
1730 Lightning NO_x emissions: reconciling measured and modeled estimates with updated
1731 NO_x chemistry. *Geophysical Research Letters*, 44, 9479–9488, 2017.
- 1732 Newton, R., Vaughan, G., Ricketts, H. M. A., Pan, L. L., Weinheimer, A. J., and Chemel, C.:
1733 Ozonesonde profiles from the West Pacific Warm Pool: measurements and
1734 validation, *Atmos Chem Phys*, 16, 619–634, [https://doi.org/10.5194/acp-16-619-](https://doi.org/10.5194/acp-16-619-2016)
1735 2016, 2016.
- 1736 Nielsen, J. Eric, et al. "Chemical mechanisms and their applications in the Goddard Earth
1737 Observing System (GEOS) earth system model." *Journal of Advances in Modeling*
1738 *Earth Systems* 9.8, 3019-3044, 2017.
- 1739 NOAA, https://gml.noaa.gov/ccgg/trends_ch4/, 2024. Last visited: August 2nd, 2024.
- 1740 Nussbaumer, C. M., Fischer, H., Lelieveld, J., and Pozzer, A.: What controls ozone
1741 sensitivity in the upper tropical troposphere?, *Atmos. Chem. Phys.*, 23, 12651–12669,
1742 <https://doi.org/10.5194/acp-23-12651-2023>, 2023.
- 1743 Oleribe OO, Suliman AAA, Taylor-Robinson SD, Corrah T. Possible Reasons Why Sub-
1744 Saharan Africa Experienced a Less Severe COVID-19 Pandemic in 2020. *J*
1745 *Multidiscip Healthc.* 2021;14:3267-3271, <https://doi.org/10.2147/JMDH.S331847>,
1746 2021.
- 1747 Oltmans, SJ, Lefohn, AS, Shadwick, D, Harris, JM, Scheel, HE, et al.: Recent tropospheric
1748 ozone changes — A pattern dominated by slow or no growth, *Atmos. Environ*, 2013.
- 1749 Orbe, C., Oman, L. D., Strahan, S. E., Waugh, D. W., Pawson, S., Takacs, L. L., and Molod,
1750 A. M.: Large-scale atmospheric transport in GEOS replay simulations. *Journal of*
1751 *Advances in Modeling Earth Systems*, 9, 2545–2560.
1752 <https://doi.org/10.1002/2017MS001053>, 2017.
- 1753 Ott, L. E., K. E. Pickering, G. L. Stenchikov, H. Huntrieser, and Schumann, U.: Effects of
1754 lightning NO_x production during the 21 July European Lightning Nitrogen Oxides
1755 Project storm studied with a three-dimensional cloud-scale chemical transport model,
1756 *J. Geophys. Res.*, 112, D05307, doi:10.1029/2006JD007365, 2007.
- 1757 Ott, L. E., K. E. Pickering, G. L. Stenchikov, D. J. Allen, A. J. DeCaria, B. Ridley, R.-F. Lin,
1758 S. Lang, and Tao, W.-K.: Production of lightning NO_x and its vertical distribution
1759 calculated from three-dimensional cloud-scale chemical transport model simulations,
1760 *J. Geophys. Res.*, 115, D04301,doi:10.1029/2009JD011880, 2010.
- 1761 Philipona, R., C. Mears, M. Fujiwara, P. Jeannot, P. Thorne, G. Bodeker, L. Haimberger, M.
1762 Hervo, C. Popp, G. Romanens, W. Steinbrecht, R. Stubi, R. Van Malderen,
1763 adiosondes show that after decades of cooling, the lower stratosphere is now
1764 warming. *J. Geophys. Res. Atmos.* 123, 12509–12522, 2018.
- 1765 Pickering, K. E, A. M. Thompson, R. R. Dickerson, W. T. Luke, D. P. McNamara, J. P.
1766 Greenberg, and R. Zimmerman, P.: Model calculations of tropospheric ozone

- 1767 production potential following observed convective events, *J. Geophys. Res.*,
1768 95:14,049-14,062, 1990.
- 1769 Pickering, K. E., Y. Wang, W.-K. Tao, C. Price, and Mueller, J.-F.: Vertical distributions of
1770 lightning NO_x for use in regional and global chemical transport models, *J. Geophys.*
1771 *Res.*, 103: 31,203-31,216, 1998.
- 1772 Pickering, K. E., E. Bucsela, D. Allen, A. Ring, R. Holzworth, and Krotkov, N.: Estimates of
1773 lightning NO_x production based on OMI NO₂ observations over the Gulf of Mexico,
1774 *J. Geophys. Res. Atmos.*, 121, doi:[10.1002/2015JD024179](https://doi.org/10.1002/2015JD024179), 2016.
- 1775 Pickering, K., Y. Li, K. A. Cummings, M. Brock, D. Allen, E. C. Bruning, and B. Pollack, I.:
1776 Lightning NO_x in the 29–30 May 2012 Deep Convective Clouds and Chemistry
1777 (DC3) Severe Storm and Its Downwind Chemical Consequences, *J. Geophys. Res.*,
1778 129, e2023JD039439., doi:10.1029/2023JD039439, 2024.
- 1779 Pinto, O., Jr., K. P. Naccarato, and R. C. A. Pinto, I.: Thunderstorm incidence in southeastern
1780 Brazil estimated from different data sources. *Ann. Geophys.*, 31, 1213–1219,
1781 <https://doi.org/10.5194/angeo-31-1213-2013>, 2013.
- 1782 Prodromos Zanis, Dimitris Akritidis, Steven Turnock, Vaishali Naik, Sophie
1783 Szopa, Aristeidis K Georgoulas, Susanne E Bauer, Makoto Deushi, Larry W
1784 Horowitz, James Keeble, Climate change penalty and benefit on surface ozone: a
1785 global perspective based on CMIP6 earth system models, *Environmental Research*
1786 *Letters*, 17, 2, DOI: <https://doi.org/10.1088/1748-9326/ac4a34>, 2022.
- 1787 Pollack, I. B., C. R. Homeyer, T. B. Ryerson, K. C. Aikin, J. Peischl, E. C. Apel, T. Campos,
1788 F. Flocke, R. S. Hornbrook, D. J. Knapp, et al.: Airborne quantification of upper
1789 tropospheric NO_x production from lightning in deep convective storms over the
1790 United States Great Plains, *J. Geophys. Res. Atmos.*, 121, 2002–2028,
1791 doi:[10.1002/2015JD023941](https://doi.org/10.1002/2015JD023941), 2016.
- 1792 Prather, M. J. and J. Jacob, D.: A persistent imbalance in HO_x and NO_x photochemistry of the
1793 upper troposphere driven by deep tropical convection, *Geophys. Res. Lett.*, 24, 3189
1794 – 3192, 1997.
- 1795 Price, C., J. Penner, and Prather, M.: NO_x from lightning 1. Global distribution based on
1796 lightning physics, *J. Geophys. Res.*, 102 (D5), 5929-5941, 1997.
- 1797 Price, C. G.: Lightning Applications in Weather and Climate Research, *Surv. Geophys.*
1798 (2013) 34:755–767, DOI 10.1007/s10712-012-9218-7, 2013.
- 1799 Putero, D., Cristofanelli, P., Chang, K.-L., Dufour, G., Beachley, G., Couret, C., Effertz, P.,
1800 Jaffe, D. A., Kubistin, D., Lynch, J., Petropavlovskikh, I., Puchalski, M., Sharac, T.,
1801 Sive, B. C., Steinbacher, M., Torres, C., and Cooper, O. R.: Fingerprints of the
1802 COVID-19 economic downturn and recovery on ozone anomalies at high-elevation
1803 sites in North America and western Europe, *Atmos. Chem. Phys.*, 23, 15693–15709,
1804 <https://doi.org/10.5194/acp-23-15693-2023>, 2023.
- 1805 Qie, K., Qie, X., & Tian, W.: Increasing trend of lightning activity in the South Asian region,
1806 *Science Bulletin*, 66 (1), 78-84, 2021.
- 1807 Qie, K., Tian, W., Wang, W., Wu, X., Yuan, T., Tian, H., Luo, J., Zhang, R., & Want, T.
1808 Regional trends of lightning activity in the tropics and subtropics, *Atmos. Res.*, 242,
1809 Article 104960, [10.1016/j.atmosres.2020.104960](https://doi.org/10.1016/j.atmosres.2020.104960), 2020.

1810 Randel, W. J., L. Polvani, F. Wu, D. E. Kinnison, C.-Z. Zou, C. Mears, Troposphere
1811 stratosphere temperature trends derived from satellite data compared with ensemble
1812 simulations from WACCM. *J. Geophys. Res. Atmos.* 122, 9651–9667, 2017.

1813 Ravetta, F., G. Ancellet, A. Colette, and H. Schlager, H.: Long-range transport and
1814 tropospheric ozone variability in the western Mediterranean region during the
1815 Intercontinental Transport of Ozone and Precursors (ITOP-2004) campaign, *J.*
1816 *Geophys. Res.*, 112, D10S46, doi:[10.1029/2006JD007724](https://doi.org/10.1029/2006JD007724), 2007.

1817 Ren, X., J. R. Olson, J. H. Crawford, W. H. Brune, J. Mao, R. B. Long, G. Chen, M. A.
1818 Avery, G. W. Sachse, J. D. Barrick, G. S. Diskin, L. G. Huey, Alan Fried, Ronald C.
1819 Cohen, Brian Heikes, Paul Wennberg, Hanwant B. Singh, Donald R. Blake, E.
1820 Shetter, R.: HO_x Chemistry during INTEX–A 2004: Observation, Model Calculations
1821 and comparison with previous studies, *J. Geophys. Res.*, 113, D05310,
1822 doi:10.1029/2007JD009166, 2008.

1823 Ridley, B., Ott, L., Pickering, K., Emmons, L., Montzka, D., Weinheimer, A., et al.: Florida
1824 thunderstorms: A faucet of reactive nitrogen to the upper troposphere, *J. Geophys.*
1825 *Res.*, 109 (D17), 10.1029/2004JD004769, 2004.

1826 Romps, D. M., Seeley, J. T., Vollaro, D., & Molinar, J.: Projected increase in lightning
1827 strikes in the United States due to global warming, *Science*, 851-854, 2014.

1828 Romps, D. M., Charn, A. B., Holzworth, R. H., Lawrence, W. E., Molinari, J., & Vollaro, D.:
1829 CAPE times P explains lightning over land but not the land-ocean contrast.
1830 *Geophysical Research Letters*, 45, 12,623–12,630,
1831 <https://doi.org/10.1029/2018GL080267>, 2018.

1832 Romps, D. M.: Evaluating the future of lightning in cloud-resolving models. *Geophysical*
1833 *Research Letters*, 46, <https://doi.org/10.1029/2019GL085748>, 2019.

1834 Sanap, S. D.: Global and regional variations in aerosol loading during COVID-19
1835 imposed lockdown, *Atmos. Environ.*, 246, <https://doi.org/10.1016/j.atmosenv.2020.118132>,
1836 2021

1837 Sauvage, B., R. V. Martin, A. van Donkelaar, and R. Ziemke, J.: Quantification of the
1838 factors controlling tropical tropospheric ozone and the South Atlantic maximum, *J.*
1839 *Geophys. Res.*, 112, D11309, doi:10.1029/2006JD008008, 2007.

1840 Saunio, M., R. Stavert, A., Poulter, B., Bousquet, P., G. Canadell, J., B. Jackson, R., A.
1841 Raymond, P., J. Dlugokencky, E., Houweling, S., K. Patra, P., Ciais, P., K. Arora, V.,
1842 Bastviken, D., Bergamaschi, P., R. Blake, D., Brailsford, G., Bruhwiler, L., M.
1843 Carlson, K., Carrol, M., Castaldi, S., Chandra, N., Crevoisier, C., M. Crill, P., Covey,
1844 K., L. Curry, C., Etiope, G., Frankenberg, C., Gedney, N., I. Hegglin, M., Höglund-
1845 Isaksson, L., Hugelius, G., Ishizawa, M., Ito, A., Janssens-Maenhout, G., M. Jensen,
1846 K., Joos, F., Kleinen, T., B. Krummel, P., L. Langenfelds, R., G. Laruelle, G., Liu, L.,
1847 MacHida, T., Maksyutov, S., C. McDonald, K., McNorton, J., A. Miller, P., R.
1848 Melton, J., Morino, I., Müller, J., Murguia-Flores, F., Naik, V., Niwa, Y., Noce, S.,
1849 O’Doherty, S., J. Parker, R., Peng, C., Peng, S., P. Peters, G., Prigent, C., Prinn, R.,
1850 Ramonet, M., Regnier, P., J. Riley, W., A. Rosentreter, J., Segers, A., J. Simpson, I.,
1851 Shi, H., J. Smith, S., Paul Steele, L., F. Thornton, B., Tian, H., Tohjima, Y., N.
1852 Tubiello, F., Tsuruta, A., Viovy, N., Voulgarakis, A., S. Weber, T., Van Weele, M.,
1853 R. Van Der Werf, G., F. Weiss, R., Worthy, D., Wunch, D., Yin, Y., Yoshida, Y.,

- 1854 Zhang, W., Zhang, Z., Zhao, Y., Zheng, B., Zhu, Q., Zhu, Q., and Zhuang, Q.: The
 1855 global methane budget 2000-2017, *Earth Syst Sci Data*, 12,
 1856 <https://doi.org/10.5194/essd-12-1561-2020>, 2020.
- 1857 Schumann, U., and Huntrieser, H.: The global lightning-induced nitrogen oxides source,
 1858 *Atmos. Chem. Phys.*, 7, 3823-3907, 2007.
- 1859 Seguel, R. J., Castillo, L., Opazo, C., Rojas, N. Y., Nogueira, T., Cazorla, M., Gavidia-
 1860 Calderón, M., Gallardo, L., Garreaud, R., Carrasco-Escaff, T., and Elshorbany, Y.:
 1861 Changes in South American Surface Ozone Trends: Exploring the Influences of
 1862 Precursors and Extreme Events, *EGUsphere* [preprint],
 1863 <https://doi.org/10.5194/egusphere-2024-328>, 2024.
- 1864 Sen, P.: Estimated of the regression coefficient based on Kendall's Tau. *J Am Stat Assoc*
 1865 39:1379-1389, 1968.
- 1866 Shi, Z., H. Wang, Y. Tan, L. Li, Li, C.: Influence of aerosols on lightning activities in central
 1867 eastern parts of China, *Atmos Sci Lett.*, 21:e957, <https://doi.org/10.1002/asl.957>,
 1868 2020.
- 1869 Sokhi, R. S., Singh, V., Querol, X., Finardi, S., Targino, A. C., Andrade, M. de F., Pavlovic,
 1870 R., Garland, R. M., Massagué, J., Kong, S., Baklanov, A., Ren, L., Tarasova, O.,
 1871 Carmichael, G., Peuch, V. H., Anand, V., Arbilla, G., Badali, K., Beig, G.,
 1872 Belalcazar, L. C., Bolignano, A., Brimblecombe, P., Camacho, P., Casallas, A.,
 1873 Charland, J. P., Choi, J., Chourdakis, E., Coll, I., Collins, M., Cyrus, J., da Silva, C.
 1874 M., Di Giosa, A. D., Di Leo, A., Ferro, C., Gavidia-Calderon, M., Gayen, A.,
 1875 Ginzburg, A., Godefroy, F., Gonzalez, Y. A., Guevara-Luna, M., Haque, S. M.,
 1876 Havenga, H., Herod, D., Hörrak, U., Hussein, T., Ibarra, S., Jaimes, M., Kaasik, M.,
 1877 Khaiwal, R., Kim, J., Kousa, A., Kukkonen, J., Kulmala, M., Kuula, J., La Violette,
 1878 N., Lanzani, G., Liu, X., MacDougall, S., Manseau, P. M., Marchegiani, G.,
 1879 McDonald, B., Mishra, S. V., Molina, L. T., Mooibroek, D., Mor, S., Moussiopoulos,
 1880 N., Murena, F., Niemi, J. V., Noe, S., Nogueira, T., Norman, M., Pérez-Camaño, J.
 1881 L., Petäjä, T., Piketh, S., Rathod, A., Reid, K., Retama, A., Rivera, O., Rojas, N. Y.,
 1882 Rojas-Quincho, J. P., San José, R., Sánchez, O., Seguel, R. J., Sillanpää, S., Su, Y.,
 1883 Tapper, N., Terrazas, A., Timonen, H., Toscano, D., Tsegas, G., Velders, G. J. M.,
 1884 Vlachokostas, C., von Schneidmesser, E., VPM, R., Yadav, R., Zalakeviciute, R.,
 1885 and Zavala, M.: A global observational analysis to understand changes in air quality
 1886 during exceptionally low anthropogenic emission conditions, *Environ Int*, 157,
 1887 <https://doi.org/10.1016/j.envint.2021.106818>, 2021.
- 1888 Souri, A. H., Johnson, M. S., Wolfe, G. M., Crawford, J. H., Fried, A., Wisthaler, A., Brune,
 1889 W. H., Blake, D. R., Weinheimer, A. J., Verhoelst, T., Compernelle, S., Pinardi, G.,
 1890 Vigouroux, C., Langerock, B., Choi, S., Lamsal, L., Zhu, L., Sun, S., Cohen, R. C.,
 1891 Min, K.-E., Cho, C., Philip, S., Liu, X., and Chance, K.: Characterization of errors in
 1892 satellite-based HCHONO₂ tropospheric column ratios with respect to chemistry,
 1893 column-to-PBL translation, spatial representation, and retrieval uncertainties,
 1894 *Atmospheric Chemistry and Physics*, 23, 1963–1986, [https://doi.org/10.5194/acp-23-](https://doi.org/10.5194/acp-23-1963-2023)
 1895 1963-2023, 2023.
- 1896 Stauffer, R. M., Thompson, A. M., Kollonige, D., Tarasick, D., Van Malderen, R., Smit, H.
 1897 G. J., Vömel, H., Morris, G., Johnson, B. J., Cullis, P., and et al.: An Examination of

- 1898 the Recent Stability of Ozone Global Network Data, Earth and Space Science
1899 Open Archive, 48, <https://doi.org/10.1002/essoar.10511590.1>, 2022.
- 1900 Steinbrecht, W., Claude, H., Köhler, U., and Hoinka, K. P.: Correlations between tropopause
1901 height and total ozone: Implications for long-term changes, *J. Geophys. Res.*, 103,
1902 19183–19192, <https://doi.org/10.1029/98JD01929>, 1998.
- 1903 Steinbrecht, W., Kubistin, D., Plass-Dülmer, C., Davies, J., Tarasick, D. W., von der
1904 Gathen, P., et al.: COVID-19 crisis reduces free tropospheric ozone across the Northern
1905 Hemisphere. *Geophysical Research Letters*, 48, e2020GL091987.
1906 <https://doi.org/10.1029/2020GL091987>, 2021
- 1907 Steiner, A. K., F. Ladst. dter, W. J. Randel, A. C. Maycock, Q. Fu, C. Claud, H. Gleisner, L.
1908 Haimberger, S. -P. Ho, P. Keckhut, T. Leblanc, C. Mears, L. M. Polvani, B. D.
1909 Santer, T. Schmidt, V. Sofieva, R. Wing, C. -Z. Zou, Observed temperature changes
1910 in the troposphere and stratosphere from 1979 to 2018. *J. Climate* 33, 8165–8194,
1911 2020.
- 1912 Stohl, A., Bonasoni, P., Cristofanelli, P., Collins, W., Feichter, J., Frank, A., Forster, C.,
1913 Gerasopoulos, E., Gäggeler, H., James, P., Kentarchos, T., Kromp-Kolb, H., Krüger,
1914 B., Land, C., Meloen, J., Papayannis, A., Priller, A., Seibert, P., Sprenger, M.,
1915 Roelofs, G. J., Scheel, H. E., Schnabel, C., Siegmund, P., Tobler, L., Trickl, T.,
1916 Wernli, H., Wirth, V., Zanis, P., and Zerefos, C.: Stratosphere-troposphere exchange:
1917 A review, and what we have learned from STACCATO, *J. Geophys. Res.*, 108, 8516,
1918 <https://doi.org/10.1029/2002JD002490>, 2003.
- 1919 Strahan, S. E., Duncan, B. N., and Hoor, P.: Observationally derived transport diagnostics for
1920 the lowermost stratosphere and their application to the GMI chemistry and transport
1921 model. *Atmospheric Chemistry and Physics*, 7(9), 2435–2445.
1922 <https://doi.org/10.5194/acp-7-2435-2007>, 2007.
- 1923 Schultz, M.G., Schröder, S., Lyapina, O., Cooper, O., Galbally, I., Petropavlovskikh, I., von
1924 Schneidmesser, E., Tanimoto, H., Elshorbany, Y., Naja, M., Seguel, R., Dauert, U.,
1925 Eckhardt, P., Feigenspahn, S., Fiebig, M., Hjellbrekke, A.-G., Hong, Y.-D., Christian
1926 Kjeld, P., Koide, H., Lear, G., Tarasick, D., Ueno, M., Wallasch, M., Baumgardner,
1927 D., Chuang, M.-T., Gillett, R., Lee, M., Molloy, S., Moolla, R., Wang, T., Sharps, K.,
1928 Adame, J.A., Ancellet, G., Apadula, F., Artaxo, P., Barlasina, M., Bogucka, M.,
1929 Bonasoni, P., Chang, L., Colomb, A., Cuevas, E., Cupeiro, M., Degorska, A., Ding,
1930 A., Fröhlich, M., Frolova, M., Gadhavi, H., Gheusi, F., Gilge, S., Gonzalez, M.Y.,
1931 Gros, V., Hamad, S.H., Helmig, D., Henriques, D., Hermansen, O., Holla, R., Huber,
1932 J., Im, U., Jaffe, D.A., Komala, N., Kubistin, D., Lam, K.-S., Laurila, T., Lee, H.,
1933 Levy, I., Mazzoleni, C., Mazzoleni, L., McClure-Begley, A., Mohamad, M., Murovic,
1934 M., Navarro-Comas, M., Nicodim, F., Parrish, D., Read, K.A., Reid, N., Ries, L.,
1935 Saxena, P., Schwab, J.J., Scorgie, Y., Senik, I., Simmonds, P., Sinha, V., Skorokhod,
1936 A., Spain, G., Spangl, W., Spoor, R., Springston, S.R., Steer, K., Steinbacher, M.,
1937 Suharguniyawan, E., Torre, P., Trickl, T., Weili, L., Weller, R., Xu, X., Xue, L. and
1938 Zhiqiang, M., Tropospheric Ozone Assessment Report: Database and Metrics Data of
1939 Global Surface Ozone Observations, *Elem Sci Anth*, 5, p.58. DOI:
1940 10.1525/elementa.244, 2017.
- 1941 Szopa, S., Naik, V., Adhikary, B., Artaxo, P., Berntsen, T., Collins, W.D., Fuzzi, S.,
1942 Gallardo, L., Kiendler-Scharr, A., Klimont, Z., Liao, H., Unger, N., and Zanis, P.:

- 1943 Short-Lived Climate Forcers. In *Climate Change 2021: The Physical Science Basis*.
 1944 Contribution of Working Group I to the Sixth Assessment Report of the
 1945 Intergovernmental Panel on Climate Change [Masson-Delmotte, V., P. Zhai,
 1946 A. Pirani, S.L. Connors, C. Péan, S. Berger, N. Caud, Y. Chen, L. Goldfarb,
 1947 M.I. Gomis, M. Huang, K. Leitzell, E. Lonnoy, J.B.R. Matthews, T.K. Maycock,
 1948 T. Waterfield, O. Yelekçi, R. Yu, and B. Zhou (eds.)]. Cambridge University Press,
 1949 Cambridge, United Kingdom and New York, NY, USA, pp. 817–922,
 1950 doi:[10.1017/9781009157896.008](https://doi.org/10.1017/9781009157896.008), 2021.
- 1951 Tarasick, D., Galbally, I.E., Cooper, O.R., Schultz, M.G., Ancellet, G., Leblanc, T.,
 1952 Wallington, T.J., Ziemke, J., Liu, X., Steinbacher, M., Staehelin, J., Vigouroux, C.,
 1953 Hannigan, J.W., García, O., Foret, G., Zanis, P., Weatherhead, E., Petropavlovskikh,
 1954 I., Worden, H., Osman, M., Liu, J., Chang, K.-L., Gaudel, A., Lin, M., Granados-
 1955 Muñoz, M., Thompson, A.M., Oltmans, S.J., Cuesta, J., Dufour, G., Thouret, V.,
 1956 Hassler, B., Trickl, T. and Neu, J.L., 2019. Tropospheric Ozone Assessment Report:
 1957 Tropospheric ozone from 1877 to 2016, observed levels, trends and uncertainties.
 1958 Tropospheric Ozone Assessment Report: Tropospheric ozone from 1877 to 2016,
 1959 observed levels, trends and uncertainties. *Elem Sci Anth*, 7(1), p.39. DOI :
 1960 [10.1525/elementa.376](https://doi.org/10.1525/elementa.376), 2019.
- 1961 Thompson, A. M., Witte, J. C., Sterling, C., Jordan, A., Johnson, B. J., Oltmans, S. J.,
 1962 Fujiwara, M., Vömel, H., Allaart, M., PETERS, A., Coetzee, G. J. R., Posny, F.,
 1963 Corrales, E., Diaz, J. A., Félix, C., Komala, N., Lai, N., Ahn Nguyen, H. T., Maata,
 1964 M., Mani, F., Zainal, Z., Ogino, S., Paredes, F., Penha, T. L. B., Silva, F. R., Sallons-
 1965 Mitro, S., Selkirk, H. B., Schmidlin, F. J., Stübi, R., and Thiongo, K.: First
 1966 Reprocessing of Southern Hemisphere Additional Ozonesondes (SHADOZ) Ozone
 1967 Profiles (1998–2016): 2. Comparisons With Satellites and Ground-Based Instruments,
 1968 *Journal of Geophysical Research: Atmospheres*, 122,
 1969 <https://doi.org/10.1002/2017JD027406>, 2017.
- 1970 Tsvilidou, M., Sauvage, B., Bennouna, Y., Blot, R., Boulanger, D., Clark, H., Le Flochmoën,
 1971 E., Nédélec, P., Thouret, V., Wolff, P., and Barret, B.: Tropical tropospheric ozone
 1972 and carbon monoxide distributions: characteristics, origins, and control factors, as
 1973 seen by IAGOS and IASI, *Atmos. Chem. Phys.*, 23, 14039–14063,
 1974 <https://doi.org/10.5194/acp-23-14039-2023>, 2023.
- 1975 Turnock, S. T., Allen, R. J., Andrews, M., Bauer, S. E., Deushi, M., Emmons, L., Good, P.,
 1976 Horowitz, L., John, J. G., Michou, M., Nabat, P., Naik, V., Neubauer, D., O'Connor,
 1977 F. M., Olivié, D., Oshima, N., Schulz, M., Sellar, A., Shim, S., Takemura, T., Tilmes,
 1978 S., Tsigaridis, K., Wu, T., and Zhang, J.: Historical and future changes in air
 1979 pollutants from CMIP6 models, *Atmos. Chem. Phys.*, 20, 14547–14579,
 1980 <https://doi.org/10.5194/acp-20-14547-2020>, 2020.
- 1981 Theil, H.: A rank-invariant method of linear and polynomial regression analysis. I, II, III”,
 1982 *Nederl. Akad. Wetensch., Proc.*, 53: 386–392, 521–525, 1397–1412, 1950.
- 1983 Trickl, T., Bärtsch-Ritter, N., Eisele, H., Furger, M., Mücke, R., Sprenger, M., and Stohl, A.:
 1984 High-ozone layers in the middle and upper troposphere above Central Europe:
 1985 potential import from the stratosphere along the subtropical jet stream, *Atmos. Chem.*
 1986 *Phys.*, 11, 9343–9366, <https://doi.org/10.5194/acp-11-9343-2011>, 2011.

- 1987 Verma, S., Yadava, P. K., Lal, D. M., Mall, R. K., Harshbardhan, K., & Payra, S.: Role of
 1988 Lightning NO_x in ozone formation: A review, *Pure and Applied Geophysics*, 178,
 1989 1425-1443, 2021.
- 1990 Wang, H., Shi, Z., Wang, X., Tan, Y., Wang, H., Li, L., & Lin, X.: Cloud-to-Ground
 1991 Lightning Response to Aerosol over Air-Polluted Urban Areas in China. *Remote*
 1992 *Sens.* 13, 2600. <https://doi.org/10.3390/rs13132600>, 2021
- 1993 Wang, H., Lu, X., Jacob, D. J., Cooper, O. R., Chang, K.-L., Li, K., Gao, M., Liu, Y., Sheng,
 1994 B., Wu, K., Wu, T., Zhang, J., Sauvage, B., Nédélec, P., Blot, R., and Fan, S.: Global
 1995 tropospheric ozone trends, attributions, and radiative impacts in 1995–2017: an
 1996 integrated analysis using aircraft (IAGOS) observations, ozonesonde, and multi-
 1997 decadal chemical model simulations, *Atmos Chem Phys*, 22, 13753–13782,
 1998 <https://doi.org/10.5194/acp-22-13753-2022>, 2022.
- 1999 Wang, Y., A. W. DeSilva, G. C. Goldenbaum, and R Dickerson, R.: Nitric oxide production
 2000 by simulated lightning: Dependence on current, energy, and pressure, *J. Geophys.*
 2001 *Res.*, 103, 19,149-19,159, 1998.
- 2002 Wilcox, R.: *Fundamentals of Modern Statistical Methods: Substantially Improving Power*
 2003 *and Accuracy.* Springer Science and Business Media, 2001.
- 2004 Williams, R. S., Hegglin, M. I., Kerridge, B. J., Jöckel, P., Latter, B. G., and Plummer, D. A.:
 2005 Characterising the seasonal and geographical variability in tropospheric ozone,
 2006 stratospheric influence and recent changes, *Atmos. Chem. Phys.*, 19, 3589–3620,
 2007 <https://doi.org/10.5194/acp-19-3589-2019>, 2019.
- 2008 Wu, D., Zhang, J., Wang, M., An, J., Wang, R., Haider, H., et al.: Global and regional
 2009 patterns of soil nitrous acid emissions and their acceleration of rural photochemical
 2010 reactions. *Journal of Geophysical Research: Atmospheres*, 127, e2021JD036379.
 2011 <https://doi.org/10.1029/2021JD036379>, 2022.
- 2012 WMO: *International Meteorological Vocabulary* (2nd ed.), Geneva: Secretariat of the World
 2013 Meteorological Organization. 1992. p. 636. ISBN 978-92-63-02182-3, 1992
- 2014 Wang and Chen, A review on parameterization and uncertainty in modeling greenhouse gas
 2015 emissions from soil, *Geoderma*,: <https://doi.org/10.1016/j.geoderma.2011.11.009>,
 2016 2012.
- 2017 Xue, X., Ren, G. Y., Xu, X. D., Sun, X. B., Yang, G. W., Zhang, P. F., & Zhang, S. Q.: The
 2018 trends of warm-season thunderstorm and lightning days in China and the influence of
 2019 environmental factors, *J. Geophys. Res.*, 126 (15), 10.1029/2021JD034950, 2021.
- 2020 Yang, X., and Li, Z.: Increases in thunderstorm activity and relationships with air pollution in
 2021 southeast China, *J. Geophys. Res. Atmos.*, 119, 1835–1844,
 2022 doi:10.1002/2013JD021224, 2014.
- 2023 Yang et al.: Photochemical emissions of HONO, NO₂ and NO from the soil surface under
 2024 simulated sunlight, *Atmospheric Environment*,
 2025 <https://doi.org/10.1016/j.atmosenv.2020.117596>, 2020.
- 2026 Yetong Li, Yan Xia, Fei Xie, Yingying Yan, Influence of stratosphere-troposphere exchange
 2027 on long-term trends of surface ozone in CMIP6, *Atmospheric Research*, 297, doi:
 2028 <https://doi.org/10.1016/j.atmosres.2023.107086>, 2024.

- 2029 Yin, Y., Chevallier, F., Ciais, P., Broquet, G., Fortems-Cheiney, A., Pison, I., and Saunois, M.:
2030 Decadal trends in global CO emissions as seen by MOPITT, *Atmos. Chem. Phys.*, 15,
2031 13433–13451, <https://doi.org/10.5194/acp-15-13433-2015>, 2015.
- 2032 Young, P.J., Naik, V., Fiore, A.M., Gaudel, A., Guo, J., Lin, M.Y., Neu, J.L., Parrish, D.D.,
2033 Rieder, H.E., Schnell, J.L., Tilmes, S., Wild, O., Zhang, L., Ziemke, J.R., Brandt, J.,
2034 Delcloo, A., Doherty, R.M., Geels, C., Hegglin, M.I., Hu, L., Im, U., Kumar, R.,
2035 Luhar, A., Murray, L., Plummer, D., Rodriguez, J., Saiz-Lopez, A., Schultz, M.G.,
2036 Woodhouse, M.T. and Zeng, G. Tropospheric Ozone Assessment Report: Assessment
2037 of global-scale model performance for global and regional ozone distributions,
2038 variability, and trends, *Elem Sci Anth*, 6(1), p.10. DOI: 10.1525/elementa.265, 2018.
- 2039 Zeng, G., Morgenstern, O., Braesicke, P., Pyle, J.A.: Impact of stratospheric ozone recovery
2040 on tropospheric ozone and its budget: impact of ozone recovery on tropospheric
2041 ozone. *Geophys. Res. Lett.* 37, n/a-n/a. <https://doi.org/10.1029/2010GL042812>,
2042 2010.
- 2043 Zhang, X., Yin, Y., van der A, R., Lapierre, J. L., Chen, Q., Kuang, X., Yan, S., Chen, J., He,
2044 C., and Shi, R.: Estimates of lightning NO_x production based on high-resolution OMI
2045 NO₂ retrievals over the continental US, *Atmos. Meas. Tech.*, 13, 1709–1734,
2046 <https://doi.org/10.5194/amt-13-1709-2020>, 2020 .
- 2047 Zhang, L., T. Wang, Q. Zhang, J. Zheng, Z. Xu, and Lv, M.: Potential sources of nitrous acid
2048 (HONO) and their impacts on ozone: A WRF-Chem study in a polluted subtropical
2049 region, *J. Geophys. Res. Atmos.*, 121, 3645–3662, doi:10.1002/2015JD024468, 2016.
- 2050 Zheng, B.; Chevallier, F.; Yin, Y.; Ciais, P.; Fortems-Cheiney, A.; Deeter, M.N.; Parker,
2051 R.J.; Wang, Y.; Worden, H.M.; Zhao, Y. Global atmospheric carbon monoxide
2052 budget 2000-2017 inferred from multi-species atmospheric inversions. *Earth Sys. Sci.*
2053 *Data*, 11, 1411–1436, <https://doi.org/10.5194/essd-11-1411-2019>, 2019.